5-2015

Improving Mechanical Properties of Bulk Metallic Glasses by Approaches of In-situ Composites and Thin Films

Haoling Jia

University of Tennessee - Knoxville, hjia2@vols.utk.edu

To the Graduate Council:

I am submitting herewith a thesis written by Haoling Jia entitled "Improving Mechanical Properties of Bulk Metallic Glasses by Approaches of In-situ Composites and Thin Films." I have examined the final electronic copy of this thesis for form and content and recommend that it be accepted in partial fulfillment of the requirements for the degree of Doctor of Philosophy, with a major in Materials Science and Engineering.

Peter K. Liaw, Major Professor

We have read this thesis and recommend its acceptance:

Yanfei Gao, Haixuan Xu, Mariya Zhuravleva, Hairong Qi

Accepted for the Council:

Carolyn R. Hodges

Vice Provost and Dean of the Graduate School

(Original signatures are on file with official student records.)

Improving Mechanical Properties of Bulk Metallic Glasses by Approaches of In-situ Composites and Thin Films

A Dissertation Presented for the
Doctor of Philosophy
Degree
The University of Tennessee, Knoxville

Haoling Jia
May 2015

DEDICATION

This dissertation is dedicated to my wife, Dan Wang, my son, Lucas Jia, my parents, Fucheng Jia and Xingmei Ma, and my grandparents, Laiqing Jia and Guilin Chen, who always love, understand, and encourage me under any circumstances. They are also very proud of me for becoming the first doctorate in our Jia family.

ACKNOWLEDGEMENTS

Firstly, I would like to express my sincere gratitude to my major academic advisor, Dr. Peter K. Liaw, and co-advisor, Dr. Yanfei Gao for giving me the greatest help both academically and personally throughout my research at The University of Tennessee. Their consistent guidance, kindness, encouragement, and patience made the completion of my Ph.D. study possible. Moreover, Dr. Jinn. P. Chu, Mr. Chia-Chi Yu, and Dr. Junwei Qiao have been giving me tremendous help in the sample preparation and valuable discussion throughout my research work. I would also thank Dr. Haixuan Xu, Dr. Mariya Zhuravleva, and Dr. Hairong Qi for kindly being in my committee and offering lots of help and suggestions.

Moreover, many people kindly help me in different aspects during the process of my PhD study. Great appreciations go to Mr. Greg Jones, Mr. Frank Holiway, Mr. Randy Stooksbury, and Mr. Doug Fielden for their great help on my experiments. I would like also to appreciate the help from the great staff members in our department, including: Ms. Carla Lawrence, Ms. Carol Winn, Ms. Martha Gale, Ms. Tonya Brewer, and Ms. Tracy Lee of The University of Tennessee. Finally, great thanks are paid to my friends, Dr. Gongyao Wang, Dr. Xie Xie, Dr. Shenyan Huang, Dr. Andrew Chuang, Dr. Wei Wu, Dr. Lu Huang, Dr. Zhenke Teng, Dr. Zhi Tang, Dr. Li Li, Dr. Yan Wang, Dr. Qing Wang, Dr. Lili Zheng, Dr. Weidong Li, Dr. Lin Li, Dr. Yuzhi Xia, Dr. Feng Jiang, Mr. Zhiqian Sun, Mr. Zhinan An, Mr. Wei Guo, Mr. Chao Pu, Ms. Haoyan Diao, Ms. Shuying Chen, Mr. Haifei Li, Ms. Xue Bai, Mr. Rui Feng, Mr. Peiyou Chen, Mr. Gian Song, and other group members for their kind help.

Acknowledgements are also given to the financial support from the National Science Foundation (DMR 0909037) and The Department of Materials Science & Engineering at University of Tennessee.

ABSTRACT

Bulk-metallic glasses (BMGs) exhibits lots of unique properties, such as, high strengths, high hardness, high specific strengths, superior elastic limits, high corrosion resistance, etc. However, the applications of BMGs are still quite limited due to their intrinsic brittleness and low ductility at room temperature. Many efforts have been conducted to improve the plasticity of BMGs, in which metallic-glass-matrix composites (MGMCs) and thin-film metallic glasses (TFMGs) are two popular and effective approaches. Nevertheless, the deformation mechanisms for the improved plasticity of MGMCs and TFMGs are still far from satisfactory understanding, which will be investigated using both experimental and simulation methods in the present work.

For the MGMCs, in situ high-energy synchrotron X-ray diffraction experiments and micromechanics-based finite element simulations have been conducted to examine their lattice strain evolution. The entire lattice-strain evolution curves can be divided into elastic-elastic (denoting deformation behavior of matrix and inclusion, respectively), elastic-plastic, and plastic-plastic stages. Characteristics of these three stages are governed by the constitutive laws of the two phases (modeled by free-volume theory and crystal plasticity) and geometric information (crystalline phase morphology and distribution).

The deformation behavior, especially the fatigue behavior, of TFMG materials has been investigated on the some substrates, including 316L stainless steel, BMG, etc. The results show that the four-point-bending fatigue life of the substrates is greatly improved by Zr- and Cu-based TFMGs, while Fe-based TFMG, TiN, and pure-Cu films

are not so beneficial in extending the fatigue life of 316L stainless steel. However, quite limited work is reported on the fatigue behavior of TFMG coated on the BMG substrate, which can be a very interesting topic. Moreover, a synergistic experimental/theoretical study are conducted to investigate the micro-mechanisms of the fatigue behavior of TFMGs adhered to BMG substrates. Furthermore, shear-band initiation and propagation under deformation are investigated using the Rudnicki-Rice instability theory and the free-volume models employing finite-element simulations.

TABLE OF CONTENTS

CHAPTER I INTRODUCTION 1
CHAPTER II LITERATURE REVIEW 4
2.1 Metallic-glass-matrix Composites 4
2.1.1 Ex-situ MGMCs 4
2.1.2 In-situ MGMCs 7
2.1.3 Fabrication of bulk metallic glasses and composites 14
2.1.4 Summary 21
2.2 Thin-film metallic glass 22
2.3 Motivation and Scientific Issues 28
CHAPTER III METALLIC-GLASS-MATRIX COMPOSITES 29
3.1 Introduction 29
3.2 Experimental and Modeling Methods 35
3.2.1 Experimental Methods 35
3.2.2 Finite-Element Modeling 37
3.3 Results and Discussion 43
3.4 Summary 52
CHAPTER IV THIN-FILM METALLIC GLASS 54
4.1 Introduction 54
4.2 Experimental and Numerical Approaches 57
4.2.1 Coating preparation and characterization 57
4.2.2 Fatigue tests 60
4.2.3 Numerical Method with FEM (Rudnicki-Rice instability theory) 60
4.3 Fatigue behavior of TFMGs on BMG substrates 62
4.3.1 Summary on the reported work on the fatigue behavior of TFMGs 62
4.3.2 Fatigue behavior of TFMG with BMG substrate 65
4.3.3 Deformation mechanism of TFMG-BMG with TEM 69
4.4 Finite-element simulations of the mechanical behavior of TFMGs 71
4.4.1 Rudnicki-Rice instability-theory simulations 71
4.4.2 Free-volume-model simulations 73
4.5 Summary 77
CHAPTER V CONCLUSION AND FUTURE WORK 79
REFERENCES 81
APPENDICES 112
APPENDIX I 113
APPENDIX II 118
APPENDIX III 191
VITA 194

LIST OF TABLES

Table 1. Strength-stiffness ratios of a number of [hkl] grains in the crystalline phase and the metallic-glass (MG) matrix, with an initial yield stress of 150 MPa for the crystalline phase. [186]..... 114
Table 2. Parameters used in the finite element simulations with results matching the lattice strain evolution in the composites, as shown in Figure 32. [186]..... 115
Table 3. Chemical compositions (in weight percent) of 316L stainless steel, C-2000® Ni-based alloy, 7075-T6 Al-based alloy, Zr-based alloy, and Ti-based alloy substrates. [155] 116
Table 4. Ultimate tensile strengths of substrate materials, including 316L stainless steel, C-2000® Ni-based alloy, 7075-T6 Al-based alloy, Zr-based alloy, and Ti-based alloy, as well as Zr-based and Cu-based BMGs. [155]..... 117

LIST OF FIGURES

Figure 1. (a) An optical micrograph showing uniformly-distributed WC particles in the V106 matrix; (b) X-ray diffraction patterns of the V106 matrix, the alloy reinforced with 10 vol. % WC, and pure WC particle; and (c) Quasi-static compression stress–strain curves of V106 composites reinforced with Ta, W, and WC particles. [35, 37]..... 119
Figure 2. (a) Hardness values of the matrix reinforced by different volumes of the ZrC particles and (b) linear fitness of the modulus, E, and yielding strength, σ_y, with increasing the volume fraction (V_f) of ZrC. [40]..... 120
Figure 3. (a) SEM micrograph in the backscatter mode of 80 vol. % W wire / bulk metallic glass matrix composite. The sample is polished and cut normal to the uniaxial reinforcement; [41] (b) SEM backscattered-electron image of *in-situ* composite microstructure (Inset: X-ray diffraction pattern for the $(Zr_{75}Ti_{18.34}Nb_{6.66})_{75}X_{25}$ *in-situ* composite. [67] (c) Backscattered SEM of the *in-situ* composite with a composition of $(Zr_{70}Ni_{10}Cu_{20})_{82}Ta_8Al_{10}$. [91]..... 121
Figure 4. A pseudo ternary phase diagram with apexes of zirconium, (titanium + niobium), and X, where X represents the moiety $Cu_5Ni_4Be_9$. [69]..... 122
Figure 5. X-ray diffraction patterns of four samples with different compositions..... 123
Figure 6. SEM images of the cross sections of the composites with the compositions of: (a) Zr54, (b) Zr56, (c) Zr58, and (d) Zr60. [69]..... 124
Figure 7. (a) the compressive engineering stress-strain curves of the four composites, [69] and (b) the tensile engineering stress-strain curves of the Zr60 composite. [71]..... 125
Figure 8. Dependence of tensile ductility on crystalline volume fraction. [97]..... 126
Figure 9. Typical schematic illustration of copper-mold suction casting, and the arc melter at The University of Tennessee shown in the inset. [102]..... 127
Figure 10. Schematic diagram of the apparatus for casting bulk MGMCs. [35]..... 128
Figure 11. The Bridgman solidification apparatus used by Qiao *et al.* (a), and the corresponding illustration exhibited in (b). [147]..... 129
Figure 12. XRD patterns (a) and DSC traces (b) of the composites synthesized with different withdrawal velocities. [53]..... 130
Figure 13. The microstructure of the sample with v = 1.0 mm/s is illustrated in (a), the dependences of spanning lengths of individual dendrite trees on varied withdrawal velocities shown in (b), and the dependences of fracture strengths and plastic strains of the composites developed by the Bridgman solidification on the v (c), the inset in (c) indicating the sample with v = 1.0 mm/s after bending. [29]..... 131
Figure 14. Classification of MGMCs. [147]..... 132
Figure 15. (a) S–N curves of 316L stainless-steel specimens coated with Zr-based metallic-glass films of different thicknesses (200 nm and 1 μm), as well as the bare substrate, under four-point-bending fatigue tests. (b) S–N curves of a Ni-based alloy and specimens coated with Zr-based metallic-glass films of different thicknesses, 200 nm and 1 μm. (c) S–N curves of a Zr-based alloy substrate, as well as coated specimens with Zr-based TFMGs of different thicknesses, 200 nm and 1 μm.(d) S–N curves of 7075-T6 aluminum alloys with and without ZrCuNiAlSi TFMG coatings. (e) S–N curves for Ti–

6Al–4V alloy substrates coated with TiN, TFMG ($Zr_{50}Cu_{27}Al_{16}Ni_7$, at.%), and TFMG/Ti. (Redrawn from [152, 156, 157, 251]) 133
Figure 16. SEM fractographs of failed 316L stainless-steel specimens coated with a $Zr_{47}Al_{13}Cu_{31}Ni_9$ TFMG of different thicknesses: (a) 200-nm-thick and (b) 1-μm-thick; (c) good adhesion between the 1-μm-thick film and substrate is shown at the crack-initiation site; and (d) blockage of the substrate-slip deformation by the 1-μm-thick thin film (Reproduced with permission from [156]). 134
Figure 17. SEM fractographs of (a) the interface between the substrate and film, illustrating partial delamination of the Zr-based film due to severe slip deformation of the substrate, and (b) the fracture surface of the TFMG-coated Zr-based alloy after a four-point bending fatigue test [251]. 135
Figure 18. SEM fractographs of (a) uncoated and (b) TFMG-coated 7075-T6 Al alloy specimens fractured at σmax. = 300 and 350 MPa, respectively, under four-point-bending fatigue tests. (I), (II), and (III) on images (a) and (b) represent crack-initiation, crack propagation, and final-fast-fracture regions, respectively [152]. 136
Figure 19. SEM fractographs of a 7075-T6 Al alloy specimen coated with the Zr-based TFMG and fractured at σmax. = 350 MPa under four-point-bending fatigue tests in two views: (a) top-view image and (b) enlarged tilt-view image of the tension surface [152]. 137
Figure 20. Cross-sectional TEM micrograph obtained from an Al-alloy-substrate specimen coated with a Zr-based TFMG after fatigue tests at σmax. = 350 MPa; the arrows indicate slip bands in the Al-alloy substrate, the offset, and cracking regions in the Zr-based TFMG [152]. 138
Figure 21. TEM cross-sectional fractographs of a coated Ti–6Al–4V substrate with σmax. = 675 MPa, (a) before load, (b–d) interrupted after 5 × 105, 5 × 106, and 6.4 × 106 fatigue cycles, respectively. (e–h) corresponding AFM morphology images with the values of rms surface roughness. [158] 139
Figure 22. A proposed mechanism for fatigue-crack-initiation in the film/substrate system, showing that substrate dislocation pileups are suppressed by the high ductility and strength of the amorphous film [156, 159] 142
Figure 23. Representative reported BMG alloys. [9] 143
Figure 24. (a) Engineering stress vs. strain curves of monolithic BMG and MGMCs; (b) SEM images of composites. [30, 70] 144
Figure 25. (a) Deformation in composites occuring through the development of highly-organized patterns of regularly-spaced shear bands distributed uniformly along the crack path; (b) Microcracks in composites are nucleated along the shear bands or at the matrix/dendrite interface. [169] 145
Figure 26. A review of the ductility and yield strength of different kinds of coatings, including TFMGs, metallic coatings, and ceramic coatings applied to improve mechanical properties of substrate materials. [155] 146
Figure 27. (a) Scanning electron microscope image of the dendritic crystalline phase (β) in the metallic glass matrix with the composite composition of $Zr_{58.5}Ti_{14.3}Nb_{5.2}Cu_{6.1}Ni_{4.9}Be_{11.0}$ (at.%) and the crystalline phase volume percentage of ~ 55%. (b) Schematic illustration of the in situ synchrotron X-ray diffraction experiment on the compression sample. (c) X-ray diffraction pattern of the as-cast specimen before

deformation. (d) Line profiles for the specimens before deformation and at an applied stress of ~ 1,500 MPa [186]. 147
Figure 28. (a) The finite element simulation is conducted on a compression specimen with cubic elements in ABAQUS model. (b) and (c) display all the crystalline grains and the [310] grains, respectively. [186] 150
Figure 29. (a) The macroscopic compressive engineering stress - strain curve shows considerable plastic deformation. (b) A representative stress - lattice strain curve can be divided into 3 stages. This example is particularly for grains with their <310> directions parallel to the loading direction. [186]..... 151
Figure 30. Stress versus lattice strain curves from the X-ray diffraction with the extrapolated lines from the elastic stage of each curve. Four grain families, [200], [211], [220], and [310], have been measured. [186] 154
Figure 31. Stress versus intergranular strain curves for [200], [211], [220], and [310] grains in the transition from Stages I to II. [186]..... 155
Figure 32. Experimental and finite element simulation results of the lattice strain evolution curves for [200], [211], [220], and [310] grains. [186] 156
Figure 33. Stress versus $\varepsilon_{33}^{elastic}$ curves of the single inclusion model with cubic, spherical, and dendritic inclusion shapes (inset). [186] 157
Figure 34. (a) Stress versus $\varepsilon_{22}^{elastic}$ curves for both the inclusion and matrix in the composite with the dendrite inclusion shown in (b), which shows the Mises stress contours at stress level (iv). Both the matrix and inclusion are simulated as elastic-perfectly plastic solids, with Young's modulus, Poisson's ratio, and yield stress being 89 GPa, 0.37, and 1.4 GPa for the matrix, and 60 GPa, 0.37, and 0.45 GPa for the inclusion. [186]..... 158
Figure 35. (a) Everything else being the same as Figure 34(a), the rotation of the dendritic crystalline phase by 45 ºleads to a dramatic change of the lattice strain evolution when the matrix yields (i.e., at the very end of the stress - $\varepsilon_{22}^{elastic}$ curves). (b) The Mises stress contours of model in (a) at stress level (iv). [186]..... 159
Figure 36. (a) Stress versus $\varepsilon_{22}^{elastic}$ curves for both the inclusion and matrix in the composite with multiple circular inclusions; (b) The Mises stress contour is shown at stress level (iv). The matrix is described by the free volume constitutive model, with the Young's modulus and Poisson's ratio being 200 GPa and 0.37, respectively. Other parameters can be found in the text. The inclusion phase is an elastic-perfectly plastic solid with the Young's modulus, Poisson's ratio, and yield stress being 60 GPa, 0.37, and 0.45 GPa, respectively. All figures are given in a deformed mesh with a displacement magnification ratio of 1, and the state-dependent variable 1 (SDV1) specifies the free volume. [186]..... 160
Figure 37. (a) Stress versus $\varepsilon_{22}^{elastic}$ curves for both the inclusion and matrix in the composite with multiple dendritic inclusions. (b) The Mises stress contour is shown at stress level (iv). The material parameters are all same as these in the Figure 36. [186] 161
Figure 38. Specimen sketches for four-point-bending fatigue tests. [155]Figure 39. (a) S-N and (b) S/UTS-N curves for all the reported TFMGs on different kinds of substrates. Five regions are separated in (a) by: A) low fatigue-endurance limit region; B) medium fatigue-endurance limit region; C) high fatigue-endurance limit region; D) tension-

tension region; and E) monolithic BMG region. In (b), the regions, corresponding to (a), are represented by A', B', C', D', and E'. [155]..... 162
Figure 40. (a) and (b) show the improvement of fatigue-endurance limit vs. UTS, improvement of fatigue-endurance limit/UTS vs. UTS, respectively, for all the reported substrate materials, including 316L steel, Ni-based alloy, Zr-based alloy, Ti-based alloy, and Al-based alloy. [155]..... 166
Figure 40 continued Figure 41. (a), (b) and (c) show the improvement of fatigue-endurance limit vs. fatigue-endurance limit, improvement of fatigue-endurance limit/UTS vs. fatigue-endurance limit, and fatigue-endurance limit vs. UTS, respectively, for all the reported substrate materials, including 316L steel, Ni-based alloy, Zr-based alloy, Ti-based alloy, and Al-based alloy. [155]..... 168
Figure 42. (a) XRD patterns for the BMG substrate and TFMG; and (b) S-N curves of bare BMG and BMG substrate with Zr-based TFMG. 173
Figure 43. (a) SEM fractography micrograph of the BMG substrate with a 200 nm-thick Zr-based TFMG after fatigue fractured at σ_{max} = 450 MPa, (b) transition regions between Stage II and Stage III, and (c) partial film delamination due to the severe deformation of the BMG substrate. 174
Figure 44. (a) TEM cross-sectional images of TFMG-coated BMG specimen after fatigue fractured at σ_{max} = 450 MPa. (b) Amplified image of the interface area in (a). 175
Figure 45. (a) SEM fractography micrograph of the BMG substrate with a 200 nm-thick Zr-based TFMG after fatigue fractured at σ_{max} = 500 MPa, (b) enlarged image of crack-initiation region, (c) transition regions between Stage II and Stage III, (d) partial film delamination due to the severe deformation of the BMG substrate, and (e) fast-failure region. 176
Figure 46. Microcracks associated with shear-off steps formed on the tensile surface near the fracture surface of a coated $Zr_{50}Cu_{30}Al_{0}Ni_{10}$ specimen tested at σ_{max} = 500 MPa. (a) and (b) are the tilt-view at different locations of sample in different magnifications. ... 177
Figure 47. TEM EDS line-scans at the interface of TFMG and BMG substrate after fatigue fractured at σ_{max} = 500 MPa. (a) STEM image; (b) Enlarged TEM image of the shear offset area in (a); (c) EDS line-scan directions marked with the red arrows; (d) and (e) EDS line-scan profile at the interface of film and substrate..... 178
Figure 48. (a) TEM cross-sectional images of TFMG-coated BMG specimen after fatigue fractured at σ_{max} = 500 MPa; (b) Enlarged image of the red circle area in (a); and (c) Enlarged image of the red circle area in (c). 179
Figure 49. (a) TEM cross-sectional images of the film area in the TFMG-coated BMG specimen after fatigue fractured at σ_{max} = 500 MPa; (b) SAED result of the red circle area in (a), indicating the fully amorphous structure. 180
Figure 50. (a) TEM cross-sectional images of TFMG-coated BMG specimen after fatigue fractured at σ_{max} = 500 MPa; and (b) Enlarged image of the shear-off steps area (blue circle) in (a). 181
Figure 51. (a) SEM fractography micrograph of the BMG substrate with a 200 nm-thick Zr-based TFMG after fatigue fractured at σ_{max} = 600 MPa, (b) transition regions between Stage II and Stage III, (c) and (d) interface area of the TFMG-BMG specimen after fatigue fracture. 182

Figure 52. An indentation model (2D) with free-volume contour plots in different adhesion cases: (a) a BMG substrate without coatings; (b) a thin-film coated BMG, in which the substrate and film is completely bonded; (c) a BMG specimen coated with a weakly-bonded thin film; (d) bending stress vs. surface strain curves for uncoated and coated BMG samples, together with 316L stainless steel for comparison. 183
Figure 53. An indentation model (2D) with free-volume contour plots in different film-thickness cases: (a) a BMG substrate without coatings; (b) a BMG substrate with a thin TFMG, having a film/substrate thickness ratio of 1/20; and (c) a BMG substrate with a thick TFMG, having a film/substrate thickness ratio of 1/5. 184
Figure 54. An indentation axisymmetric model (3D) with free-volume contour plots for BMG specimens: (a) without and (b) with TFMG. 185
Figure 55. An indentation axisymmetric model (3D) with stress plots for BMG specimens: (a) without and (b) with TFMG. 186
Figure 56. An indentation axisymmetric model (3D) with (a) shear band and (b) stress plots for BMG specimens coated with Ti-alloy thin film. 187
Figure 57. An indentation 3D model with shear-band plots for BMG specimens using Berkovich indenter: (a) without and (b) with TFMG. 188
Figure 58. (a) ABAQUS model of a half-symmetric Rockwell indention in a metallic glass, used for predicting shear-band directions in (b) a BMG substrate, and (c) a Ti-coated BMG witha film/substrate thickness ratio of 1/20, having $\mu + \beta = 0$ and $\upsilon=0.3$. The blue solid curves indicate predicted shear-band directions, and the red dashed curves are principal shear-stress directions. The short solid black and dashed green curves are corresponding shear-band directions and the principal shear-stress directions. [155] ... 189
Figure 59. Summary of fatigue crack-initiation and propagation mechanisms in a TFMG/substrate system. [155] 190

CHAPTER I
INTRODUCTION

In 1960, the first metallic glass (MG) was reported in the alloy, $Au_{75}Si_{25}$ (All of the compositions in the text are in atomic percent, at. %), by Duwez et al [1]. The so-called metallic glass retains the disordered atomic structure of high-temperature melts, which is usually prepared from extremely rapid cooling to avoid crystallization. In the early development stage of metallic glasses, they are generally produced into ribbons, films, or wires, since heat can be extracted quickly enough to achieve the amorphous critical cooling rate of ~ $10^5 – 10^6$ K/s. For example, in the 1970s, amorphous ribbons and wires are fabricated, mainly in the Fe- and Co-based alloy systems, focusing on their excellent softer magnetic properties [2]. Meanwhile, Turnbull's criterion is proposed: a liquid with $T_g / T_m = 2/3$ (T_g and T_m denoting the glass-transition temperature and melting temperature, respectively) becomes very sluggish in crystallization, which will be easier to form a glass alloy. Then, "bulk" metallic glasses are reported sequentially [3-5]. Here, the "bulk" is arbitrarily defined as the millimeter (mm) scale. For example, in 1974, Chen reported the first bulk metallic glasses (BMGs) in the ternary Pd–Cu–Si alloy system, which yielded a cylindrical specimen with the diameter of l - 3 mm and length of several centimeters (cm), possessing a critical cooling rate of less than $l0^3$ K/s [3]. In 1980s, more BMG alloy systems were developed, and considerable efforts are contributed to the fundamental understanding of atomic structure of MGs, as well as further exploration of their mechanical, magnetic, and chemical properties [5].

During the late 1980s, Inoue's group succeeded in developing many multicomponent BMG alloy systems with lower critical cooling rates, generally consisting of common metallic elements, including the well-known Pd-Cu-Ni-P, Zr-Al-transition metal (TM), and Zr-Ti-Al-TM-Pd alloys [6], as well as other alloys, such as Ln-, Ti-, Mg-, Fe-, and Ni-based BMG systems [1, 7-9]. For example, high glass-forming ability is found in La–Al–Ni and La–Al–Cu alloy systems, which possessed a critical diameters of 5 mm [10]. In BMG alloy of $Mg_{80}Cu_{10}Y_{10}$, the fully amorphous specimen is prepared with a maximum diameter of ~ 10 mm in cylindrical shape [11]. In the 1990s, the BMG alloys of $Zr_{65}Al_{7.5}Ni_{10}Cu_{17.5}$ and $Zr_{55}Al_{10}Ni_5Cu_{30}$ were fabricated with a diameter up to 16 mm using water quenching and suction-casting approach, respectively [12, 13]. In 1997, the Pd–Cu–Ni–P family with the super high glass-forming ability (GFA) was discovered with a critical casting diameter of 72 mm [14], which is one of significant breakthroughs during the development of BMGs. Moreover, another important BMG alloy is $Zr_{41.2}Ti_{13.8}Cu_{12.5}Ni_{10}Be_{22.5}$, developed in Johnson's group, which is commonly referred as Vitreloy 1 (Vit1) alloy [15].

In the early 21th century, the research enthusiasm on BMGs is mostly focused on the structures and properties of BMGs and their promise for structural applications due to their unique properties, such as, high strengths (over 5 GPa [16]), high hardness, high specific strengths (strength / density), superior elastic limits (2 %), good wear resistance, high corrosion and oxidation resistance, etc. [7, 9, 15, 17-24]. However, the applications of BMGs as structural materials are severely limited because of their low ductility, intrinsic brittleness, and moderate fatigue resistance at room temperature, which is mainly due to the formation of localized shear bands that quickly lead to catastrophic

fracture of BMG specimens [25-27]. The so-called shear bands in BMGs are the deformation bands with a thickness of only 10 nm [28], distributed on the lateral surface of deformed samples, much less than the thickness of deformation bands in conventional crystalline alloys with a typical value of several microns. There have been several approaches to improve the room-temperature ductility of BMGs, including microstructure modifications by adding dispersed inclusions in the amorphous matrix to form metallic-glass-matrix composites (MGMCs) [29-31] and surface modifications of BMG, such as thin film metallic glasses (TFMGs) [22, 32-34], which all seek to block major shear bands and thus to induce a more homogeneous distribution of shear bands in BMGs during deformation. However, the micro mechanism study on these two new materials is still quite limited. Therefore, it would be very interesting topic to investigate the deformation mechanisms responsible for the improved mechanical performance of MGMCs and TFMGs.

In Chapter II of the present work, we will review the recent developments in MGMCs and TFMGs, with particular emphases on their deformation and fracture mechanisms. Moreover, both experimental and continuum modeling will be employed to investigate the deformation behavior of MGMCs and TFMGs in Chapter III and Chapter IV, respectively.

CHAPTER II
LITERATURE REVIEW

2.1 Metallic-glass-matrix Composites

In the last two decades, Johnson et al. make tremendous progress in the designing and preparation of metallic-glass-matrix composites to improve the plasticity of BMGs, while Inoue et al. made great contribution on the development of BMGs, as mentioned in Chapter I. In this Chapter, we will review the recent advances in MGMCs, including both *in-situ* and *ex-situ* MGMCs, with particular emphases on the deformation and fracture mechanisms of *in-situ* MGMCs, due to their better structural and mechanical performance, compared with the *ex-situ* MGMCs.

2.1.1 *Ex-situ* MGMCs

In order to avoid the early failure of monolithic BMGs upon deformation as discussed in Chapter I, a straightforward approach is adding secondary phases in the glassy matrix, which can arrest the propagation of shear bands into macro-cracks, therefore, leading to the formation of multiple minor shear bands. This kind of dual-phase composite is called *ex-situ* MGMCs, which is usually categorized into two types, depending on the second phase geometry: (a) particle-reinforced and (b) fiber-reinforced MGMCs.

(a) Particle-reinforced MGMCs

The first particle-reinforced *ex-situ* MGMC was prepared by Choi-Yim et al. in 1997 [35], in the glassy matrix with the nominal composition of: $Cu_{47}Ti_{34}Zr_{11}Ni_8$, $Zr_{52.5}Ti_5Al_{10}Cu_{17.9}Ni_{14.6}$ (V105), and $Zr_{57}Nb_5Al_{10}Cu_{15.4}Ni_{12.6}$ (V106), while ceramics and

metals are used as the secondary phases, such as SiC, WC, W, and Ta, with volume fractions (vol. %) varied from 5 % – 30 %. The particle sizes ranged between 20 and 80 μm. These MGMCs were fabricated by remelting a mixture of the pre-alloyed metallic glass-forming elements and second phases using induction melting, then, injected through a nozzle into a copper mold under the high-purity argon atmosphere. The optical micrograph of this MGMC is displayed in Figure 1(a), which can be observed that uniformly-distributed WC particles in the V106 matrix with the particle size of ~ 50 μm and the second phase vol. % of ~ 10 % [35]. Figure 1(b) presents the X-ray diffraction patterns of the V106 matrix, the alloy reinforced with 10 vol. % WC, and pure WC particle [36]. The X-ray results of the MGMCs present diffraction peaks from WC particles superimposed on the broad diffuse scattering maxima from the glass matrix, which is different with the X-ray patterns of V106 and Pure WC. The quasi-static compression stress-strain curves of V106 composites reinforced with Ta, W, and WC particles were investigated [Figure 1(c)], which exhibited the compressive plastic deformation of ~ 0.5 %, 7 %, 3 – 5 %, and ~ 0%, for monolithic V106, W-reinforced, Ta/WC-reinforced, and SiC-reinforced MGMCs, respectively [37].

Up to now, many different particle-reinforced *ex-situ* MGMCs have been reported, such as WC_p / Zr-based [35-37], WC_p / Cu-based [35], SiC_p / Zr-based [35-37], SiC_p / Cu-based [35, 36], Ta_p / Zr-based [35-38], and C_p / Zr-based bulk MGMCs (the subscript, p, denoting particles) etc. [39]. All these *ex-situ* dual-phase composites exhibit toughness at room temperature. Therefore, the intrinsic brittleness of monolithic BMGs is greatly improved by adding the ductile metals, such as Ti particles, or brittle intermetallics, such as ZrC particles, into the glass matrix. Meanwhile, other mechanical properties, such as

hardness, can also be enhanced for the MGMC ($Zr_{55}Al_{10}Ni_5Cu_{30}$) with ZrC as inclusion, which is shown in Figure 2(a). Moreover, as displayed in Figure 2 (b), the yielding strength and elastic modulus exhibit a close-to-linear increase with the increase in the ZrC content ranging from 0 to 20 vol.% [40].

(b) Fiber reinforced MGMCs

In 1998, long-fiber reinforced MGMCs ($Zr_{41.2}Ti_{13.8}Cu_{12.5}Ni_{10.0}Be_{22.5}$) were firstly synthesized by Dandliker et al, with the tungsten and carbon steel continuous wire reinforcement [41, 42]. The SEM micrographs of an 80 vol.% tungsten-wire reinforced MGMCs are shown in Figure 3(a) [41]. The presence of continuous long fibers in the glass matrix can effectively retard the prompt development of shear bands upon loading, which is analogous to the cases in particle-reinforced MGMCs. Note that the unreinforced metallic glass is elastic up to 1,900 MPa, and shows no significant plastic deformation. In contrast, the fiber reinforced MGMCs have a varied plastic strain of 2% - 16% depending on different inclusion and slightly improved ultimate strength [41].

Fiber-reinforced MGMCs have been widely reported in Al, Mg, Cu, and Ti alloys to increase their strengths. Up to now, there are W_f / Zr-based [41-47], W_f / Cu-based [48], Cu_f / Zr-based [49], Ta_f / Zr-based [50], stainless steel fiber / Zr-based MGMCs [51]. For this kind of composites, the modulus of the composites is usually calculated, using the Rule of Mixture (ROM):

$$E_c = fE_f + (1-f)E_m \quad (1)$$

where E_c, E_f, and E_m are the moduli for the composite, the fiber, and glass matrix, respectively, and f is the volume fraction of fibers. According to Eq. (1), E_c is easily calculated, which is highly consistent with the experimental results [42].

Regardless of particle- or fiber-reinforced MGMCs, the wetting behavior has an important effect on the bonding at the interface [52]. The infiltration pressure, the volume fraction of fibers, and the filtration length together determine the reactive wetting. For a system in which the melt partly wets the fibers, the extra pressure, P, is needed to put the metallic melt to infiltrate into fibers. For the ideal unidirectional infiltration, the analytical solution of the filtration velocity, v, can be derived as [52]:

$$v = \frac{R^2}{8\eta h}[P + \rho g(H_0 + hV_f) + \frac{2\sigma_{lg}\cos\theta}{R}] \quad (2)$$

where h is the length of fibers, H_0 the height of melt, R the radius of fiber, g the gravitational acceleration, η the viscosity of the melt, ρ the density of melt, θ the contact angle, and σ_{lg} the surface tension of the melt. Based on Eq. (2), the determined infiltration dynamics investigation is believed to provide the valid foundation for controlling preparation conditions of fiber-reinforced composites.

2.1.2 In-situ MGMCs

The nature of plasticity improvement by introducing secondary phases in the metallic-glass matrix is that the secondary phases can inhibit the propagation of shear bands in the amorphous matrix, and promote the formation of multiple shear bands. Besides the effective addition of *ex-situ* inclusions, *in-situ* crystalline phases during the

solidification of melts can be another good selection [53], in which the *in-situ* crystalline phases is usually comprised of nanorystallites or dendrites. Beyond that, a few special brittle intermetallic phases [54, 55] or *in-situ* two amorphous phases through the phase separation [56, 57] are also employed to toughen the BMGs.

(a) Nanocrystalline ductilization

Fan et al. found that the as-quenched BMGs $Zr_{53}Ti_5Ni_{10}Cu_{20}Al_{12}$ and $Zr_{60}Cu_{20}Pd_{10}Al_{10}$ included nanocrystals with an average grain size of ~ 2 nm embedded in the amorphous matrix, which exhibited significant plastic strains [58, 59]. The increased ductility was explained by the multiplication of shear bands due to the stress concentration in the vicinity of the nanocrystals [58, 59]. Kim et al. found that $Ti_{40}Zr_{29}Cu_8Ni_7Be_{16}$ BMGs crystallized by forming a few 3–5-nm-sized quasicrystals with the volume fraction of ~ 7 % in the amorphous matrix, enabling the fabrication of quasicrystal-reinforced MGMCs. The stable low-energy interface between the glass matrix and quasicrystals may act as a source for the multiple-shear-band formation, corresponding to plastic strains larger than 6 % at room temperature [60]. Inoue et al. found that the as-cast $Cu_{50}Zr_{50}$ BMG can sustain a compressive plastic strain of more than 50 % at room temperature, which is due to the compensation of any shear softening through nanocrystalline coalescence and pinning of shear bands [61].

Therefore, the improved plasticity can be obtained for nanocrystallite-reinforced MGMCs. It is generally proposed the ductilization effect of nanocrystals in the MGMCs is from a strong interaction between nanocrystals and local shear bands during deformation [62]. Nanocrystals can grow in shear bands, delocalize the shear, and deviate

and blunt cracks by the aid of *in-situ* deformation in the TEM analysis [63]. Several factors affect the overall mechanical behavior. The dominant effect is the presence of weak interfaces, which play a dual role in that they weaken the entire specimen and also provide multiple locations for shear-band initiation. A second factor is the resistance to the plastic deformation of the nanocrystallite, when a shear band tries to propagate through it. Such participation is neither the result of heating due to mechanical work nor due to the presence of compressive strains. Besides nanocrystallites, the nanoscale heterogeneity in BMGs can act as precursors for the formation of multiple shear bands [64-66]. Thus, shear banding is preferentially initiated at the interfaces or soft regions, and these shear bands can distribute the applied strain more homogeneously, resulting in the enhanced plasticity.

(b) Dendrite or Ta solid-solution ductilization

The first *in-situ* ductile-metal (dendrite)-reinforced MGMC based on glass-forming compositions in the Zr-Ti-Cu-Ni-Be system had been successfully developed by Hays et al. in 2000 [67]. Primary dendrite growth and solute partitioning in the molten state yielded a microstructure consisting of a ductile crystalline Ti-Zr-Nb β phase, with a body-centered cubic (bcc) structure, in a Zr-Ti-Nb-Cu-Ni-Be bulk metallic glass matrix, which resulted in a dramatic increase in the plastic strain to failure, impact resistance, and toughness of the metallic glass. This kind of MGMCs open the possibility of producing an entirely new class of metallic materials with high strength, toughness, and fatigue-resistant, which can combine the high strength of the metallic-glass matrix with the ability to undergo plastic deformation under unconfined or otherwise unstable loading conditions.

Figure 3(b) shows a dual-phase microstructure containing β-phase dendrites in a glass matrix, and an estimated fraction is ~ 25 vol.% of β phases, which is identified by the XRD peaks in the inset image [67]. Upon cooling from the high-temperature melt, the alloy undergoes the partial crystallization by the nucleation and subsequent dendritic growth of the β phase in the remaining liquid. In order to provide a deep understanding of the designing of such kinds of dual-phase composites, a pseudo-binary phase diagram for the *in-situ* β-phase-reinforced composites had been constructed by Lee et al. [68] Moreover, a series of plastic Zr-based MGMCs have been designed, based on a pseudo ternary phase diagram with apexes of zirconium, (titanium + niobium), and X, where X represents the moiety of $Cu_5Ni_4Be_9$ [67, 69], as displayed in Figure 4. Four compositions are on a line in the phase diagram, which can be written as $(Zr_{75}Ti_{25-x}Nb_x)_{100-y}X_y$. The $Zr_{41.2}Ti_{13.8}Cu_{12.5}Ni_{10}Be_{22.5}$ BMG (Vit 1) lies on the same line with x = 0 and y = 45. If the value of x is fixed to 6.66 and the value of y varies (y = 20, 22, 25, and 28, respectively), different MGMCs can be prepared. Figure 5 shows the X-ray diffraction patterns of four samples with different compositions in Figure 4, labeled as Zr54, Zr56, Zr58, and Zr60, respectively, [69]. It can be identified that the β-Zr phase with a bcc structure is detected, and its diffraction peaks are superimposed on the broad diffuse scattering from the glassy matrix. The crystal-plane indices of the β-Zr phase corresponding to diffraction peaks are marked in Figure 5.

Figure 6 presents the SEM images of the cross sections of the prepared MGMCs [69]. For the Zr54 alloy, very few dendritic phases distributes in the glassy matrix, as shown in Figure 6(a). For the Zr56 alloy, the dendrites with a very fine microstructure possess a volume fraction of ~ 50 %, as displayed in Figure 6(b). Figure 6(c) exhibits a

well-developed dendritic morphology for the Zr58 alloy, and the characteristic spanning length of an individual dendrite is ~ 20 μm. The dendrites have a volume fraction of ~ 55 % for the Zr58 alloy, which are homogeneously distributed in the amorphous matrix. The typical dendritic morphology develops in the glassy matrix in the Zr60 alloy, as displayed in Figure 6(d), with the dendrites volume fraction of ~ 60 %. As designed above, the slight tuning of atomic ratios dramatically change the microstructure, which gives a reminder that the chemical compositions of glass-forming alloys should be carefully controlled to avoid the full crystallization of amorphous matrix.

The compressive engineering stress-strain curves of designed alloys are displayed in Figure 7(a) [69]. The yielding strength (σ_y), the yielding strain (ε_y), the ultimate strength (σ_{max}), and the fracture strain (ε_f) of these MGMCs together with mechanical properties of Vit 1 are summarized in Ref. [69, 70]. Compared with the fracture strain of Vit 1 alloy, all the four MGMCs are significantly improved, due to the transfer of the local stress concentration to the surrounding glass, upon the yielding of β-Zr phase under loading [67]. Moreover, all these four MGMCs exhibit the work-hardening behavior during plastic flows. The tensile engineering stress-strain curve of the Zr60 alloy is shown in Figure 7(b) [71]. It can be observed that the ultimate tensile strength is ~ 1,480 MPa, and tensile fracture strain is ~ 2.9 %. During the past 15 years, many such dendrite / MGMCs are successfully designed, which exhibit improved macroscopic ductility and high strength at room temperature, together with the high thermal stability of the amorphous matrix [72]. They have been reported in the dendrite / Zr-based [29, 31, 67-71, 73-76], dendrite / Ti-based [30, 77-83], dendrite / Co-based [84], dendrite (flake) / Mg-

based [85], dendrite / La-based [86, 87], dendrite / LaCe-based [88], and dendrite / Fe-based MGMCs [89, 90].

In *in-situ* ductile crystalline-reinforced composites, the characteristic morphology of crystalline phases is mainly dendritic, and the bcc dendritic β-Zr and β-Ti solid solutions are most popular in Zr- and Ti-based MGMCs, with Ta particle-reinforced in the matrix. In 2002, Fan et al. had discovered precipitated micron-scale Ta-rich solid-solution particles distributed in a metallic glass matrix during melting of the master alloy of the glass-forming $(Zr_{70}Ni_{10}Cu_{20})_{82}Ta_8Al_{10}$ BMG [91]. The microstructure of the as-cast composite samples is shown in Figure 3(c) [91]. Particles of the Ta-rich solid solution, with an average size of 10 – 30 μm and volume fraction of about 4 %, are dispersed throughout the glassy matrix. Compared to dendrite composites, the differences between them are manifested not only in the morphology, but also in the chemical constituents. In the developed dendrite composites mainly, including Zr- and Ti-based BMG matrix, the β solid solutions are composed of Zr, Ti, and Nb for the Zr-based matrix, Ti, Zr, and V for the Ti-based matrix, and Zr and / or Ti occupy the most atomic percent [79, 92]. However, in *in-situ* Ta-reinforced composites, only a few elements can dissolve into bcc Ta particles [91, 93, 94]. Ta has a melting temperature near 3,000 degrees, and tends to precipitate prior to other elements with lower melting temperatures upon cooling. Although the differences between dendrites and Ta particles obviously exist, the function of these two reinforcements during plastic deformation is the same. These Ta-rich particles serve more than as traditional force carriers in the composites but as the main obstructions for the shear-band propagation [91, 93-96]. Finite-element analysis (FEA) demonstrates that homogeneously-dispersed Ta-rich particles form a network in the

matrix to effectively localize shear banding and, thus, avoid catastrophic failures [96]. The deformation behavior of the dendrite MGMCs would be investigated in detail in Section 3.

After the introduction of formation mechanisms of MGMCs, the mechanical properties could be controllably tailored by tuning the microstructure. Figure 8 presents the variation of the tensile ductility, e_T, as a function of the crystalline fraction, V_c, in the $Cu_{47.5}Zr_{47.5}Al_5$ MGMCs [97]. The e_T of MGMCs achieves its maximum value in the crystallinity range of ~ 40 % – 70 % and decreases steeply on both sides of the plateau. Recent studies have revealed that there exists a topological transition at a statistically-critical microstructural condition in MGMCs [29, 80, 86]. This transition can be termed as the percolation and the transition point as the percolation threshold. The relationship between e_T and V_c can be calculated quantitatively using the percolation theory [98]:

$$e_T \propto (V_c^p - V_c)^{-\beta} \tag{3}$$

where V_c^p is the percolation threshold, and β is a power exponent [98].

In addition, the mechanical properties can be tailored by varying the microstructure via adding minor elements. Song [99] has systematically investigated in 11 CuZr-based alloy systems with 36 different compositions. It can be noticed that the addition of minor elements has greatly affected the microstructure and mechanical properties of MGMCs. Wu et al. found that the twinning property of the reinforcing crystals could be dramatically improved by reducing the stacking fault energy through microalloying, which effectively alters the electron-charge density redistribution on the

slipping plane [100]. Consequently, minor additions of Co can dramatically improve the tensile ductility with a value of ~ 7 % and work-hardening capability of MGMCs.

2.1.3 Fabrication of bulk metallic glasses and composites

(a) Fabrication of monolithic BMGs

As introduced above, Au-Si binary amorphous alloys have been successfully quenched via high cooling rates in the 1960s [1]. Later, amorphous alloys were mainly developed in the form of ribbon or strip types by melt spinning [5]. In 1970s, some BMGs with low critical cooling rates have been discovered. For example, Drehman et al. synthesized $Pd_{40}Ni_{40}P_{20}$ BMGs with a slow cooling rate of 1.4 K / s on a fused silica surface [4]. In 1990s, to produce BMGs with a thickness above 10 mm, copper-mold suction casting [13], water quenching of a melt in a quartz tube [12], and unidirectional zone melting by the usage of arc melting as a heat source [101] were widely employed by Inoue et al. Up to now, copper-mold suction casting is the most common approach to fabricate BMGs, which is illustrated in Figure 9. The suction-casting system consists of two chambers: an upper chamber, in which the alloy ingot is melted, and a lower chamber, which mainly consists of a copper mold. To cast a sample, an ingot of the desired composition is melted under the atmosphere of Ar gas. While the ingot is molten, the valve is opened, creating a vacuum in the mold chamber and sucking the molten alloy into the mold. As a result, the rod and plate samples or samples with even more complex shapes can be fabricated. Other types of copper-mold-suction-casting systems are the same in essentials, while can be different in minor detail. For example, from the arc melter in Liaw's group from The University of Tennessee, as shown in the inset in Figure

9 [102], it can be observed that the four-piece suction-casting die is sized to seat in the hearth leaving a 0.15 mm gap between the upper (crucible) portion and lower (mold) portion. With the development of large-size monolithic BMGs, all kinds of new methods appear, including the spark-plasma sintering [103], electromagnetic-vibration process [104], pulsed-laser forming [105], low-pressure die-casting [106], melt atomization and spray deposition [107], continuous casting [108], *etc*.

People have been always searching for strategies to optimize the glass-forming ability (GFA) by computer calculations [30, 109, 110], and employing advanced ways to pinpoint GFA [111, 112]. For example, Ding et al. [112] proposed a high-throughput strategy. Using this approach, the composition with the highest thermoplastic formability in the glass-forming system of Mg-Cu-Y is quickly identified. Despite an increasing theoretical understanding of glass formation, BMGs are predominantly developed through a sequential and time-consuming trial-and-error approach.

(b) Fabrication of ex-situ MGMCs

As described before, as early as in 1997, *ex-situ* particle-reinforced Zr-, and Cu-based MGMCs have been successfully synthesized by melt infiltration using an induction heating coil and then injected melts through a nozzle into a copper mold [35]. Figure 10 shows the schematic diagram of the apparatus [35]. In this method, the top-fill casting-liquid metal is forced downward by a pressurized gas into a preform, and particle-reinforced and fiber-reinforced MGMCs can be easily synthesized. Actually, this method has been extensively employed to synthesize metal and ceramic matrix composites [113, 114]. As the case of copper-mold suction casting to obtain BMGs, melt infiltration is the

most popular approach in the fabrication of *ex-situ* MGMCs [35-40, 115-125]. During melt infiltration, the extra pressure, the infiltration temperature, and melt / fiber interface have an important effect on the infiltration kinetics.

To follow the temperature evolution during infiltration, a representation of the thermal behavior of both the fibers and melt is required as well as for the combined composite. The enthalpy (H) of the composite can be derived via Eq. (4) [126]

$$H = \int_{298}^{T} (M_f C_f + M_m C_m) dT + (1 - f_s) M_m G_m \tag{4}$$

where M is the mass fraction, C the specific heat, f_s the matrix solid fraction, and G the heat of fusion. The subscript, f, denotes the fiber and m the matrix. In the case of the melt, a fixed melting point is used, at which the state change (e.g., phase transformation) occurs, leading to a large step in the resultant $H(T)$ function.

Moreover, the dual-phase boundary is of considerable importance in the consideration of the thermal evolution during infiltration. A concentric fiber / melt cell, consisting of the appropriate melt volume for the fiber radius (R_f) and fiber volume fraction (V_f), may be introduced for the consideration of heat transfer on the scale of a single fiber, the outer cell (R_c) radius given by the following Eq. (5) [126].

$$R_c = \frac{R_f}{\sqrt{V_f}} \tag{5}$$

Based on Eqs. (4) and (5), the effects of the infiltration temperature and melt / fiber interface on fabrication can be quantitatively analyzed, which reminders people to optimize the *ex-situ* MGMCs processing.

(c) Fabrication of in-situ MGMCs

Recently, considerable research efforts have been directed towards the development of *in-situ* MGMCs, in which the reinforcements are formed *in-situ* by exothermal reactions between elements and compounds [127]. Using this approach, MGMCs with a wide range of matrix materials (including aluminum, et al.) and second-phase particles (including borides, et al.) have been prepared. Due to the formation of ultrafine and stable ceramic reinforcements, the *in-situ* MGMCs are observed to exhibit excellent mechanical properties.

Contrary to conventional *in-situ* MGMCs, the ductile phase is the secondary phase in *in-situ* MGMCs, for example, dendrites and Ta solid solutions, rather than the glassy matrix. These secondary phases play an important role in the ductilization of monolithic BMGs. The high strength originates from the network structure of the amorphous matrix. From the first *in-situ* dendrite MGMCs [67, 70], it have been noticed the heterogeneous distribution of secondary phases from the outer surface to the center of specimens [69, 92, 128-130]. Kong et al. [128] has found that the secondary dendrite arm spacing (SDAS) closely depends on the cooling rate, and an increased SDAS dominates from the outer surface to the center. Even if the composition is fixed, different microstructures, including the size and volume fraction, could be obtained, related to the different cooling rates by using different-sized molds [131]. For the synthesis of the

homogeneous *in-situ* MGMCs, copper-mold casting has not been the best choice yet. Therefore, several approaches are proposed to solve this problem (inhomogeneous microstructures), and homogeneous *in-situ* MGMCs can be obtained.

i) Semi-solid processing

In 2006, an innovative method was developed, based on the controlled solidification in the liquid-solid dual-phase region to produce spherical crystalline particles homogeneously dispersed in the amorphous matrix [132]. The synthesized composites by this semi-solid processing method exhibit the improved toughness. The spheroidization makes the crystals coarsen, which can more effectively increase cracking resistance [132-134]. Later, the ductile spherical crystal / metallic glass has been found in Qiao's group [133]. Therefore, semi-solid processing has been recognized as a good candidate to fabricate *in-situ* MGMCs with uniform microstructures.

Overall, the tips to prepare MGMCs by semi-solid processing are refered to be the following steps: (1) selecting a highly-processable BMG system with large GFA and finding a dendrite that forms in equilibrium with the glass-forming liquid; (2) processing the dual-phase alloys between the solidus and liquidus temperatures, which will coarsen the dendrites, create a uniform microstructure; and (3) quenching rapidly to vitrify the remaining liquid and form a dual-phase composite consisting of an amorphous matrix with ductile secondary phases. As the extension of semi-solid processing, thermoplastic processing [135] and semi-solid forging [136] are well developed to produce near-perfect replications and net shapes.

ii) Bridgman solidification (unidirectional solidification)

Bridgman solidification has been widely employed to synthesize conventional crystalline alloys, since the microstructure can be controlled by tailoring the temperature gradient and withdraw velocity [137]. By varying the withdrawal velocities in a controlled manner, the alloys with tailorable volume fractions and sizes of crystalline phases are obtained, owing to the variation of the cooling rates. Furthermore, the distribution of the crystalline phase is still homogeneously attributed to the availability of the invariable cooling rates, since the direction of the thermal conduction and extraction is mainly along the longitudinal direction for rod-shape samples obtained by the Bridgman solidification. The early study on the formation of MGMCs by the Bridgman solidification was mainly carried out in La-based alloy systems, and precipitated α-La dendrites were as the reinforcement [87, 138-141].

Later, significantly ductile high-strength Zr-based [29, 53, 129, 133, 142-144] and Ti-based MGMCs [80, 145, 146], consisting of amorphous matrix and ductile bcc dendrites, are prepared employing the Bridgman solidification by Qiao et al. It is illustrated in Figure 11 [147], which consists of an induction coil, a quartz tube, a heat insulator, a graphite heater, and a liquid Ga-In-Sn alloy with a water-cooled bath. After heating to the required temperature and holding for several minutes, a sample was directionally solidified into the liquid Ga-In-Sn alloy with a withdraw velocity of v. The cooling rate ($R_{cooling}$) could be calculated, according to the equation of $R_{cooling} = G_T v$.

Figure 12(a) [53] displays the XRD patterns of the $Zr_{37.5}Ti_{32.2}Nb_{7.2}Cu_{6.1}Be_{17.0}$ composites fabricated by the Bridgman solidification with different velocities, v = 0.2 -

1.5 mm / s. It can be observed that the peaks for the bcc β-Zr phases are superimposed on the broad diffuse-scattering amorphous maxima, when the v increases to 0.5 mm / s or higher, and the crystal-plane indices of the β-Zr phase corresponding to peaks are marked. The DSC results for $Zr_{37.5}Ti_{32.2}Nb_{7.2}Cu_{6.1}Be_{17.0}$ composites are shown in Figure 12(b) [29, 53]. The samples with v ≥ 0.5 mm/s exhibit a glass transition, followed by a single exothermic event during continuous heating, which is an indicator of an eutectic crystallization event. However, no glass transition and exothermic event are observed for the sample with v = 0.2 mm / s, indicating that this composite is only composed of the crystalline phases. The heat of crystallization in these composites relative to the heat of crystallization in the matrix alloy is an estimation of the volume fraction of the glass [31]. Therefore, the analysis of the heat of crystallization of the glass matrix of the composites compared with that of the matrix of DH1 alloy (ΔH_x = 100.90 J / g) gives a direct estimate of the volume fractions of β-Zr dendrites to be 64 %, 43 %, 42 %, and 40 % corresponding to v of 0.5, 0.8, 1.0, and 1.5 mm / s, respectively.

The microstructure of the sample with v = 1.0 mm/s is illustrated in Figure 13(a) [29]. It can be observed that dendrites homogeneously disperse in the glass matrix. An individual dendrite tree is indicated in the inset of Figure 13(a), which has a spanning length, s (μm), of ~ 330 μm. The dependences of spanning lengths of individual dendrite trees on varied withdrawal velocities are shown in Figure 13(b) [29], which roughly obeys a linear relationship. The relationship between s and v is approximately expressed by the following equation.

$$s = -239v + 588 \quad (6)$$

By controlling the withdrawal velocities, the sizes of dendrites have been effectively tailored, which verifies that the microstructures of the MGMCs can be tuned by the Bridgman solidification even when the composition is fixed. In addition, with the increase of withdrawal velocities, i.e., the increase of cooling rates, the growth of dendrites is suppressed, leading to the decrease of volume fractions of dendrites. Figure 13(c) plots the dependences of the fracture strengths and the plastic strains of the MGMCs developed by the Bridgman solidification on v. It is noted that the mechanical data are collected from Ref. [29]. All the composites by the Bridgman solidification have high fracture strength ($>$1,700 MPa) and exhibit the large plasticity. The bended specimen is exhibited in the inset in Figure 13(c). The crack does not happen during bending until the bending angle is approaching 130 degree, which also demonstrates that the Bridgman solidification is a good approach to adjust and optimize the mechanical properties of the *in-situ* MGGCs.

Therefore, both the semi-solid processing and Bridgman solidification can yield a uniform "near-equilibrium" dual-phase microstructure throughout the specimens, leading to the improved ductility. Through tuning the compositions of the composites, different scaled and volume-fractioned dendrites in the glass matrix can be obtained, and the enhanced ductility and toughness can be achieved.

2.1.4 Summary

This section clarifies the development history of MGMCs. According to the reinforcement phases in the glass matrix, the classification of MGMCs is schematically illustrated in Figure 14 [147]. It can be noticed that artificially introducing *ex-situ*

reinforcements with high melting temperatures into the glass-forming melts makes *ex-situ* MGMCs. Spontaneously, the partial crystallization of glass-forming melts yields *in-situ* MGMCs. Moreover, advanced approaches to fabricate homogeneous *in-situ* MGMCs are in expectation, other than the semi-solid processing and Bridgman solidification.

2.2 Thin-film metallic glass

According to reported data [32, 33, 148-152], TFMGs have been used extensively to improve the mechanical behavior of various substrate materials, especially in the field of wear resistance and hardness, without adversely affecting their desirable properties [149]. Numerical studies have reported that the fatigue behavior of the film/substrate system is closely dependent on film properties, such as structure, composition, thickness, hardness, ductility, and film/substrate interfacial adhesion, et al. [153-155]. Therefore, the fatigue behavior of various TFMG-substrate systems will be reviewed in this section, in which the film properties and film/substrates adhesion are investigated in detail.

Zr-based TFMG on 316L stainless steel: Figure 15(a) shows the stress-fatigue life (S-N, in which S is the applied stress and N is the number of cycles to failure) curves of 316L stainless steels coated with Zr-based TFMGs ($Zr_{47}Cu_{31}Al_{13}Ni_9$, at.%) of two different thicknesses (200 nm and 1 μm). It can be observed that both TFMG-substrate systems could improve the fatigue life of the steel substrate, while the 1-μm-thick-TFMG case has a better performance in improving the fatigue life and strength of the substrate. The fatigue-endurance limits of the bare-steel substrate, and substrates coated with 200-nm- and 1-μm-thick films are 700 MPa, 750 Mpa, and 775 Mpa, respectively. Noted that the fatigue-lifetime improvement is generally much more significant at lower stress levels

in Figure 15a, however, only limited beneficial effects of the TFMG on the fatigue life improvement can be observed at high stress levels [155].

To investigate the deformation mechanisms of the TFMG-Steel material system, the fractography of a 200-nm-thick Zr-based TFMG specimen after fatigue fracture is characterized by SEM, as exhibited in Figure 16(a) and (b) [155, 156], in which fatigue-crack-initiation and crack-propagation regions can be observed on the fracture surface. Figure 16(a) shows that the cracks initiate from the film/substrate interface zones and propagating inward, as indicated by the arrows. After large plastic deformation and final fatigue fracture, the TFMG remained well adhered with the substrate without remarkable cracks observed in the TFMG, shown in Figure 16b. It is good indication of the excellent film/substrate adhesion under fatigue loading, which is attributed to the outstanding film ductility accommodating bending deformation of substrate. However, slightly film delamination can be observed on the fractured specimens with 1-μm-thick Zr-based TFMG, illustrated in Figure 16(c) and (d) [155, 156], due to slip deformation in the substrate travelling to the film/substrate interface.

Zr-based TFMG on HAYNES C-2000® Ni-based alloys: Figure 15(b) exhibits the S-N curves of Zr-based ($Zr_{47}Cu_{31}Al_{13}Ni_9$, at.%) TFMG-coated Ni-based alloy substrates with two different film thicknesses (200 nm and 1 μm), as well as the bare substrate [156, 157]. Remarkable beneficial effects on the fatigue life of the Ni-based alloys are observed for both the 200-nm and 1-μm-thick cases, especially the improvement at lower applied stresses. Moreover, the fatigue-life and fatigue-endurance-limit improvements tend to be slightly higher for the 200-nm case than the 1-μm case.

The fractography of the Ni-based alloy with Zr-based TFMG after fracture is similar with that of steel coated with Zr-based TFMG, which is illustrated in Ref. [155]. The fatigue crack initiates from the coated surface and propagates inward. After fatigue failure, the Zr-based TFMG remains well adhered in the Ni-based alloy substrate.

Zr-based TFMG on Zr-based alloys: The S-N curves of Zr-based alloys ($Zr_{96.5}Hf_{4.5}$, wt.%) coated with a Zr-based TFMG ($Zr_{47}Cu_{31}Al_{13}Ni_9$, at.%) at different thicknesses (200 nm and 1 μm), as well as bare substrates, are displayed in Figure 15(c), which shows that both the 200-nm- and 1-μm-thick Zr-based TFMGs can improve the fatigue-life and fatigue-endurance limit of the Zr-based alloy substrates. The enhancement of the fatigue life is more significant for the 200-nm-thick film case, compared with the 1-μm-thick film case, especially at high stress levels. The fractographs of Zr-based-TFMG-coated Zr-based alloys are exhibited in Figure 17. In Figure 17(b), the fracture surface shows that the crack initiates from the corner of the tensile side and propagates inward, as indicated by white arrows. The adhesion between the film and substrate is displayed in Figure 17(a), which shows partial film delamination near the fracture region, resulting from severe slip deformation of the Zr-based alloy substrate under fatigue deformation.

Zr-based TFMG on Al alloys: The heat-treated Al-based alloy (7075-T6) substrates were deposited with a 50-nm-thick Ti adhesive layer plus a 200-nm-thick Zr-based [$(Zr_{53}Cu_{30}Al_8Ni_9)_{99.5}Si_{0.5}$, at.%] TFMG. The S-N curves of the Al-based alloy film/substrates systems, as well as the bare substrates, are shown in Figure 15(d) [152].

The results reveal that the coated specimen exhibit much improved fatigue life and strength, compared to the bare substrate, especially at low stress levels.

Typical SEM fractographs for fracture surfaces of the Al-based film/substrate system, as well as bare substrates, deformed at σmax. = 300 and 350 MPa are shown in Figure 18 [152], in which it can be observed that the fatigue-fracture surfaces are consisted of three distinct regions: (I) crack initiation on the tensile surface, (II) crack propagation, and (III) final-fast-fracture regions. The top view of the coated surface is shown in Figure 19 [152], which reveals that the overall TFMG remains intact, indicating good film/substrate adhesion, after severe four-point-bending deformation [Figure 19(a)], although slightly film delamination is found to be associated with fatigue cracks [Figure 19(b)]. A TEM cross-sectional image of the failure specimens, after the fatigue test at σmax. = 350 Mpa, is illustrated in Figure 20 [152], which can be observed that a pimple-like protrusion appears on the film surface, when PSBs propagate to the film/substrate interface and, eventually, form a crack. The pimple-like protrusion results from the step-like offsets appearing at the film/substrate interface during the fatigue test [152]; are mainly attributed to dislocations pileups and PSB formation in the substrate.

Zr-based TFMG on Ti-based alloys: Figure 15**(**e) [158] shows S-N curves of the Ti-6Al-4V substrates with and without coatings. Three kinds of coating materials with the thicknesses of 200 nm are used: TiN, single-layer $Zr_{50}Cu_{27}Al_{16}Ni_7$ (at.%) TFMG, and bilayer TFMG/Ti coatings. The S-N results indicate that fatigue life of Ti-based alloys is improved for all three cases, among which the TFMG/Ti bilayer case exhibits the best fatigue lifetime and endurance limit.

To investigate the fatigue mechanism of this Ti-based alloy film/substrate system, a series of cross-sectional TEM graphs [Figure 21(a)-(d)] are obtained, together with the AFM images of the surface morphology [Figure 21(e)-(h)] at various fatigue cycles with $\sigma_{max.}$ = 675 Mpa [158]. In Figure 21(a), the columnar structure of the as-deposited TFMG is clear. The corresponding AFM morphology image in Figure 21(e) exhibits a smooth surface, before fatigue loading. Figure 21(b) and (c) show that the columns or domain slipped along the boundaries, due to slip bands piled up and subsequent offsets formed in the substrate, with the corresponding morphology images displayed in Figure 21(f) and (g), revealing the bubble-like surface morphology, at the fatigue cycles of 5×10^5 and 5×10^6, respectively. Figure 21(d) and (h) present the morphologies of a failed specimen at 6.4×10^6 cycles, as a slip plane stacked up during the fatigue test. Therefore, the film roughness increased with fatigue cycles, ultimately leading to the film peeling off.

Moreover, the film properties can affect the film/substrate adhesion in the film/substrate system, which will result in the dramatic difference in the fatigue behavior of the film/substrate system. For example, TFMGs having good adhesion with crystalline substrates, such as Zr-based and Cu-based TFMGs, can increase the fatigue behavior of substrate materials, while poor film adhesion with the substrate, such as the Fe-based TFMG, will not significantly increase the fatigue behavior of substrate materials.

In film/substrate materials, fatigue-fracture surface occurs in three stages: fatigue-crack-initiation at the tension (coating) surface of the specimen (Stage I), crack propagation through the whole sample (Stage II), and the fast-fracture-stage, as shown in

Figure 16 [156]. In general, the surface-crack-initiation stage, usually initiated from the tension surface, plays a major role in affecting the fatigue behavior of film/substrate materials under HCF loading. The fatigue life and strength of the coated 316L stainless steel, Ni-based alloys, Zr-based alloys, and Al-based alloys can be improved by Zr-based TFMGs at a low stress level, which is mainly attributed to the lifetime extension at the fatigue-crack-initiation stage. Nevertheless, the TFMG coating does not have significant influence on the fatigue resistance of the substrate once a fatigue crack propagates.

Therefore, fatigue-resistance enhancement is attributed to lifetime extension in the fatigue-crack-initiation stage, mainly due to the deformation of substrates accommodated by the good ductility of thin films. Thus, the interaction between the film and the slip deformation in the substrate is extremely important in understanding the fatigue behavior of TFMG/substrate material systems. According to the interaction behavior of the slip-band/film occurring at the film/substrate interface, a fatigue-crack initiation mechanism can be proposed in Figure 22 [156, 159]. When PSBs or/and dislocation-pileups in the substrate arrive at the film/substrate interface, surface offsets will appear, which are potential sites for fatigue-crack initiation. Furthermore, the interaction between the slip bands and TFMG could lead to the activation of multiple narrow bands in the TFMG, which were believed to be the sites for shear-band nucleation and multiplication in TFMGs, thus preventing the catastrophic failure by single shear-band propagation and improving thin-film ductility. Consequently, it will take more fatigue cycles for a fatigue crack to initiate, and result in the increased fatigue life of TFMG/substrate material systems.

2.3 Motivation and Scientific Issues

Despite of the desirable properties of BMGs, there are several critical issues needed to be addressed before the application of BMGs as structural materials, especially the plasticity and fatigue behavior, even considering the improved mechanical properties for MGMCs and TFMGs. Firstly, the plasticity of MGMCs can be greatly improved, due to dispersed inclusions in the metallic-glass matrix. However, the micro mechanisms for the improved plasticity of BMGs are still far from satisfactory understanding. Second, the fatigue behavior of different TFMG-substrate materials can be further studied with the four-point-bending and tensile loading methods, since very limit clues are reported on the relationship between fatigue behavior and critical factors of TFMG-substrate materials, such as the film composition, film/substrate adhesion, film thickness, and surface roughness, et al. Finally, the micro mechanisms responsible for the TFMG-substrate materials need to be further investigated with transmission electron microscopy (TEM) to characterize the interface of the TFMG-substrate and FEM to simulate the shear-band initiation and propagation in TFMGs, which in turn can help us to design better TFMG-substrate materials.

CHAPTER III
METALLIC-GLASS-MATRIX COMPOSITES

3.1 Introduction

Despite the unique properties of BMGs, most monolithic BMGs have limited macroscopic plasticity prior to the catastrophic failure, which greatly restricts their structural applications. To date, macroscopic ductility has been obtained only for monolithic metallic glasses with nanoscale dimensions (e.g., nanopillars) due to homogeneous deformation rather than local shear banding at room temperature [160, 161]. For engineering applications, larger BMG specimens (e.g., a millimeter scale) with the improved ductility are imperative. To circumvent the rapid propagation of shear bands within BMG samples, a new class of metallic-glass-matrix composites (MGMCs), with soft body-centered cubic (BCC) dendritic crystals as the reinforcement phase dispersed in the metallic-glass (MG) matrix, has emerged with improved ductility, as shown in Figure 24 [30, 70]. Compared to the traditional MGMCs with particle-like crystalline inclusions in the MG matrix [95, 162-165], the typical characteristic of this kind of composite is that a large amount of dendritic single crystals with random crystallographic orientations precipitate in the metallic-glass matrix. Some studies have been conducted to investigate the mechanical behavior of these novel MGMCs under various loading conditions. For example, Hofmann et al. [31] and Qiao et al. [30, 166-168] found that the MGMCs had substantially improved compressive and tensile ductility, compared to monolithic BMGs. The improved toughness and ductility of these MGMCs are commonly believed to be caused by blocking the propagation of shear bands through

soft crystalline phases under loading, as revealed in Figure 25 [169]. This mechanism can be revealed by post-mortem observations, while only limited in-situ studies have been performed by synchrotron X-ray and neutron-diffraction measurements on the microstructural origin of these deformation mechanisms [164, 170-173].

Owing to the excellent penetration capability, X-ray diffraction techniques have been widely used to study the effects of material microstructures and loading conditions on the deformation behavior of polycrystals [30, 174-180]. In the X-ray diffraction, the lattice strain can be calculated from the shift of diffraction peaks, which corresponds to the elastic lattice distortion of grains in different crystallographic directions. From the micromechanics standpoint, the lattice strain relies on the intergranular interactions of the inhomogeneous deformation fields in neighboring grains, which is called Type-II strains [181]. In diffraction analyse, the lattice strain in the <hkl> direction, ε_{hkl}, is calculated from the interplanar spacing (d_{hkl}), based on the change of d_{hkl} before and after deformation, which can be measured from the [hkl] peak shift in the diffraction pattern. In elastic deformation, the evolution and anisotropy of ε_{hkl} are determined by the elastic anisotropy and texture of materials, while in plastic deformation, they are mainly contributed by plastic slips and intergranular interactions among neighboring grains. The deviation of the measured ε_{hkl} from the extrapolated curve of the measured elastic-elastic portion is denoted as intergranular strains [181, 182].

In the reported diffraction works, Balch et al. [170, 171] used synchrotron X-ray scattering to measure the lattice strains in crystalline reinforcements of MGMCs upon uniaxial compression. They examined the load transfer between the amorphous matrix and the second-phase particles during loading and unloading, and found that the

crystalline phase yielded before the matrix, decreasing the fraction of the subsequent load transferred to crystals. Ott et al. [164] studied the elastic-strain evolution of the particle-enforced MGMCs in the single-crystal direction using the synchrotron X-ray diffraction and finite-element modeling (FEM) during compression loading. As compared to our dendritic composite, the second phase is softer than the MG matrix, but the deformation mechanisms are very different when strain localization appears in the matrix. Their simulations are based on continuum Mises plasticity without any reference to the plastic anisotropy. Clausen et al. [172, 173] investigated the lattice-strain evolution of dendrite-crystal-strengthened MGMCs by neutron diffraction and self-consistent models. Their self-consistent model is based on the Eshelby inclusion model and gives a neat treatment of how a crystalline grain deforms within other grains, which clearly has difficulties in describing dendritic crystals. Deformation in the matrix involves strain localization, which again cannot be addressed by the self-consistent model. We note that the synchrotron X-ray diffraction measurement has unique advantages, compared to the neutron diffraction with respect of resolution, which tends to be more sensitive to structural disorder and fluctuations, and allows the background intensities between peaks to be estimated more reliably [183].

Bulk metallic glasses (BMGs) exhibit many desirable properties, e.g., high strengths and hardness, large elastic limits, and excellent corrosion and oxidization resistance [7, 8, 19, 22, 155, 184, 185], which make them potential candidates as new structural materials. However, BMGs are notorious for their brittle nature upon loading due to the formation of highly localized shear bands. In a monolithic BMG, a major shear band will run through the entire sample once it initiates from some weak locations. To

circumvent this disadvantage, a class of metallic-glass-matrix composites (MGMCs), with ductile dendritic crystalline phases dispersed in the metallic-glass (MG) matrix, has emerged with improved toughness, due to the stabilization against shear localization and propagation of critical shear bands upon loading.[17, 30, 31, 70, 88, 168] The primary objective will be clearly directed to how to design such a microstructure and control the internal strain fields so that the ductility enhancement can be manipulated.

A number of studies have been conducted to investigate the deformation mechanisms in the dendrite-dispersed MGMCs. For example, Hofmann et al.[31] and Qiao et al. [30, 83, 166-168] found that the MGMCs had substantially improved malleability and tensile ductility compared with monolithic BMGs, presumably by blocking the propagation of shear bands by soft crystalline phases in MGMCs under loading [29, 31, 67]. This mechanism can be revealed by post-mortem observations, while only limited in situ studies have been performed by synchrotron X-ray and neutron diffraction measurements on the microstructural origin of these deformation mechanisms [164, 170-173]. We note that the synchrotron X-ray diffraction measurement has unique advantages, compared to the neutron diffraction with respect of resolution, which tends to be more sensitive to structural disorder and fluctuations, and allows the background intensities between peaks to be estimated more reliably [183].

In the X-ray diffraction, lattice strain can be calculated from the shift of diffraction peaks, which corresponds to the elastic lattice distortion of grains in different crystallographic directions. From the micromechanics standpoint, the lattice strain relies on the intergranular interactions of inhomogeneous deformation fields in neighboring

grains, which is also called Type-II strains [181]. In diffraction analysis, the lattice strain in the <hkl> direction, ε_{hkl}, is calculated from the interplanar spacing (d_{hkl}), based on the change of d_{hkl} before and after deformation, which can be measured from the [hkl] peak shift in the diffraction pattern. In elastic deformation, the evolution and anisotropy of ε_{hkl} are determined by the elastic anisotropy and texture of materials, while in plastic deformation, they are mainly contributed by plastic slips and intergranular interactions among neighboring grains. The deviation of the measured ε_{hkl} from the extrapolated curve of the measured elastic-elastic portion is denoted as intergranular strains [181, 182].

In the reported diffraction works, Ott et al. [164] studied the elastic strain evolution of particle-reinforced MGMCs in single crystal direction using the synchrotron X-ray diffraction and finite element modeling (FEM) during compressive loading. Their simulations are based on continuum Mises plasticity without any reference to the plastic anisotropy in the inclusions, and also there is no reference to the strain localization in the matrix. Clausen et al. [172, 173] investigated the lattice strain evolution of dendrite-crystal-strengthened MGMCs by neutron diffraction and self-consistent models. Their self-consistent model is based on the Eshelby inclusion model and gives a neat treatment of how a crystalline grain deforms within other grains, which clearly has difficulties in describing dendritic crystals. Deformation in the matrix involves strain localization, which again cannot be addressed by the self-consistent model. Limitations in these literature works have prevented a full understanding of deformation mechanisms in these composites.

In the present work, a synergistic experimental/modeling study is reported to investigate the lattice strain evolution of crystalline phases in the dendritic-inclusion-dispersed MGMCs under in situ uniaxial compressive deformation in both elastic and plastic stages. The composition of the selected MGMC system is $Zr_{58.5}Ti_{14.3}Nb_{5.2}Cu_{6.1}Ni_{4.9}Be_{11.0}$ in atomic percent (at.%). The final microstructure of the MGMC, as shown in the scanning-electron-microscopy (SEM) image of Figure 27(a) [186], consists of metallic glass matrix and crystalline phase. During the transition from elastic to plastic deformation in the crystalline phase (~ 450 MPa under uniaxial compression), we are interested in the sequence of yielding in different grain families. In other words, which grains are "hard" or "soft" when the crystalline microstructure is dendritic and the surrounding matrix is elastic? During the transition from elastic to plastic deformation in the matrix phase (~ 1,450 MPa under uniaxial compression), the emphasis is placed on the load partitioning between the MG matrix and crystalline dendrites. For example, how would the shear bands affect the lattice strain evolution in the second phase? Deformation behavior was identified using high-energy synchrotron X-ray diffraction, with the schematic in Figure 27(b) [186] illustrating the experimental setup. Procedures to obtain representative diffraction results in Figure 27(c) and (d) [186] are explained in Section II.

Deformation mechanisms can be studied from a microstructure-based finite element method in which the crystalline phase and matrix are explicitly modeled in Figure 28 [186]. Appropriate geometric information (such as crystallographic orientation and shape) and constitutive models (including crystal plasticity for the inclusion and free-volume model for the matrix) can be assigned to the finite elements. The connection

between the synchrotron X-ray diffraction measurements and the finite element simulation lies on the lattice strain, which can be extracted by finding the grains that satisfy the diffraction condition, as schematically shown in Figure 28(c). Details of modeling and simulation, as well as lattice strain extraction procedure, are given in Section III. Lattice strains will provide the unprecedented information on the underlying deformation mechanism at microstructural scales, and our explicit microstructure-based simulations differ from many previous studies in this class of materials. Consequently, effects of dendrite shape, crystalline orientations, and strain localization in the matrix on lattice strain evolution can be investigated and be used to understand the deformation mechanisms.

3.2 Experimental and Modeling Methods

3.2.1 Experimental Methods

(a) Sample Preparation

The MGMCs were prepared by arc-melting a mixture of Zr, Ti, Ni, Cu, Nb, and Be with purities greater than 99.9% in weight percent (wt.%) under a Ti-gettered argon atmosphere. The liquid alloys were sucked into a cylindrical copper mold with a diameter of 3 mm and a length of around 70 mm. Upon cooling from a high temperature melt, the alloy undergoes partial crystallization by nucleation and subsequent growth of the β phase in the remaining liquid, producing a two-phase microstructure containing β-phase dendrites in the MG matrix. The energy dispersive spectrometry (EDS) analysis revealed the compositions of the dendrites and the glass matrix to be $Zr_{66}Ti_{15}Nb_8Cu_{10}Ni_1$ and $Zr_{50}Ti_{13}Nb_3Cu_{20}Ni_{14}$, respectively. It should be note that element Be cannot be detected

by EDS, and it is almost all enriched in the MG matrix [167]. The volume fraction of the dendrites was found to be approximately 55% by analyzing the contrast in the SEM images. For mechanical experiments, the samples were still in a cylindrical geometry, and machined to 6 mm in length with an aspect ratio of 2:1. The ends of samples for mechanical tests were polished to a 1,200 grit SiC surface to ensure alignment.

(b) Synchrotron X-Ray Measurements

The high-energy synchrotron X-ray diffraction was carried out at the beamline, 11ID-C, of the Advanced Photon Source (APS), Argonne National Laboratory, USA. As schematically shown in Figure 27(b), a digital image plate (MAR 345, with a 200×200 μm^2 pixel size) was positioned 1,800 mm downstream from the sample to record the scattered intensity in transmission through the specimens, with a beam size of 0.2×0.2 mm^2. A two-dimensional ring pattern was recorded on the image plate, as shown in Figure 27(c). Scattering patterns were extracted by azimuthally averaging the ring pattern over an arc of approximately 5^{o} centered on the vertical (loading) direction using the *FIT*2D software [187]. The specimens were loaded incrementally in uniaxial compression using a motorized screw-driven load cell, and the data was collected automatically every 20 seconds, without stopping the load. All the samples were tested under compression at a strain rate of 2×10^{-4} s^{-1}.

The interplanar spacing of the [hkl] planes, d_{hkl}, was determined in terms of the Bragg's law, $d_{hkl} = \lambda / 2\sin\theta_{hkl}$, where $2\theta_{hkl}$ is the diffraction angle of different [hkl] planes and determined by fitting the position of an individual Debye cone on the diffraction spectra. Due to the high angular resolution of the synchrotron-based X-ray

diffraction technique, the slight shift of diffraction patterns could be tracked during the course of loading. The lattice strain, ε_{hkl}, can thus be obtained by

$$\varepsilon_{hkl} = \frac{d_{hkl} - d_{hkl}^0}{d_{hkl}^0} \tag{7}$$

where d_{hkl}^0 is the interplanar spacing in the undeformed state. The diffraction peaks of [110], [200], [211], [220], and [310] planes of the β phase in the MGMCs with a BCC structure before and after deformation are exhibited in Figure 27(d) under compressive deformation.

3.2.2 Finite-Element Modeling

(a) Microstructure-Based Finite Element Simulations

In contrast to the self-consistent model in which a grain of interest is embedded in an effective homogeneous medium [172, 173], the microstructure will be explicitly simulated with appropriate constitutive models assigned to each phase as shown in Figure 28. The crystalline phase can be assigned with a slip-based crystal plasticity model [181, 182], which describes the Schmid law, slip anisotropy, and hardening behavior. The constitutive parameters include elastic constants C11, C12, and C44, the critical resolved shear stress τ_0, and those describing strain-rate dependence and hardening behavior. Details are given in Section III (B). This model has been implemented in ABAQUS, a commercial finite element software, through the user-defined material (UMAT) subroutine [188], which has been modified further for the lattice strain analysis. The MG matrix can be assumed to be elastic-perfect plastic solids in some cases for the sake of

simplicity with the constitutive parameters of Young's modulus *E*, Poisson's ratio *v*, and yield stress σ_{BMG}^{Y}. However, at the late stage of deformation, the localized deformation in the narrow shear bands will give a stress field that cannot be faithfully described by the elastic-plastic model. To this end, we adopt the free-volume-based constitutive model for more elaborate studies since it is capable of capturing the shear-banding events [189, 190], with details given in Section III (C). This constitutive model has been implemented into ABAQUS using the UMAT subroutine in Ref. [189], which allows us to study the interaction between individual shear bands and the background stress fields [191, 192].

Compared to the traditional MGMCs with particle-like crystalline inclusions in the MG matrix [95, 162-165], the typical characteristic of this kind of composite is that a large amount of dendritic single crystals with random crystallographic orientations precipitate in the metallic-glass matrix. However, a full three-dimensional mesh of the dendritic microstructure in Figure 27(a) is not feasible because of the fine geometric details. Here, we adopt a uniaxial specimen in Figure 28(a) with 7,986 cubes. Half of these cubes belong to the MG matrix, while the other half is the crystalline phase, as shown in Figure 28(b). This configuration is close to the experimental condition, where the crystalline phases have a volume percentage of ~ 50% in the MGMC specimens. Each grain in Figure 28(b) has eight C3D8R elements with the same crystal orientation, in which the C3D8R element is a 3D reduced-integration hexahedral element. Note in Figure 27(a), each crystalline inclusion is dendritic and actually consists of multiple grains. All the crystalline grains are assigned with the same crystal plasticity constitutive

parameters but different crystallographic orientations. The boundary conditions in the present models are with an applied load at one end and pinned boundary at the other end.

The extraction and calculation of lattice strains, ε_{hkl}, are specified as follows. A subset of grains is selected, whose <*hkl*> directions are parallel (or within a small tolerance angle) to the diffraction vector, q. The tolerance, which is the maximum deviation between the <*hkl*> direction and q, is chosen in the simulations to ensure that a large amount of [hkl] grains could be selected to improve the statistical quality (e.g., $\pm 4°$ in our simulation). Figure 28(c) exhibits the selected grains with the <310> crystallographic orientation in the model. The lattice strain, ε_{hkl}, is a volume average of the projected elastic strain, given by [181]

$$\varepsilon_{hkl} = \frac{\sum_{N=1}^{N_{grain}} \int \varepsilon_{ij}^{elastic} q_i q_j d\Omega_N}{\sum_{N=1}^{N_{grain}} \int d\Omega_N} \tag{8}$$

where $d\Omega_N$ is the differential volume of the N^{th} grain and N_{GRAIN} is the total number of grains in <*hkl*> directions.

(b) Crystal Plasticity for Crystal Inclusions

In the slip-based crystal plasticity theory [193, 194], the crystal will yield when the revolved shear stress reaches a critical strength on a given slip system (i.e., the Schmid law), and the constitutive model also needs to specify the flow behavior and hardening law. From the kinematics point of view, the deformation behavior of the material elements is characterized by the deformation gradient,

$$F_{ij} = \frac{\partial x_i}{\partial X_j} \tag{9}$$

where x_i and X_i are the current (deformed) and initial coordinates, respectively. The total deformation gradient can be decomposed into elastic and plastic parts, $F_{ij}=F^e_{ik}F^p_{kj}$, where F^e_{ik} and F^p_{kj} denote elastic and plastic deformation components, respectively. The plastic rate of deformation is

$$\dot{F}^p_{ik}F^{p-1}_{kj} = \sum_{\alpha=1}^{n_s} \dot{\gamma}[\tau^{(\alpha)}, \tau^{(\alpha)}_{flow}]s^{(\alpha)}_i m^{(\alpha)}_j \tag{10}$$

where n_s is the total number of slip systems, $\dot{\gamma}$, and $m^{(\alpha)}_j$ are the shear rate, slip direction, and slip plane normal of the α^{th} slip system, respectively. The shear rate is a function of the resolved shear stress, $\tau^{(\alpha)}$, acting on the slip plane and the flow strength of the slip system, $\tau^{(\alpha)}_{flow}$. The resolved shear stress is computed as

$$\tau^{(\alpha)} = m^{(\alpha)}_i F^{e-1}_{ij} J\sigma_{jk} F^e_{kl} s^{(\alpha)}_l \tag{11}$$

where J = det(F^e). The elastic part of the deformation gradient is related to stress through

$$T_{ij} = C_{ijkl}E^e_{kl} \tag{12}$$

where $E^e_{ij}=\frac{1}{2}(F^e_{ki}F^e_{kj}-\delta_{ij})$ is the elastic Lagrange-Green strain, and T_{ij} is the material stress tensor, which is related to the Cauchy stress by

$$J\sigma_{ij} = F^e_{ik}T_{kl}F^e_{jl} \tag{13}$$

The Pierce-Asaro-Needleman's constitutive law is used to characterize the plastic flow and strain hardening, given by

$$\dot{\gamma}^{(\alpha)} = \dot{\gamma}_0 \left| \frac{\tau^{(\alpha)}}{\tau^{(\alpha)}_{flow}} \right|^n \operatorname{sgn}[\tau^{(\alpha)}] \tag{14}$$

$$\dot{\tau}^{(\alpha)}_{flow} = \sum_{\beta} h_{\alpha\beta} \left| \dot{\gamma}^{(\beta)} \right| \tag{15}$$

where the self-hardening modulus is given by

$$h_{\alpha\alpha} = h(\gamma) = h_0 \sec h^2 \left| \frac{h_0 \gamma}{\tau_s - \tau_0} \right| \text{ (no sum on } \alpha) \tag{16}$$

where h_0 is the initial hardening modulus, τ_0 is the initial yield stress, τ_s is the saturation slip strength (the stress at which the large plastic flow initiates), and $\gamma = \int_0^t \sum_{\alpha} |\dot{\gamma}^{(\alpha)}| dt$ is the total accumulated shear strain on all slip systems. The latent hardening moduli, $h_{\alpha\beta}$, are given by

$$h_{\alpha\beta} = h(\gamma)[q + (1-q)\delta_{\alpha\beta}] \tag{17}$$

where q is the ratios of latent to self-hardening.

To summarize, the constitutive behavior of crystals is characterized by a set of parameters, including the elastic constants in principal directions (C_{11}, C_{12}, and C_{44}), characteristic strain rate ($\dot{\gamma}_0$), stress exponent (n), initial yield stress (τ_0), saturated yield stress (τ_s), and initial hardening rate (h_0).

A. *Free Volume Model for the Metallic-Glass Matrix*

Following the Spaepen's free volume model [190], the stress-driven increase in the free volume reduces the viscosity, thus leading to strain softening behavior of MGs. In the pure shear case, the plastic-strain rate ($\dot{\gamma}^p$) is represented by

$$\frac{\partial \gamma^p}{\partial t} = 2f \exp(-\frac{\alpha v^*}{v_f}) \exp(-\frac{\Delta G^m}{k_B T}) \sinh(\frac{\tau \Omega}{2k_B T}) \tag{18}$$

where f is the frequency of atomic vibration, α is a geometric factor of order 1, v^* is the hard-sphere volume of an atom, v_f is the average free volume per atom, ΔG^m is the activation energy, Ω is the atomic volume, τ is the shear stress, k_B is the Boltzmann constant, and T is the absolute temperature.

The evolution of free volumes is determined by two competing processes during deformation: the stress-driven creation and diffusion-dominated annihilation. Thus, the net change rate of the free volume is given by

$$\frac{\partial v_f}{\partial t} = v^* f \exp(-\frac{\alpha v^*}{v_f}) \exp(-\frac{\Delta G^m}{k_B T}) \{\frac{2\alpha k_B T}{v_f C_{eff}} [\cosh(\frac{\tau \Omega}{2k_B T}) - 1] - \frac{1}{n_D}\} \tag{19}$$

where n_D is the number of atomic jumps needed to annihilate a free volume equal to v^*, and $n_D = 3$ in the present calculation, and the effective elastic modulus is $C_{eff} = E/3(1-\upsilon)$. Using the small-strain and rate-dependent plasticity framework, the plastic strain is assumed to be proportional to the deviatoric stress, as generalized from Eq. (18), while the temporal change in the free volume is also coupled with the Mises stress, as generalized in Eq. (19). This constitutive model allows us to study the interaction

between individual shear bands and between the shear bands and the background stress fields [191, 192].

3.3 Results and Discussion

A. *Lattice-Strain Evolution in MGMCs*

The compressive engineering stress–strain curve of a cylindrical MGMC specimen is shown Figure 29(a) [186]. Note that the compressive stress/strain is denoted as positive throughout this paper. Under quasi-static compressive loading, the composite exhibits at yield stress σ_y = ~ 1.5 GPa, with a corresponding elastic strain limit, ε_y = 1.2%. After further deformation, linear work hardening prevails until the failure occurs for the MGMCs specimen, with the fracture strength of σ_f = ~ 1,800 MPa and plastic strain of ε_y^p = ~ 5.6%. It could be noted that the yielding strength of the MGMCs is much higher than that of single β-phase specimens, which is ~ 450 MPa in the present case [167, 173]. But there is no indication of yield and subsequent plastic deformation of the second phase (β) from the macroscopic stress-strain curve in Figure 29(a).

Figure 29(b) displays the applied stress vs. the longitudinal lattice-plane-specific elastic strain (i.e., lattice strain) curves of the β-Zr crystalline phase in the MGMCs for [310] grains. Three stages of deformation can be identified. In Stage I (0 – 450 MPa, elastic-elastic stage), the lattice strain of the β-phase crystals increases linearly with the applied stress, since both the dendritic crystalline phases and MG matrix are under elastic deformation. In Stage II (450 – 1,480 MPa, an elastic-plastic stage), the β phase yields at around 450 MPa, and plastic deformation starts thereafter, which can be concluded from the deviation of lattice strains in this stage from the extrapolated straight line from Stage I.

In Stage III (1,480 – 1,550 MPa, a plastic-plastic stage), both the crystals and MG matrix deform plastically after 1,480 MPa, and the lattice strain decreases with the increase of applied stress thereafter, until the ultimate failure of MGMC specimens. We denote this lattice strain decrease in Stage III as a "turnover" phenomenon, which results from an elastic relaxation near the second phase. The microscopic mechanisms responsible for these three stages and their transitions will be investigated in details next.

B. *Elastic-Elastic Deformation of β-Zr Crystalline Phase and MG Matrix (Stage I)*

Figure 30 gives the measured stress - lattice strain curves of the β phase for several grain families [186]. In Stage I, when the applied stress is below 450 MPa, these curves are straight lines with different slopes, which are governed by the elastic constants of both the crystal and MG phases, the geometric shape of crystalline phases, and crystallographic orientations of these dendrites. In this work, the elastic constants (C_{11}, C_{12}, and C_{44}) can be fitted from the comparison between predicted and measured slopes of stress-lattice strain curves in Stage I. These slopes are denoted as k_{Exp}^{hkl} and k_{FEM}^{hkl}, respectively. The elastic constants are optimized to minimize the following objective function φ,

$$\varphi = (k_{Exp}^{200} - k_{FEM}^{200})^2 + (k_{Exp}^{211} - k_{FEM}^{211})^2 + (k_{Exp}^{220} - k_{FEM}^{220})^2 + (k_{Exp}^{310} - k_{FEM}^{310})^2 \quad (20)$$

The resulting elastic constants are C_{11} = 91.0, C_{12} = 69.5, and C_{44} = 31.0 GPa, while the reported elastic constants by the self-consistent model are C_{11} = 90.0, C_{12} = 68.0, and C_{44} = 33.0 GPa [172, 173].

C. *Elastic-Plastic Transition of the β-Zr Crystalline Phase (Stage II)*

When the second phase deforms plastically and the MG matrix deforms elastically, the lattice strains deviate from the straight lines extrapolated from Stage I, which can be characterized by the intergranular strains ($\Delta\varepsilon_{hkl}$) [181, 182],

$$\Delta\varepsilon_{hkl} = \varepsilon_{hkl}^{Experiment} - \varepsilon_{hkl}^{Extrapolation} \tag{21}$$

as plotted against the applied stress in Figure 31 [186]. The deviation is a result of load partitioning between "hard" and "soft" phases or grains [182, 195]. When two solids are under an isostrain condition (which corresponds to the Taylor model of a polycrystal in which all grains have the same strain field as the macroscopic one), the one with a high ratio of yield stress to modulus, σ_Y/E , will yield later and is the "hard" solid. Once the "soft" solid (with a low σ_Y/E) yields, the load will be supported by the "hard" solid so that the corresponding elastic strain in the "hard" solid significantly increases. In other words, the "hard" solid will experience positive intergranular strains, and the "soft" one with negative intergranular strains.

The load partitioning occurs not only between the two phases but also among the grains. As presented in Figure 31, at the transition from Stage I to Stage II, $\Delta\varepsilon_{200}$ is the most positive, and $\Delta\varepsilon_{220}$ is about zero, indicating that [200] grains are the "hardest", followed by [310] and [211] grains, while [220] grains are the "softest". The ''hardest'' [200] grains will carry more applied loads, and their further deformation will decrease the slope of the σ - ε_{200} curve in Stage II, as shown in Figure 30. In order to testify these

experimental results, the "hard" and "soft" crystal directions could be further demonstrated by calculations from the strength-to-stiffness ratio, r_{cry}^{hkl}, as given by [195],

$$r_{cry}^{hkl} = \frac{\sigma_Y^{hkl}}{E^{hkl}} = \frac{\tau_0}{m^{hkl} E^{hkl}} \tag{22}$$

where r_{cry}^{hkl} and m^{hkl} are the strength-to-stiffness ratio and Schmid factor in the <*hkl*> direction, respectively, and τ_0 is the critical resolved shear stress. The first grain family to yield will be the one with the lowest strength-to-stiffness ratio, which is the "softest" grain family. Three sets of slip systems for BCC materials, [110]<111>, [112]<111>, and [123]<111>, are considered in the present calculation. In Table 1, for the [110]<111> slip system, the "hardest" grain family is [200] with a r_{cry}^{hkl} value of 2.85 $\times 10^{-3}$, followed by [310] grains with a r_{cry}^{hkl} value of 1.67 $\times 10^{-3}$, and the [220] and [211] grain families are the "softest" with a r_{cry}^{hkl} value of 1.17 $\times 10^{-3}$. For the [112]<111> and [123]<111> slip systems, the "hardest" to "softest" grain sequence is [200], followed by [310] grains, then [220] and [211] grain families, and the r_{cry}^{hkl} values are all listed in Table 1. Therefore, [200] and [310] grain families are much "harder" than the [211] and [220] grain families for all these three slip systems. However, all the intergranular strains of [hkl] grains will become positive, when the applied stress increases to high enough (e.g., 1,000 MPa), since the MG matrix has a much higher r_{MG} value of 20.22 $\times 10^{-3}$ than the crystalline phases, indicating that the matrix is much "harder" than all the crystal grain families.

D. *Elastic-Plastic Transition Of the MG Matrix (Stage III)*

In uniaxial compression, when the applied stress reaches ~ 1,480 MPa, the deformation behavior of crystals enters the Stage III in Figure 29(b), in which both the MG matrix and crystal inclusions deform plastically. Then, the lattice strain in each crystalline orientation decreases with the increase of the applied stress until the ultimate failure of the MGMCs specimens.

Our initial ABAQUS simulations employ cubic grains of random crystal orientations and the elastic-plastic matrix to simulate the lattice strain evolution of crystals in MGMCs. The overall trends of the lattice-strain evolution of the crystalline phase in MGMCs can be obtained in Figure 32 [186] with both experimental and simulated results, after carefully choosing the constitutive parameters for the three families of slip systems, [110]<111>, [112]<111>, and [123]<111>, in the crystal-plasticity theory and for the Mises plasticity in MG matrix σ_{BMG}^{Y}, which are all listed in Table 2. In Figure 32, it can be observed that the simulation results have a good agreement with the experimental results in Stage I, while some discrepancy appears in Stages II and III. Although the simulation results exhibit some deviation from the experimental results in the end Stage II and Stage III, we obtain the same sequence of different grain families at various stress levels, such as 800 MPa, 1,400 MPa, and 1,500 MPa, i.e., red-blue-green-black ([220]-[211]-[310]-[200]) from left to right in Figure 32. The discrepancy near the end of Stage II may result from the highly idealized microstructure in simulations, as opposed to the actual dendritic structure, as well as from the hardening law that may not faithfully represent the deformation behavior in the crystalline phase.

Note that thermal residual stress might exist in the MGMCs, which is developed during rapid cooling due to the difference in coefficients of thermal expansion between the metallic glass matrix and dendrite crystals. The magnitude of thermal residual stress can be calculated using the Eshelby equivalent inclusion method [196]. The residual stress in MGMCs has been extensively reported in the range of 100 - 300 MPa for crystalline inclusions and less than 100 MPa in matrix [171, 197-200]. For the MGMCs in the present work, there is an initial tensile longitudinal residual stress in the β phase and a compressive stress in the metallic glass matrix [173], which will slightly affect the initial yielding of inclusions in MGMCs, other than the deformation mechanisms. Therefore, thermal residual stress is not introduced to our FEMs in the present work, and will be investigated in a separate work.

A. *Effects of Inclusion Shape and Dendrite Orientation on Lattice Strain Relaxation in Stage III*

The crystalline phases in the FEM capture some but not all the features of the dendritic microstructure. Therefore, it is necessary to examine the effect of geometric parameters on the predictability of the FEM results. Using a single-inclusion model, three kinds of geometric shapes (cubic, spherical, and dendritic morphologies) are employed in the inset of Figure 33. Stress - elastic strain curves of these different models under uniaxial compression are presented. The yield stresses for the inclusion and matrix are 450 and 1,400 MPa, respectively. It could be observed that the slopes of stress - elastic strain curves increase at ~ 450 MPa, and the turnover behavior occurs at ~ 1,400 MPa with an enlarged view in the inset of Figure 33 [186]. It should be noted that the slopes change in Stage II are almost the same for the inner cubic and spherical models, while the

elastic-strain evolution is very different for the dendritic model. This is due to the introduction of high aspect-ratio features in the dendrite, and thus the severe stress concentration. However, the trend of lattice strain evolution is similar for these three different shapes. Near the end of these curves, the plastic zone in the matrix will expand as the applied stress increases, and the load partitioning by the matrix will relax the elastic strain in the inclusion that is responsible for the turnover behavior in the stress versus lattice strain curves for the crystalline inclusions. However, we note that this analysis is based on a continuum plastic model for the matrix, while the actual deformation is by the shear bands. This issue will be further illustrated later by the free volume model.

Another variable is the orientation of the dendritic inclusions with respect to the loading direction, since this trend will directly affect the resulting plastic-zone development. To reduce the simulation effort, 2D uniaxial compression simulations on the MGMCs with 45^{o}- and 90^{o}-oriented dendrite inclusions were performed to investigate the influence of orientations of the dendrite inclusions on the lattice-strain evolution, respectively. It is found that in the MGMCs with a 45^{o}-oriented dendrite inclusion, no relaxation occurs, as indicated by (iii) and (iv) in Figure 34(a) [186]. In contrast, slight relaxation can be observed in the model with a 90^{o}-oriented dendritic inclusion, as shown in Figure 35(a) [186]. As discussed in Refs. [97, 201, 202], complex stress states under loading can be beneficial in improving the plasticity of MGMCs. In the 45^{o}-dendritic model, the stress concentration initiates from four corners of the dendrite inclusion and propagates throughout the entire sample, as shown in the Mises stress contour in Figure 35(b) [186]. In contrast, stress concentration only starts from two horizontal dendrite

vertexes, and the other two perpendicular dendrite vertexes have low stresses, as shown in Figure 35(b). Therefore, this inclusion-geometry study can provide some guidance on the design and preparation of MGMCs.

B. *Effects of Localized Deformation in Metallic Glass on Lattice Strain Evolution*

The studies above successfully predict the lattice strain evolution of crystalline phases in MGMCs. However, the role played by the localized deformation in shear bands in the MG matrix remains unclear. Thus the free-volume-based constitutive model for the MG matrix is employed to investigate the shear band initiation and propagation in the MGMC upon uniaxial compression. The material parameters for the MG matrix are $v_f / \alpha v^* = 0.05$, $E\Omega / 2k_B T = 200$, $\nu = 0.37$, $n_D = 3$, $\alpha = 0.15$, and $v^*/\Omega = 1$, and the normalized applied strain rate is 10^{-3} s^{-1}. In simulations in Figure 36Fig. 9, the inclusions are assumed to be an elastic-perfectly plastic body, with the Young's modulus, Poisson's ratio, and yield stress being 60 GPa, 0.37 and 0.45 GPa, respectively. For comparison, two types of MGMCs with different inclusion shapes, dendritic and circular morphologies, are employed for calculations.

Figure 36(a) [186] describes the lattice strain evolution for both the MG matrix and crystalline inclusion in the circular-inclusion model under compressive loading. Here, the lattice strain is in fact the elastic strain in the loading direction, and the applied stress is the one on the entire specimen. The ultimate lattice strain in the crystalline inclusion is obtained by averaging the values of all inclusion grains. As observed in Figure 36(a), with increasing the applied stress, the lattice strain in both the matrix and inclusion rises linearly at the beginning till a deviation occurs at a stress of ~ 0.8 GPa. Afterwards, the

lattice strain of the MG matrix still increases linearly, while that of inclusions increases at a much lower rate. This trend is due to the load partitioning following the yielding of the crystalline inclusion. When the applied stress reaches ~ 1.7 GPa, the difference of stress/lattice-strain slopes between the MG matrix and inclusion becomes more significant. With the further increase of the applied stress, the lattice strain of the matrix increases significantly, while that of the inclusions begins to decrease, i.e., turnover phenomenon happens. To obtain insights on the mechanism responsible for the stress/lattice-strain slope change in the matrix and inclusion, particularly on the turnover behavior, the free volume contours at stress level (iv) are plotted in Figure 36(b) [186]. Note that SDV1 in Figure 36(b) denotes the first solution-dependent state variable (SDV), which is employed to represent the free volume in the UMAT code [189]. At the stress level (i), although inclusions have already yielded at a nominal yield stress of 0.45 GPa, and the free volume in the matrix starts to localize around the matrix/second phase interface, no stress/lattice-strain slope change occurs. This trend indicates that the load partitioning in the MGMCs does not happen immediately following the yielding of inclusions. When the load is increased to 1.2 or 1.7 GPa, localized deformation begins to form in shear bands, typically as demonstrated in stress levels, (ii) and (iii). At these two stages, more loads will be transferred to the matrix, resulting in much increased lattice strains, while the lattice strain in the crystalline inclusion tends to evolve slowly. In Figure 36(b) [186], the shear bands can be observed to initiate at an angle of ~ 45^{o} from the matrix/inclusion interface and propagate outward. Ultimately, when the localized shear bands propagate and link with each other, the lattice strain relaxation in the

inclusions become more significant, and the turnover behavior will emerge at the stress level (iv).

The study on the dendritic-inclusion embedded MGMCs with the free-volume model is presented in Figure 37(a) and (b) [186], which exhibit similar trends with the circular-inclusion model. The only difference is that the shear bands preferentially initiate from vertexes of the dendritic inclusions in Figure 37(b). This trend demonstrates that the geometry of the inclusions does not exert significant influence on the lattice strain evolution. Note that in these simulations, MGMCs contain roughly 20% (volume percent) of crystalline inclusions. However, in the real specimens, the volume percentage of crystals is ~ 50%. The only difference between the high-volume and low-volume percentage cases is that the chance of forming a dominant shear band by connecting many minor ones is much lower for the high-volume percentage case, due to the enhanced blocking effect of second phases. Clearly, the success of the MGMCs in the ductility enhancement needs to reach the percolation limit, below which the plasticity of MGMC specimens cannot be enhanced significantly.

3.4 Summary

In summary, microscopic deformation mechanisms in the in situ MGMCs have been examined using synchrotron X-ray scattering and FEM under compressive loading in the present work. In a uniaxial compression, the $\sigma - \varepsilon_{hkl}$ curves of the crystalline inclusions could be divided into three stages. In Stage I, both the inclusion and matrix are elastic, before the crystalline inclusions yield at an applied stress of ~ 450 MPa. In Stage II, crystals undergo plastic deformation, while the amorphous matrix remains elastic until

~ 1,480 MPa. In Stage III, beyond 1,480 MPa, both the crystal and matrix yield and are subjected to the plastic deformation until the ultimate failure of specimens. After the β phase yields, the stress concentrations appear in the MG matrix, resulting in the yielding behavior of the matrix at an applied stress slightly lower than its macroscopic yield stress. Different crystal geometries, including cubes/spheres/dendrites, are used to examine the inclusion-shape effects on the elastic strain evolution of the inclusions. Both the elastic-perfect plastic model and the free-volume-based model are used for the MG matrix, which successfully explain the relaxation of elastic strains in the second phase and also the effects of geometric shape and dendrite orientations. Moreover, the present work can provide some guidelines in the design and preparation of MGMCs. For example, the 45^{o}-dendritic inclusions should work better in improving the ductility of MGMCs, compared to the 90^{o}-case, because more stress concentration is introduced into the MGMC specimens upon loading for the 45^{o}-case. The percentage of crystalline inclusions should be above the percolation limit so as to block and deflect the shear-band propagation to form a major shear band, which can lead to the catastrophic failure of MGMC specimens.

CHAPTER IV
THIN-FILM METALLIC GLASS

4.1 Introduction

Thin-film coatings have been used extensively to improve the mechanical behavior of various substrate materials with different thin-film thicknesses [32, 33, 148-152], especially in the field of wear resistance, hardness, and corrosion resistance, without adversely affecting their desirable bulk properties [149]. Coating components are often used in service under cyclic-loading conditions, while experiencing wear and corrosion environments simultaneously, such as cutting saws. Therefore, the fatigue behavior of thin-film coatings is extremely important for the performance of substrate materials. An appropriate example is the widespread use of ceramic coatings, which are deposited on steel substrates to improve their fatigue strength [149]. The beneficial effects on fatigue strength are mainly attributed to the retardation of crack initiation in the substrate materials by the hard ceramic coating [149].

Numerical studies have reported that the fatigue behavior of the film/substrate system is closely dependent on film properties, such as the composition, thickness, hardness, ductility, and structure, as well as film/substrate interfacial adhesion [153, 154]. For instance, many ceramic coatings are susceptible to fatigue-induced fracture and delamination under high stress levels, because of their intrinsically-brittle nature, despite their high hardness and strength. Moreover, with an increase in coating thicknesses, a reduction in the adhesion of the film to the substrate may occur due to increasing residual stresses [203]. A literature review indicates that there are five film properties that could

affect the fatigue-crack-initiation resistance in film/substrate materials [148]: (i) hardness - to prevent surface roughening, (ii) ductility or toughness - to retard crack initiation at the sites where persistent slip bands (PSBs) intersect with the film, (iii) cyclic work hardenability - to reduce slip localization, (iv) residual compressive stresses - to decrease film tensile stresses, and (v) film/substrate adhesion - to prevent film delamination, for which good film/substrate adhesion is the most important factor responsible for fatigue-resistance enhancement [32, 33, 156]. Therefore, good balance between beneficial mechanical properties of coatings and film/substrate adhesion is the prerequisite for the excellent potential coating materials to enhance the fatigue behavior of substrates.

Based on the above analysis and reported results, the TFMG can be a good candidate as excellent coating materials, because of their unique properties, as shown in Figure 26 [155]. It should be noted that TFMGs have much higher yield strengths than ceramic and metallic (crystalline) coatings, while metallic coatings and TFMGs have larger ductility, usually indicating better adhesion with the substrate than ceramic coatings. Therefore, TFMGs should have better balance of strength and ductility than crystalline metallic and ceramic coatings, indicating that MGs can be better coating materials than most ceramic and metallic coatings.

Currently thin-film coatings have been used extensively to improve the mechanical behavior of various substrate materials [32, 33, 148-152], with different thin-film thicknesses [from nanometers (nm) to micrometers (μm)], especially in the field of wear resistance, hardness, and corrosion resistance, without adversely affecting their desirable bulk properties [149]. Coating components are often used in service under cyclic-loading conditions, while experiencing wear and corrosion environments

simultaneously, such as on cutting saws. Therefore, the fatigue behavior of thin-film coatings is extremely important for the performance of substrate materials. An appropriate example is the widespread use of ceramic coatings, which are deposited on steel substrates to improve their fatigue strength [149]. The beneficial effects in fatigue strength are mainly attributed to the retardation of crack initiation in the substrate materials by the hard ceramic coating [149].

Numerical studies have reported that the fatigue behavior of the film/substrate system is closely dependent on film properties, such as composition, thickness, hardness, ductility, and structure, as well as film/substrate interfacial adhesion [153, 154]. For instance, many ceramic coatings are susceptible to fatigue-induced fracture and delamination under high stress levels, because of their intrinsically-brittle nature, despite their high hardness and strength. Moreover, with an increase in coating thicknesses, a reduction in the adhesion of the film to the substrate may occur due to increasing residual stresses [203]. A literature review indicates that there are five film properties that could affect the fatigue-crack-initiation resistance in film/substrate materials [148]: (i) hardness - to prevent surface roughening, (ii) ductility or toughness - to retard crack initiation at the sites where persistent slip bands (PSBs) intersect with the film, (iii) cyclic work hardenability - to reduce slip localization, (iv) residual compressive stresses - to decrease film tensile stresses, and (v) film/substrate adhesion - to prevent film delamination, for which good film/substrate adhesion is the most important factor responsible for fatigue-resistance enhancement [32, 33, 156]. Therefore, good balance between beneficial mechanical properties of coatings and film/substrate adhesion is the prerequisite for excellent potential coating materials to enhance the fatigue behavior of substrates.

Based on the above analysis and our preliminary results, the TFMG can be a good candidate as excellent coating materials, because of their unique properties, as shown in Figure 26 [185, 204-218]. It should be noted that TFMGs have much higher yield strengths than ceramic and metallic (crystalline) coatings, while metallic coatings and TFMGs have larger ductility, usually indicating better adhesion with the substrate than ceramic coatings. Therefore, TFMGs should have better balance of strength and ductility than crystalline metallic and ceramic coatings, indicating that MGs can be better coating materials than most ceramic and metallic coatings. Note that two same symbols in Figure 26 represent the upper and bottom limits of yield strength and ductility of the corresponding material. In practice, these unique mechanical properties of TFMGs have made them very popular to enhance the plasticity, strength, and fatigue life of different substrates, including steels [32, 151, 156, 219], Ni-based alloys [32, 156, 157], and BMGs [33] in the past several decades. In this paper, the fatigue behavior of TFMG coatings deposited on structural materials will be reviewed and discussed.

4.2 Experimental and Numerical Approaches

4.2.1 Coating preparation and characterization

Two kinds of fatigue tests, including four-point-bending and tension-tension fatigue, will be conducted in the present work. The substrate materials used in the present paper are the commercial-grade 316L stainless steel with 20% cold rolling [220], HAYNES C-2000® Ni-based superalloy [221], Zr-based alloy (Zr-Hf) [222], Ti-based alloy (Ti-6Al-4V) [223], and Al-based alloy (7075-T6) [224]. Substrate compositions are

listed in Table 3. The specimen geometry for the four-point-bending fatigue experiments, with a sample size of $3 \times 3 \times 25$ mm^3, is shown in Figure 38(a) [155].

Four-point-bending fatigue-substrate specimens were prepared in two ways: (1) the 316L stainless-steel specimens were polished by an 800-grit sand paper and then electropolished to ensure a smooth surface; and (2) the Ni-based, Zr-based, Ti-based, and Al-based alloy specimens were mechanically polished by a 1,200-grit sand paper, followed by 1-μm diamond paste polish. The specimens for the tension-tension fatigue test, a notched 316L steel bar, were mechanically polished by a 1,200-grit SiC paper.

The sputtering process establishes a series of collision events between ions and target materials, resulting in the target-atom ejection onto the surface of substrates with the desired compositions. In the present work, magnetron sputtering is employed for film deposition [225]. The electron-residence time in the plasma is prolonged by the magnetic field lives, thus enhancing the Ar-ionization efficiency and increasing the deposition rate. Multicomponent TFMGs, with compositions of $Zr_{47}Cu_{31}Al_{13}Ni_9$, $Cu_{51}Zr_{24}Hf_{18}Ti_7$, and $Fe_{65}Ti_{13}Co_8Ni_7B_6Nb_1$ (atomic percent, at.%), were deposited using commercial radio frequency (RF) magnetron sputtering systems [226, 227], with base and working pressures of 10^{-7} and 10^{-3} Torr, respectively. The substrates were rotated during deposition in order to ensure uniform film thicknesses.

In order to study film-thickness effects on the fatigue behavior of substrate materials, TFMGs with two different thicknesses, 200 nm and 1 μm, are deposited on the above mentioned substrates. Thin films with different compositions, including TiN, pure copper films, Zr-based, Cu-based, and Fe-based TFMGs with thicknesses of 200 nm, deposited on the 316L stainless steel, are employed to study film-composition effects on

the fatigue behavior of substrate materials. Together with the above mentioned TFMG, the fatigue behavior of another kind of TFMG, the "annealed" TFMG [225, 228, 229], with a more homogeneous amorphous film structure, is also studied. For this annealed TFMGs, additional steps are needed, as described below, in addition to the above mentioned monolithic TFMG preparation procedure [225]. Monolithic TFMGs, with the composition of $Zr_{47}Cu_{31}Al_{13}Ni_9$ (at.%), are annealed in an Ar atmosphere at a heating rate of 40 K/min. with a holding time of 60 s at temperatures ranging from 550 to 950 K. Annealing is performed in the mTorr range after several Ar purges [225].

BMGs ($Zr_{50}Cu_{30}Al_{10}Ni_{10}$, at.%) were machined into rectangular beam with a sample dimension of 3 mm × 3 mm × 25 mm from as-cast ingot fabricated by arc melting in an argon atmosphere. Prior to thin film deposition, the four faces of BMG substrates were polished to be a mirror-like surface by using emery papers with grit size up to 4000. A 260 nm-thick TFMG was deposited on the BMG substrate with ZrAlNiCu alloy target by using radio frequency magnetron sputtering system with a base pressure of $< 1 \times 10^{-6}$ Torr. Upon sputtering deposition, argon was introduced as sputtering gas with a working pressure of 3 mTorr. The substrate bias of -50 V was applied during deposition. The working distance was 100 mm.

The crystallographic structures were characterized by X-ray diffractometer (XRD, D8 Discover) with Cu Kα radiation at 40 kV and 200 mA. A low glancing angle was used for thin film. The composition of TFMG was determined by energy dispersive spectrometer (EDS) and the fracture surfaces of specimens were examined by secondary electron microscope (SEM) in dual-beam focused ion beam system. A transmission electron microscopy (TEM) was use to examine the nano-structure and to obtain the

selected-area diffraction pattern (SADP) to check the crystallinity in the specimen. The operated voltage for high resolution image and SADP was 200 kV. To acquire the mechanical properties of coating and substrate, a nanoindenter (HysitronTM TI 950 TriboIndenter) with a Berkovich 142.3 ° diamond indenter was employed with a maximum loading of 1200 μN.

4.2.2 Fatigue tests

A computer-controlled servo-hydraulic testing machine is employed to conduct the four-point-bending fatigue experiments, which were performed under a load-control mode, using a sinusoidal waveform frequency of 10 Hz, with an R ratio ($R = \sigma_{min.} / \sigma_{max.}$) of 0.1, where $\sigma_{min.}$ and $\sigma_{max.}$ are the minimum and maximum applied stresses, respectively. Before the fatigue tests, the height (h) and width (b) of the specimens were measured and used to calculate the applied-stress (σ) range at the tensile surface using Eq. (23), where S_1 = 10 mm and S_2 = 20 mm, with the specimen geometry shown in Figure 38(a).

$$\sigma = \frac{3P(S_2 - S_1)}{2bh^2} \tag{23}$$

Upon failure or 10^7 cycles, the fractographs of samples were analyzed using SEM and TEM, in order to have in-depth understanding of the tension-tension fatigue mechanism.

4.2.3 Numerical Method with FEM (Rudnicki-Rice instability theory)

The mechanism responsible for improving mechanical behavior by TFMG, especially the ductility and fatigue behavior, usually results from the multiplication of shear bands in the amorphous phase, thus affecting shear-band propagation to the interface between the coating and substrate, which has already been observed by TEM in

Refs. [32, 33, 219]. However, the shear-band nucleation/initiation and propagation behavior cannot be monitored and characterized, due to the extreme difficulty of the in-situ TEM observation during fatigue loading. In contrast, finite-element modeling (FEM), using the Rudnicki-Rice (R-R) instability theory [230, 231] and free-volume model [189, 190], provides a feasible method to study shear-band initiation and propagation in the film/substrate materials under deformation,

Strain localization is an instability phenomenon, from a continuum-mechanics point of view, and can be described by a bifurcation theory in which the shear band results from the bifurcation of a homogeneous elastic-plastic flow. The shear-band angle in the principal stress space is given by [230, 231]:

$$\theta_0 = \tan^{-1}\sqrt{\frac{\xi - N_{\min}}{N_{\max} - \xi}} \tag{24}$$

where ξ is a function given by $\frac{1}{3}(1+\upsilon)(\mu+\beta) - N(1-\upsilon)$, $N_{\max} = \frac{\sigma_I^{'}}{\bar{\tau}}$, $N = \frac{\sigma_{II}^{'}}{\bar{\tau}}$, $N_{\min} = \frac{\sigma_{III}^{'}}{\bar{\tau}}$, and $\bar{\tau} = \frac{\sigma_{mises}}{\sqrt{3}}$. $\sigma_I^{'}$, $\sigma_{II}^{'}$, and $\sigma_{III}^{'}$ are the principal deviatoric stresses. υ is the Poisson's ratio, μ is the coefficient of internal friction, and β is the dilatancy factor, $\bar{\tau}$ is the effective shear stress, and σ_{mises} is the Mises stress. Accordingly, the shear-band plane will make an angle of ± θ° with the first principal-stress direction, while the shear-band plane is parallel to the second principal-stress direction.

4.3 Fatigue behavior of TFMGs on BMG substrates

4.3.1 Summary on the reported work on the fatigue behavior of TFMGs

The fatigue lifetimes and endurance limits of the above film substrate material systems, together with base Zr-based and Cu-based BMG alloys, are plotted in Figure 39(a) [151, 152, 156, 157, 219] , in which five regions (A, B, C, D, and E) are observed in the boxed areas. For the four-point-bending fatigue data (A, B, and C), the results can be divided into high (C, larger than 700 MPa), medium (B, 300 - 700 MPa), and low (A, smaller than 300 MPa) fatigue-endurance limit regions in the TFMG-substrate material systems. Region D represents tension-tension fatigue data of the TFMG-substrate material systems, while the monolithic BMG [$Zr_{55}Cu_{30}Ni_5Al_{10}$ and $(Cu_{60}Zr_{30}Ti_{10})_{99}Sn_1$, at.%] four-point-bending fatigue data is shown in region E. For the coated 316L stainless steel (in region C), neither fatigue lifetime and endurance limit is improved by the Fe-based TFMG, TiN, and pure-Cu films adhesion, due to the intrinsic brittle nature of films and/or poor film/substrate. For the good adhesion cases in region C, such as Zr- and Cu-based TFMGs on steels, the lifetime and fatigue-endurance limit can only be improved more or less, which may be caused by the high fatigue-endurance limit of the substrate materials. Note that the 316L stainless-steel substrate is cold rolled, which may be the reason for its high fatigue-endurance limit [220].

In contrast, for the medium fatigue-endurance limit materials in regions B, such as the HAYNES C-2000® Ni-based alloys, the fatigue lifetime and endurance limit are enhanced more significantly by the Zr-based ($Zr_{47}Cu_{31}Al_{13}Ni_9$, at.%) TFMGs, compared to the steel case. For example, the fatigue-endurance limit is increased from 400 MPa to around 625 MPa. In the tension-tension fatigue data (region D), both the fatigue lifetime

and endurance limit of the 316L stainless steel are not significantly affected by Zr- and Cu-based TFMGs. The poor performance of film/substrate system upon tension-tension fatigue loading is caused by the poor film adhesion with the substrate, resulting from stress concentration in the notched dog-bone tension-tension specimens.

Figure 39(b) [155] shows the cyclic-stress range/ultimate tensile strength (UTS) vs. cycles to failure (S/UTS-N) of TFMG-substrate materials and BMGs, with the UTS of substrates listed in Table 2 [155]. Figure 39(b) can be also separated into five regions based on the substrate materials, corresponding to Figure 39(a), represented by A', B', C', D', and E'. For example, the Al-based alloy is in region A in Figure 39(a) and in region A', the low S/UTS range, in Figure 39(b). The Zr-based, Ti-based, and Ni-based alloys are in the medium S/UTS range (region B'), while the 316L stainless steel is in high S/UTS range (region C'). The regions, D' and E', represent the S/UTS ranges of the tension-tension region and monolithic BMG region, respectively. Note that the S-N and S/UTS-N plots roughly correlate with each other for most film/substrate materials, expect for the BMG region E', which is attributed to the high UTS of BMGs.

In order to better demonstrate the improvement of fatigue behavior of different film/substrate systems, the plots of improvement of fatigue-endurance limit vs. UTS, improvement of fatigue-endurance limit/UTS vs. UTS, improvement of fatigue-endurance limit vs. fatigue-endurance limit, and improvement of fatigue-endurance limit/UTS vs. fatigue-endurance limit for the bare substrates and film/substrate systems are displayed in Figure 40(a), (b) and Figure 41(a) and (b), respectively [155]. Figure 41(c) shows the relationship between the fatigue-endurance limit and UTS of the substrate materials, presenting a approximated linear correlation between them, which

means the substrate material with a higher UTS generally has a larger fatigue-endurance limit, as found in our previous study [232]. Improvement is defined as the difference in the fatigue-endurance limit and fatigue-endurance limit/UTS between the bare substrate and film/substrate specimens. It is shown that the improvements of the fatigue-endurance limit and the fatigue-endurance limit/UTS of the substrate are the most significant for medium-UTS (fatigue-endurance limit) substrate materials (HAYNES C-2000® Ni-based alloys); see the red dashed curves in Figure 40(a), (b) and Figure 41(a) and (b), TFMGs perform the best on the fatigue-behavior improvement of Ni-based alloys. Upon loading, the plastic deformation of TFMGs can be accommodated by the medium strength (fatigue-endurance limit) crystalline substrates, resulting in good film/substrate adhesion, since the monolithic BMGs are generally in the medium fatigue-endurance region. However, for the low [such as, Al-based alloy (7075-T6)] and high [such as, Ti-based alloy (Ti-6Al-4V)] strength (fatigue-endurance limit) materials, the fatigue behavior (improvement of fatigue-endurance limit and fatigue-endurance limit/UTS) of the film/substrate systems is enhanced moderately, but not as evidently as medium fatigue-endurance limit materials.

For the low-strength (fatigue-endurance limit) substrate, the fatigue-endurance limit can be much lower than that of the TFMG. Therefore, incompatible deformation between the TFMG and low-strength (fatigue-endurance limit) substrate occurs upon loading, which will easily lead to the film delamination and poor fatigue performance of the substrate materials. The incompatible deformation also happens for the high-strength (fatigue-endurance limit) substrate upon loading, since the fatigue-endurance limit for the high-strength (fatigue-endurance limit) substrate can be higher than that of the TFMG. In

contrast, for the medium-strength (fatigue-endurance limit) substrate, the fatigue-endurance limit can be generally comparable to that of the TFMG, which will not lead to the incompatible deformation between the TFMG and substrate upon loading, therefore increasing the fatigue performance of the TFMG/substrate systems.

Moreover, the film properties can affect the film/substrate adhesion in the film/substrate system, which will result in the dramatic difference in the fatigue behavior of the film/substrate system, as mentioned in Section 4.3. For example, TFMGs having good adhesion with crystalline substrates, such as Zr-based and Cu-based TFMGs, can increase the fatigue behavior of substrate materials, while poor film adhesion with the substrate, such as the Fe-based TFMG, will not significantly increase the fatigue behavior of substrate materials.

Therefore, the overall S-N and S/UTS-N curves, together with (1) the improved fatigue-endurance limit vs. UTS, (2) improved fatigue-endurance limit/UTS vs. UTS, (3) improvement of fatigue-endurance limit vs. fatigue-endurance limit, (4) improvement of fatigue-endurance limit/UTS vs. fatigue-endurance limit, and (5) UTS vs. fatigue-endurance limit results in Figure 39, Figure 40, and Figure 41, provide clues for the future study of the fatigue behavior of TFMG/substrate material systems.

4.3.2 Fatigue behavior of TFMG with BMG substrate

The composition of TFMG was measured to be $Zr_{60.2}Cu_{24.4}Al_{10.6}Ni_{4.8}$ (in atomic percent, at.%) by EDS. Figure 42(a) shows the X-ray diffraction patterns for BMG sample and TFMG, which show only a broad diffraction hump with 2θ in a range of 30-45 ° in both specimen corresponding to an amorphous structure, and no peaks of any crystalline phases can be detected.

Figure 42(b) shows the stress-life (S-N) curve of the BMG substrate coated with a 200 nm-thick Zr-based thin-film metallic glass. It can be observed that the 200 nm-thick TFMG could improve the fatigue life of the BMG substrate. Based on the applied maximum stress, the fatigue endurance limits of the BMG substrate and the substrate with 200 nm-thick TFMG are 300 MPa and 400 MPa, respectively. It can be noticed that at both high and low stress levels, the improvement of the fatigue lives is very pronounced by the Zr-based TFMGs, which is slightly different with the reported works on the case of conventional metallic materials, such as, steel and Ni-based alloys [156, 157]. For the conventional metallic alloys, the fatigue behavior of TFMG-coated specimens is usually improved more pronounce in the low strass levels, compare with their performance at high stress level. What are the deformation mechanisms for the improved fatigue behavior of TFMG-BMG? As illustrated in the previous work [32, 33, 155-157], it will be investigated using the SEM and TEM to characterize the fractography of the fatigue-fractured specimens at different stress levels in this section.

Figure 43 shows the SEM fractographs of TFMG-BMG with a 200 nm-thick Zr-based metallic-glass film after fatigue-fractured at σ_{max} = 450 MPa. As marked in Figure 43(a), three regions can be observed on the fracture surface, including fatigue-crack-initiation (Stage I), crack-propagation (Stage II), and fast failure (Stage III) regions could be observed. Fatigue-crack initiates from the corner of the tensile surface exhibiting a striation-type structure (close to the TFMG, marked with red circle), then propagates inside with crack-growth direction indicated by the red arrow on the micrograph. There is a distinct boundary between the fatigue-crack-growth region and the fast-fracture region [Figure 43(b)], which shows very different microstructures in different regions. The final

fracture (Stage III) surface shows a porous structure surface, which is usually a vein-like structure in the reported work of BMG fatigue deformation [233-235]. A tilted-angle image [Figure 43(c)] shows the interface region of the fatigue fractured specimens after loading at the maximum stress of 450 MPa, which clearly indicates that, after the severe plastic deformation and final fatigue fracture, only slightly film delamination appears at the area close to fracture surface, while the TFMG remained well adhered with the substrate in the other region. Moreover, no observable cracks are found on the TFMG, which is a very good indication of the good adhesion between the TFMG and BMG substrate. This is due to the excellent film ductility can accommodate the fatigue deformation of substrates during the cyclic loading.

Figure 45 shows the SEM fractographs of TFMG-BMG with a 200 nm-thick Zr-based metallic-glass thin film after fatigue-fractured at σ_{max} = 500 MPa. As marked in Figure 45(a), three regions can be observed on the fracture surface, including fatigue-crack-initiation (Stage I), crack-propagation (Stage II), and fast failure (Stage III) regions could be observed, which is similar to the fatigue-fractured TFMG specimen at σ_{max} = 450 MPa. Fatigue-crack initiates from the area close to the tensile surface, which exhibits a striation-type structure, as shown in Figure 45(b). Then the crack propagates toward inside of the specimen, with crack-growth direction marked by the red arrow in Figure 45(a). Distinct boundary can be observed between the fatigue-crack-growth region (Stage II) and the fast-fracture region (Stage III), as displayed in Figure 45(c). The final fracture (Stage III) surface shows a porous structure surface, which is confirmed to be a vein-like structure in Figure 45(e). However, in fatigue crack-propagation region (Stage II), there is no vein-like structure observed. This trend demonstrates that the melting phenomenon

of BMGs did not occur at the tip of the fatigue crack during the crack-propagation stage. In fact, it means that the released elastic energy due to crack propagation is too low to melt the metallic glass locally. This result is consistent with observations reported in references [234, 236-238]. However, most of the elastic and plastic energy was released to melt the metallic glass at the moment of the final fracture [234]. A tilted-angle image [Figure 45 (d)] shows the interface region of the fatigue fractured specimens after loading at the maximum stress of 500 MPa, which clearly indicates that, after the severe plastic deformation and final fatigue fracture, only slightly film delamination appears at the area close to fracture surface, while the TFMG remained well adhered with the substrate in the other region. This is a very good indication of the good adhesion between the TFMG and BMG substrate, which is due to that the excellent film ductility can accommodate the fatigue deformation of substrates during the cyclic loading.

Fatigue-damage mechanisms of crystalline materials have been well studied and understood, and many theories are available. In general, slip bands (SBs), twinning, deformation bands (DBs), and grain boundaries (GBs) are the preferential sites for the nucleation of fatigue cracks in single-phase materials. However, since BMGs are non-crystalline materials, their fatigue crack-initiation and growth mechanisms could be different from those of the crystalline alloys. The basic fatigue-damage mechanism of BMGs is still unclear. However, the deformation mechanism of metallic glasses is usually attributed to the presence of shear bands and plastic flows. Because the plastic flow is confined to narrow regions (shear bands) of the BMGs, the presence of a shear band in a metallic glass specimen reduces its strength by providing a site for further plastic flows [239, 240].

4.3.3 Deformation mechanism of TFMG-BMG with TEM

Figure 46 shows micro-cracks and shear-off steps on the tensile surface near the fracture surface of a coated $Zr_{50}Cu_{30}Al_{l0}Ni_{10}$ specimen tested at σ_{max} = 500 MPa (The TEM graphs in the present thesis are obtained with the help of Mr. Chia-Chi Yu in Dr. Jinn P. Chu's research group). In both Figure 46(a) and (b), the presence of shear-off steps and micro-cracks was observed. It can be noticed that the micro-cracks generally initiate from shear-off steps, and the shear-off steps are almost parallel to each other. Even though the multiple shear-off steps and micro-cracks formed, the TFMG coating is still well adhere to the substrate without peeling-off. Good adhesion between substrate and coating has been demonstrated as an important factor affecting the fatigue crack-initiation [155].

In general, shear band or crack usually initiates from the casting defects and porosity in a BMG specimen introduced during alloy casting and leads to a preliminary failure due to the stress concentration in these sites [241]. These defects could have a significant effect on the mechanical properties of a BMG specimen, especially, on the fatigue properties [235, 242]. A Weibull size effect appears and shear bands embryo heterogeneously in a millimetre-size MG specimen due to a higher population of casting flaws in the specimen [243]. When the scale of MG specimen down to submicron- or nano-scale, the deformation of a thin MG specimen would require the homogeneous nucleation of shear bands which would lead to an increase of yield strength of specimen [244].

Recently, Wang, et al. [245] discovered that the nucleation length for shear banding in metallic glass can reach as high as 500 nm in the case of constrained

deformation, such as indentation. Therefore, a 260 nm-thickness TFMG is expected to deform homogeneously without embryonic shear banding in this study. Nanoindentation tests were carried out on the BMG sample and TFMG on Si wafer at a maximum applied loading of 1,200 μN. In order to avoid substrate effect, the film was prepared with a thickness of 500 nm. Nanoindentation curves for BMG substrate and TFMG were obtained. The pop-in or serration events can be observed in the loading curve of BMG, associated with coalescence of local shear transformation zones (STZs) and lead to an individual shear banding underneath the indent area [244, 246, 247]. However, no pop-in event can be observed in the TFMG curve which validate the result that the shear-band nucleation lengths are as high as 500 nm reported by Wang et al. [245].

TEM EDS line-scan was used to analyse the composition at the interface between the Zr-based TFMG and BMG substrate, as shown in Figure 47. An apparent dark line presents in the interface between the film and substrate while no significant contrast can be observed at the shear-band offset region in Figure 47(c). Based on the line-scan results in Figure 47(e), obvious drops in X-ray intensity for all elements are observed at the corresponding position for the interface between the film and substrate. This suggests the less dense region at interface might have resulted from undesirable preferential etching during FIB TEM sample preparation. However, no apparent intensity difference is shown at the interface of shear-band offset region, as presented in Figure 47(d). It is assumed that the energy released during shear-band offset formation which led to a localized temperature rising at offset region. As a result, the diffusion and fusing occurred at the offset region between metallic glass film and substrate. It has been reported by Chu et al. [33] that the TFMG coating can cover the surface weak points and decreased shear-band

initiating point at the surface of coated samples as well as absorb the deformation energy when the coated BMG substrate undergoes plastic deformation.

4.4 Finite-element simulations of the mechanical behavior of TFMGs

As mentioned in Section 2, under deformation, the plastic flow in BMGs is accommodated by shear bands. Thus, catastrophic failure happens due to the unconstrained propagation of individual shear bands. Hence, the most efficient way to improve ductility is to geometrically constrain these shear bands, so that the plastic strain in each shear band can be minimized, therefore preventing crack initiation. The application of surface coatings is a typical approach to constrain the shear-band propagation and, thus promote the proliferation of shear bands. For example, Li et al. [248] studied the effect of nanocrystalline Ni-15%Fe (weight percent, wt.%) coatings on Zr-based BMGs and ascribed the ductility enhancement to the increased shear-band density. They proposed that the multiplication of shear bands was due to the resistance of the nanocrystalline coating to shear-band propagation at the interface. However, the detailed mechanism still needs to be elucidated, and this process can be well understood through computational studies investigate coating effects, using both the Rudnicki-Rice instability theory [230, 231] and the free-volume model [189, 190] as described below.

4.4.1 Rudnicki-Rice instability-theory simulations

To predict the shear-band initiation and propagation under deformation, in coating/substrate systems with a film/substrate thickness ratio of 1/20, compared with the bare substrate case, a three-dimensional (3-D) half-symmetric ABAQUS model under Rockwell indentation was developed, as shown in Figure 58(a) [155]. In this model, both

the MG substrate and film are treated as a pure elastic body, which means that the deformation behavior of the substrate and coating is dominated by their Young's moduli (E) and Poisson's ratios (υ), with E = 88.6 (substrate) and 122 (film) GPa, and υ = 0.3 (substrate) and 0.34 (film), respectively. The Rudnicki-Rice instability theory is employed to predict the directions of shear bands for both the monolithic [Figure 58(b)] [155] and coated BMGs [Figure 58(c)] [155], with $\mu + \beta = 0$ in the MG substrate, where $\mu + \beta = 0$ indicates that the materials deformation is pressure insensitive and associative. The detailed explanation on the $\mu + \beta$ from the mechanics point of view can be found in the work [231]. The prediction, from the instability theory, gives typical radial shear-band patterns under indentation for both the bare substrate and film/substrate cases, which is consistent with many reported experimental results [191, 231, 249]. In Figure 58(b), the blue solid curves indicate the predicted shear-band directions, while the red dashed curves are along principal shear stress directions. Since there are no shear-band constraint conditions on the surface of the monolithic BMG specimen, only major shear bands appear and propagate in the MG substrate. However, in the coating/substrate material system, more shear bands appear, most of which are less than the major shear bands in the bare-substrate case, as shown in Figure 58(c). It can be observed that a lot of short solid black and dashed green curves, which are the corresponding shear-band directions and principal shear-stress directions, respectively, occur at the coating/substrate interface, together with some larger shear bands (blue solid curves). This phenomenon suggests that the local strain of the BMG produced in the deformation process can be dispersed by more shear bands, which reduce the shear strain in each shear band. Therefore, the plasticity of BMG substrate is increased by a surface coating.

Moreover, in the TFMG-substrate material systems, shear bands are “reflected”, resulting in the occurrence of more short and minor shear bands [solid curves, Figure 58(c)], when major shear bands propagate and arrive at the film/substrate interface during deformation, as shown in Figure 58(c). It should be noted that in our simulations, shear bands start from the substrate material, while shear bands can be initiated at the interface in the real case. The term “reflection” means the shear-band directions change, since two families (before and after reflection) of shear bands may be initiated simultaneously. This trend causes the formation of multiple shear bands at the interface, so that each shear band will not endure a large amount of shear strains. Thus, enhanced ductility can be achieved in the coated MG during experiments. Similar simulation results concerning the coating effects on the shear-band propagation were reported by Chu et al. [33], which reveals that the deformation bands are shorter and less developed in the coated samples, compared with the uncoated BMG substrate. Ultimately, each shear band carries less shear stain for the coated samples, and, therefore, the ductility is increased. For future studies, the simulation on cases of crystalline substrates with MG films will be conducted, in order to have a direct comparison with the experimental data in the present work.

4.4.2 Free-volume-model simulations

As reported in the previous work [32, 33, 155], the fatigue behavior of the film/substrate material system is significantly dependent on the adhesion between the film and substrate. However, the effects of the adhesion between the film and substrate are difficult to simulate with the Rudnicki-Rice instability theory. Here, a free-volume model will be employed to investigate the effects of film/substrate adhesion and film thickness on the fatigue behavior of coated specimens. Note that we are interested in the

effects of geometry constraint of films on the substrate. The film/substrate system with the crystal coating on the MG substrate is studied in the present work, which may not be exactly the same with the experimental case of the present work.

A two-dimensional (2D) ABAQUS model consisting of four-node plane-strain elements, with an element type of CPE4, is constructed under indentation loading, with an MG substrate and a Ti-based alloy coating. To explore the effects of coating thickness and adhesion on enhanced plasticity, films with varied configurations and constitutive laws are employed. A rigid Rockwell indenter was applied to indent the specimen, and the sample bottom is completely immobile. The contact between the indenter and sample was frictionless, while the substrate/coating interaction varies for different simulation purposes, as explained below. For all substrate materials, the constitutive parameters are $v_f / \alpha v^* = 0.05$, $E\Omega / 2k_BT = 240$, $\upsilon = 0.33$, $n_D = 3$, $\alpha = 0.15$, and $v^* / \Omega = 1$. Here, f is the frequency of the atomic vibration, α is a geometric factor of order 1, v* is the hard-sphere atomic volume, v_f is the average free volume per atom, ΔG^m is the activation energy, Ω is the atomic volume, k_B is the Boltzmann constant, and T is the absolute temperature. The normalized loading rate is $\dot{\gamma} = \frac{\dot{h}}{Rf}\exp(\frac{\Delta G^m}{k_BT}) = 2.3 \times 10^{-6}\ s^{-1}$. Different constitutive relations are assigned to the coatings and substrates, as described below.

To investigate the effects of coating adhesion on the ductility and fatigue enhancement of BMGs, different indentation contours were simulated in Figure 52 [155]. The coating material used in the present work is Ti, which is treated as a purely elastic body in the ABAQUS model, with a Young's modulus of E = 122 GPa and a Poisson ratio of $\upsilon = 0.34$. In Figure 52(a), it is demonstrated that the indentation of the bare

BMG substrate results in several major pairs of intersecting shear bands. By contrast, the indentation of Ti-coated MG specimen to the same displacement induces the formation of multiple shear bands, for both infinite-adhesion and zero-adhesion cases, as displayed in Figure 52(b) and (c), respectively. This shear-band multiplication phenomenon in the coating case is attributed to two mechanisms: (1) shear-band reflection occurs at the film/BMG interface, and (2) abundant minor shear-band branches appear inside the coated specimens. Both mechanisms are triggered by the geometrical constraint of coatings and responsible for the enhanced plasticity in MGs. This result agrees well with the previous predictions by the Rudnick-Rice instability theory on shear-band multiplication in coating/substrate materials [230, 231].

Experimental studies [33] reveal that film/substrate adhesion plays a crucial role in enhancing the ductility of BMGs. To examine this effect, two extreme cases are simulated in the present work with the ABAQUS model: (1) indentation of a Ti-coated MG substrate with perfect adhesion [Figure 52(b)] and (2) the same sample with zero adhesion [Figure 52(c)], which is realized by defining a frictionless film/substrate contact between the film and substrate. Consistent with the experimental observations, poor film/substrate adhesion tends to bring about less shear-band reflection and branching, which is attributed to film delamination occurring easily in the poor adhesion case. As a result, only relatively limited enhanced plasticity is obtained in the poorly-bonded coating material, thus leading to poor fatigue improvement. For the perfect film-adhesion condition, the fatigue-crack initiation stage is significantly elongated, thus prolonging the overall fatigue life of this coating material. This trend is consistent with the reported fatigue experimental results that good adhesion usually leads to the longer fatigue life of

coated specimens [155]. However, it should be noted that geometrical constraints by coatings will lose their effect on the ductility and fatigue improvement of substrate materials once the fatigue crack starts to propagate.

The experimental results show that fatigue behavior is strongly dependent on film thickness. Therefore, two different cases, with a film/substrate thickness ratio of 20 (thin-film) [Figure 53(a)] [155] and 5 (thick-film) [Figure 53(b)] [155] in the perfect film adhesion case, are simulated in the present work. The results reveal that many more shear-band branches appear in the BMG substrate, but only several major shear bands for the thin-film case. Moreover, for the thin-film case, the major shear bands don't arrive at the film/substrate interface. However, the major shear bands can reach the interface in the thick-film case, which would lead to film delamination. These simulation results are consistent with most of the current experimental data and shows why more fatigue work on the TFMG-coated specimens are conducted with the film thickness of 200 nm, rather than 1 μm or larger, although some exceptional cases exist [33, 152, 159].

Based on the analysis above, a summary of the fatigue-crack initiation and propagation mechanisms in the TFMG-substrate material systems is displayed in Figure 59. It can be observed that fatigue-crack initiation in the TFMG-substrate system results from dislocation pileup in crystalline substrates under cyclic loading, with the fatigue crack-initiation factors: (i) film/substrate interface adhesion; (ii) surface roughness; (iii) coating properties; and (iv) coating thickness. After the fatigue crack initiates in the TFMG/substrate systems, some minor shear bands will be formed in the TFMG. Thereafter, the fatigue crack-propagation process will not be affected significantly by the TFMG, which will result in rapid failure of the TFMG/substrate system. Beneficial-effect

factors on fatigue behavior of the TFMG/substrate systems are: (i) medium-strength substrate materials; (ii) good TFMG/substrate adhesion; (iii) TFMGs with good ductility; and (iv) proper film thickness (~ 200 nm in the present work).

4.5 Summary

Thin-film metallic glasses provide a possible solution to utilize their unique properties to increase the plasticity and fatigue resistance of substrates, without weakening substrate strength, even though BMGs possess a macroscopic brittle nature. In this paper, the fatigue behavior and underlying micro-mechanisms of TFMGs were studied with both experimental and FEM simulation methods. Zr-based and Cu-based TFMGs, as well as annealed Zr-based TFMGs, were employed to improve the four-point-bending fatigue resistance of 316L stainless-steel, Ni-, Zr-, Al-, and Ti-based alloy substrates, while TiN, pure Cu, and Fe-based TFMGs did not extend the four-point-bending fatigue life of steel substrates. The fatigue results show that the TFMGs have the best effects on the fatigue behavior of medium-strength substrates, with less significant effects on low and high strength materials. The enhancement of fatigue life is mainly attributed to the good ductility and strength of the films, leading to the multiplication of shear bands in TFMGs, and, thus prolonging the fatigue-crack-initiation state of film/substrate materials. Consequently, it requires more fatigue cycles for the fatigue-crack initiation, resulting in the enhanced fatigue life in the presence of TFMGs.

In contrast, failure of the fatigue-life enhancement by thin films is attributed to poor adhesion between the film and substrate, yielding film delamination. The thin film then has little influence on the fatigue-life extension of the substrate, once a fatigue crack

starts to propagate. The tension-tension fatigue life of the Zr- and Cu-based TFMG-coated 316L steel substrate is not improved by the thin-film coating because of film delamination and peel-off.

The mechanisms of the ductility and fatigue-resistance enhancement in film/substrate systems have been studied using the ABAQUS simulation model. Enhanced ductility and plasticity in MGs is attributed to shear-band multiplication in the coating material due to two mechanisms: (1) shear-band reflection occurs at the film/BMG interface and (2) abundant minor shear-band branches appear inside the MG substrate of coated specimens. These two mechanisms are triggered by the geometric constraint of the coating. The simulation results show that film thickness, together with adhesion between the film and substrate, have significant effects on the shear-band multiplication of BMGs, hence affecting the ductility and fatigue behavior of the film/substrate systems.

CHAPTER V

CONCLUSION AND FUTURE WORK

Based on the results and discussion above, microscopic deformation mechanisms in the in situ MGMCs have been examined using synchrotron X-ray scattering and FEM under compressive loading in the present work. Different crystal geometries, including cubes/spheres/dendrites, are used to examine the inclusion-shape effects on the elastic strain evolution of the inclusions. The present work on MGMCs can provide some guidelines in the design and preparation of MGMCs. Moreover, the fatigue lifetime and endurance limit of most structural materials, including BMGs, can be enhanced by TFMG coatings, which would be helpful to the application of BMGs. However, the optimization of TFMG coatings for the fatigue-lifetime improvement of structural materials remains to be further studied. Based upon the present work, several approaches can be fruitfully conducted to study TFMG-coating effects on the fatigue behavior of substrate materials.

(a) TFMGs can be deposited on materials with medium strengths (fatigue-endurance limits), such as Ni-based alloys to increase the fatigue performance of substrates, because of the compatible fatigue deformation (fatigue-endurance limits) between substrates and TFMGs upon loading.

(b) The fatigue behavior of TFMG-substrate materials systems is clearly dependent on the adhesion properties between the substrate and coating. Thus, fatigue lifetime and endurance limit can be enhanced by increasing film/substrate adhesion. In previous studies [33, 152], a bilayer-coating has provided a feasible way to improve the

film/substrate adhesion, which a ductile thin film between the substrate and the TFMG for enhancing the adhesion.

(c) Multilayer coatings may indeed be a good approach to increase the fatigue behavior of substrate materials.

(d) The mechanical deformation mechanism of TFMGs on crystalline materials has been studied with finite-element and molecular dynamic simulations [32, 33]. However, the deformation behavior of bilayer coatings, together with multilayer coatings, remains to be further investigated.

REFERENCES

1. Klement W, Willens RH, Duwez P. Non-crystalline structure in solidified gold–silicon alloys. Nature 1960; 187:869.
2. Chen HS, Ferris SD, Gyorgy EM, Leamy HJ, Sherwood RC. Field heat treatment of ferromagnetic metallic glasses. Appl. Phys. Lett. 1975; 26:405.
3. Chen HS. Metallic glasses. Acta Metall. 1974; 1505.
4. Drehman AJ, Greer AL, Turnbull D. Bulk formation of a metallic glass: Pd40Ni40P20. Appl. Phys. Lett. 1982; 41:716.
5. Chen HS. Glassy metals. Rep. Prog. Phys. 1980; 43:353.
6. Inoue A, Takeuchi A, Zhang T. Ferromagnetic bulk amorphous alloys. Metall. Mater. Trans. A 1998; 29A:1779.
7. Inoue A. Stabilization of metallic supercooled liquid and bulk amorphous alloys. Acta Mater. 2000; 48:279.
8. Greer AL. Metallic glasses. Science 1995; 267:1947.
9. Greer AL, Ma E. Bulk metallic glasses: At the cutting edge of metals research. MRS Bull. 2007; 32:611.
10. Inoue A, Zhang T, Masumoto T. Al-La-Ni amorphous-alloys with a wide supercooled liquid region. Mater. Trans., JIM 1989; 30:965.
11. Inoue A, Nakamura T, Nishiyama N, Masumoto T. Mg-Cu-Y bulk amorphous-alloys with high-tensile strength produced by a high-pressure die-casting method. Mater. Trans., JIM 1992; 33:937.
12. Inoue A, Zhang T, Nishiyama N, Ohba K, Masumoto T. Preparation of 16 mm diameter rod of amorphous Zr65Al7.5Ni10Cu17.5 alloy. Mater. Trans., JIM 1993; 34:1234.

13. Inoue A, Zhang T. Fabrication of bulky Zr-based glassy alloys by suction casting into copper mold. Mater. Trans., JIM 1995; 36:1184.

14. Inoue A, Nishiyama N, Kimura H. Preparation and thermal stability of bulk amorphous Pd40Cu30Ni10P20 alloy cylinder of 72 mm in diameter. Mater. Trans., JIM 1997; 38:179.

15. Peker A, Johnson WL. A highly processable metallic glass: Zr41.2Ti13.8Cu12.5Ni10.0Be22.5. Appl. Phys. Lett. 1993; 63:2342.

16. Chen MW. Mechanical behavior of metallic glasses: Microscopic understanding of strength and ductility. Annu. Rev. Mater. Res. 2008; 38:445.

17. Qiao JW, Jia HL, Chuang CP, Huang EW, Wang GY, Liaw PK, Ren Y, Zhang Y. Low-temperature shear banding for a Cu-based bulk-metallic glass. Scripta Mater. 2010; 63:871.

18. Qiao JW, Jia HL, Zhang Y, Liaw PK, Li LF. Multi-step shear banding for bulk metallic glasses at ambient and cryogenic temperatures. Mater. Chem. Phys. 2012; 136:75.

19. Kai W, Wu YH, Chen WS, Tsay LW, Jia HL, Liaw PK. Air-oxidation behavior of a [(Fe50Co50)75B20Si5]96Nb4 bulk metallic glass at 500–650 ℃. Corros. Sci. 2013; 66:26.

20. Kai W, Wu YH, Chen WS, Huang RT, Jia HL, Liaw PK, Zhang T. Air-oxidation behavior of a [(Co50Cr15Mo14C15B6)97.5Er2.5]93Fe7 bulk-metallic glass at 873 K to 973 K (600 ℃ to 700 ℃). Metall. Mater. Trans. A 2012; 43:2721.

21. Miller MK, Liaw PK, Bulk metallic glasses, Springer-Verlag, New York, 2008.

22. Jia HL, Muntele CI, Huang L, Li X, Li G, Zhang T, He W, Liaw PK. A study on the surface structures and properties of Ni-free Zr-based bulk metallic glasses after Ar and Ca ion implantation. Intermetallics 2013; 41:35.

23. Li WD. Ductility enhancement and structural origin of ductile-brittle ransition in bulk metallic glasses. Ph.D. Thesis 2013.

24. Li WD, Bei H, Tong Y, Dmowski W, Gao YF. Structural heterogeneity induced plasticity in bulk metallic glasses: From well-relaxed fragile glass to metal-like behavior. Appl. Phys. Lett. 2013; 103:171910.

25. Song SX, Bei H, Wadsworth J, Nieh TG. Flow serration in a Zr-based bulk metallic glass in compression at low strain rates. Intermetallics 2008; 16:813.

26. Cheng YQ, Ma E. Atomic-level structure and structure-property relationship in metallic glasses. Prog. Mater Sci. 2011; 56:379.

27. Yang B, Morrison ML, Liaw PK, Buchanan RA, Wang GY, Liu CT, Denda M. Dynamic evolution of nanoscale shear bands in a bulk-metallic glass. Appl. Phys. Lett. 2005; 86:141904.

28. Zhang Y, Greer AL. Thickness of shear bands in metallic glasses. Appl. Phys. Lett. 2006; 89:071907.

29. Qiao JW, Wang S, Zhang Y, Liaw PK, Chen GL. Large plasticity and tensile necking of Zr-based bulk-metallic-glass-matrix composites synthesized by the Bridgman solidification. Appl. Phys. Lett. 2009; 94:151905.

30. Qiao JW, Sun AC, Huang EW, Zhang Y, Liaw PK, Chuang CP. Tensile deformation micromechanisms for bulk metallic glass matrix composites: From work-hardening to softening. Acta Mater. 2011; 59:4126.

31. Hofmann DC, Suh JY, Wiest A, Duan G, Lind ML, Demetriou MD. Designing metallic glass matrix composites with high toughness and tensile ductility. Nature 2008; 451:1085.

32. Chu JP, Jang JSC, Huang JC, Chou HS, Yang Y, Ye JC, Wang YC, Lee JW, Liu FX, Liaw PK, Chen YC, Lee CM, Li CL, Rullyani C. Thin film metallic glasses: Unique properties and potential applications. Thin Solid Films 2012; 520:5097.

33. Chu JP, Greene JE, Jang JSC, Huang JC, Shen YL, Liaw PK, Yokoyama Y, Inoue A, Nieh TG. Bendable bulk metallic glass: Effects of a thin, adhesive, strong, and ductile coating. Acta Mater. 2012; 60:3226.

34. Zhang Y, Wang WH, Greer AL. Making metallic glasses plastic by control of residual stress. Nat. Mater. 2006; 5:857.

35. Choi-Yim H, Johnson WL. Bulk metallic glass matrix composites. Appl. Phys. Lett. 1997; 71:3808.

36. Choi-Yim H. Synthesis and characterization of bulk metallic glass matrix composities. Ph.D Thesis California Institute of Technology:1999.

37. Conner RD, Choi-Yim H, Johnson WL. Mechanical properties of Zr57Nb5Al10Cu15.4Ni12.6 metallic glass matrix particulate composites. J. Mater. Res. 1999; 14:3292.

38. Choi-Yim H, Conner RD, Szuecs F, Johnson WL. Processing, microstructure and properties of ductile metal particulate reinforced Zr57Nb5Al10Cu15.4Ni12.6 bulk metallic glass composites. Acta Mater. 2002; 50:2737.

39. Siegrist ME, Löffler JF. Bulk metallic glass-graphite composites. Scripta Mater. 2007; 56:1079.

40. Liu T, Shen P, Qiu F, Zhang T, Jiang Q. Microstructures and mechanical properties of ZrC reinforced (Zr-Ti)-Al-Ni-Cu glassy composites by an in situ reaction. Adv. Eng. Mater. 2009; 11:392.

41. Dandliker RB, Conner RD, Johnson WL. Melt infiltration casting of bulk metallic-glass matrix composites. J. Mater. Res. 1998; 13:2896.

42. Conner RD, Dandliker RB, Johnson WL. Mechanical properties of tungsten and steel fiber reinforced Zr41.25Ti13.75Cu12.5Ni10Be22.5 metallic glass matrix composites. Acta Mater. 1998; 46:6089.

43. Choi-Yim H, Conner RD, Szuecs F, Johnson WL. Quasistatic and dynamic deformation of tungsten reinforced Zr57Nb5Al10Cu15.4Ni12.6 bulk metallic glass matrix composites. Scripta Mater. 2001; 45:1039.

44. Hou B, Li YL, Xing LQ, Chen CS, Kou HC, Li JS. Dynamic and quasi-static mechanical properties of fibre-reinforced metallic glass at different temperatures. Philos. Mag. Lett. 2007; 87:595.

45. Zhang HF, Li H, Wang AM, Fu HM, Ding BZ, Hu ZQ. Synthesis and characteristics of 80 vol.% tungsten (W) fibre/Zr based metallic glass composite. Intermetallics 2009; 17:1070.

46. Lee K, Son CY, Lee SB, Lee SK, Lee S. Direct observation of microfracture process in metallic-continuous-fiber-reinforced amorphous matrix composites fabricated by liquid pressing process. Mat. Sci. Eng. A 2010; 527:941.

47. Son C-Y, Kim GS, Lee S-B, Lee S-K, Kim HS, Huh H, Lee S. Correlation of microstructure with mechanical properties of Zr-based amorphous matrix

composite reinforced with tungsten continuous fibers and ductile dendrites. Metall. Mater. Trans. A 2012; 43:4088.

48. Khademian N, Gholamipour R. Fabrication and mechanical properties of a tungsten wire reinforced Cu-Zr-Al bulk metallic glass composite. Mat. Sci. Eng. A 2010; 527:3079.

49. Wadhwa P, Heinrich J, Busch R. Processing of copper fiber-reinforced Zr41.2Ti13.8Cu12.5Ni10.0Be22.5 bulk metallic glass composites. Scripta Mater. 2007; 56:73.

50. Kim Y, Shin SY, Kim JS, Huh H, Kim KJ, Lee S. Dynamic deformation behavior of Zr-based amorphous alloy matrix composites reinforced with STS304 or tantalum fibers. Metall. Mater. Trans. A 2012; 43:3023.

51. Kim GS, Lee S-B, Lee S-K, Kim HS, Lee S. Effect of fiber diameter on quasi-static and dynamic compressive properties of Zr-based amorphous matrix composites reinforced with stainless steel continuous fibers. Metall. Mater. Trans. A 2014; 45:1284.

52. Hui X, Yu J, Wang M, Dong W, Chen G. Wetting angle and infiltration velocity of Zr base bulk metallic glass composite. Intermetallics 2006; 14:931.

53. Qiao JW. In-situ dendrite/metallic glass matrix composites: A review. J. Mater. Sci. Technol. 2013; 29:685.

54. Fu XL, Li Y, Schuh CA. Temperature, strain rate and reinforcement volume fraction dependence of plastic deformation in metallic glass matrix composites. Acta Mater. 2007; 55:3059.

55. Chen G, Bei H, Cao Y, Gali A, Liu CT, George EP. Enhanced plasticity in a Zr-based bulk metallic glass composite with in situ formed intermetallic phases. Appl. Phys. Lett. 2009; 95:081908.

56. Du XH, Huang JC, Hsieh KC, Lai YH, Chen HM, Jang JSC, Liaw PK. Two-glassy-phase bulk metallic glass with remarkable plasticity. Appl. Phys. Lett. 2007; 91:131901.

57. Park BJ, Chang HJ, Kim DH, Kim WT, Chattopadhyay K, Abinandanan TA, Bhattacharyya S. Phase separating bulk metallic glass: A hierarchical composite. Phys. Rev. Lett. 2006; 96:245503.

58. Fan C, Li C, Inoue A. Deformation behavior of Zr-based bulk nanocrystalline amorphous alloys. Phys. Rev. B 2000; 61:3761.

59. Fan C, Inoue A. Ductility of bulk nanocrystalline composites and metallic glasses at room temperature. Appl. Phys. Lett. 2000; 77:46.

60. Kim YC, Na JH, Park JM, Kim DH, Lee JK, Kim WT. Role of nanometer-scale quasicrystals in improving the mechanical behavior of Ti-based bulk metallic glasses. Appl. Phys. Lett. 2003; 83:3093.

61. Inoue A, Zhang W, Tsurui T, Yavari AR, Greer AL. Unusual room-temperature compressive plasticity in nanocrystal-toughened bulk copper-zirconium glass. Philos. Mag. Lett. 2005; 85:221.

62. Chen MW, Inoue A, Fan C, Sakai A, Sakurai T. Fracture behavior of a nanocrystallized Zr65Cu15Al10Pd10 metallic glass. Appl. Phys. Lett. 1999; 74:2131.

63. Hajlaoui K, Yavari AR, Doisneau B, LeMoulec A, F. WJB, Vaughan G, Greer AL, Inoue A, Zhang W, Kvick Å. Shear delocalization and crack blunting of a metallic glass containing nanoparticles: In situ deformation in TEM analysis. Scripta Mater. 2006; 54:1829.

64. Yao KF, Ruan F, Yang YQ, Chen N. Superductile bulk metallic glass. Appl. Phys. Lett. 2006; 88:122106.

65. Liu YH, Wang G, Wang RJ, Zhao DQ, Pan MX, Wang WH. Super plastic bulk metallic glasses at room temperature. Science 2007; 315:1385.

66. Sopu D, Ritter Y, Gleiter H, Albe K. Deformation behavior of bulk and nanostructured metallic glasses studied via molecular dynamics simulations. Phys. Rev. B 2011; 83:100202.

67. Hays CC, Kim CP, Johnson WL. Microstructure controlled shear band pattern formation and enhanced plasticity of bulk metallic glasses containing in situ formed ductile phase dendrite dispersions. Phys. Rev. Lett. 2000; 84:2901.

68. Lee SY, Kim CP, Almer JD, Lienert U, Ustundag E, Johnson WL. Pseudo-binary phase diagram for Zr-based in situ beta phase composites. J. Mater. Res. 2007; 22:538.

69. Qiao JW, Zhang Y, Chen GL. Fabrication and mechanical characterization of a series of plastic Zr-based bulk metallic glass matrix composites. Mater. Des. 2009; 30:3966.

70. Szuecs F, Kim CP, Johnson WL. Mechanical properties of $Zr_{56.2}Ti_{13.8}Nb_{5.0}Cu_{6.9}Ni_{5.6}Be_{12.5}$ ductile phase reinforced bulk metallic glass composites. Acta Mater. 2001; 49:1507.

71. Qiao JW, Zhang Y, Feng P, Zhang QM, Chen GL. Strain rate response of mechanical behaviors for a Zr-based bulk metallic glass matrix composite. Mat. Sci. Eng. A 2009; 515:141.

72. Bracchi A, Huang Y-L, Seibt M, Schneider S, Thiyagarajan P. Decomposition and metastable phase formation in the bulk metallic glass matrix composite Zr56Ti14Nb5Cu7Ni6Be12. J. Appl. Phys. 2006; 99:123519.

73. Löser W, Das J, Güth A, Klauß H-J, Mickel C, Kühn U, Eckert J, Roy SK, Schultz L. Effect of casting conditions on dendrite-amorphous/nanocrystalline Zr–Nb–Cu–Ni–Al in situ composites. Intermetallics 2004; 12:1153.

74. Wu FF, Zhang ZF, Mao SX, Peker A, Eckert J. Effect of annealing on the mechanical properties and fracture mechanisms of a Zr56.2Ti13.8Nb5.0Cu6.9Ni5.6Be12.5 bulk-metallic-glass composite. Phys. Rev. B 2007; 75:134201.

75. Roberts S, Zachrisson C, Kozachkov H, Ullah A, Shapiro AA, Johnson WL, Hofmann DC. Cryogenic Charpy impact testing of metallic glass matrix composites. Scripta Mater. 2012; 66:284.

76. Cheng J-L, Chen G, Liu C-T, Li Y. Innovative approach to the design of low-cost Zr-based BMG composites with good glass formation. Sci. Rep. 2013; 3:2097.

77. He G, Eckert J, Löser W, Schultz L. Novel Ti-base nanostructure–dendrite composite with enhanced plasticity. Nat. Mater. 2003; 2:33.

78. Guo FQ, Poon SJ, Shiflet GJ. Networking amorphous phase reinforced titanium composites which show tensile plasticity. Philos. Mag. Lett. 2008; 88:615.

79. Hofmann DC, Suh JY, Wiest A, Lind ML, Demetriou MD, Johnson WL. Development of tough, low-density titanium-based bulk metallic glass matrix composites with tensile ductility. PNAS 2008; 105:20136.

80. Qiao JW, Zhang JT, Jiang F, Zhang Y, Liaw PK, Ren Y, Chen GL. Development of plastic Ti-based bulk-metallic-glass-matrix composites by controlling the microstructures. Mat. Sci. Eng. A 2010; 527:7752.

81. Oh YS, Kim CP, Lee S, Kim NJ. Microstructure and tensile properties of high-strength high-ductility Ti-based amorphous matrix composites containing ductile dendrites. Acta Mater. 2011; 59:7277.

82. Jeon C, Kim CP, Joo S-H, Kim HS, Lee S. High tensile ductility of Ti-based amorphous matrix composites modified from conventional Ti–6Al–4V titanium alloy. Acta Mater. 2013; 61:3012.

83. Qiao JW, Zhang T, Yang FQ, Liaw PK, Pauly S, Xu BS. A tensile deformation model for in-situ dendrite/metallic glass matrix composites. Sci. Rep. 2013; 3:2816.

84. Fan JT, Zhang ZF, Shen BL, Mao SX. Plastic deformation of a Co-based metallic glass composite with in situ precipitated dendritic phases. Scripta Mater. 2008; 59:603.

85. Ferry M, Laws KJ, White C, Miskovic DM, Shamlaye KF, Xu W, Biletska O. Recent developments in ductile bulk metallic glass composites. MRS Communications 2013; 3:1.

86. Lee ML, Li Y, Schuh CA. Effect of a controlled volume fraction of dendritic phases on tensile and compressive ductility in La-based metallic glass matrix composites. Acta Mater. 2004; 52 4121.

87. Zhang Y, Xu W, Tan H, Li Y. Microstructure control and ductility improvement of La–Al–(Cu, Ni) composites by Bridgman solidification. Acta Mater. 2005; 53:2607.

88. Chen ZP, Gao JE, Wu Y, Wang H, Liu XJ, Lu ZP. Designing novel bulk metallic glass composites with a high aluminum content. Sci. Rep. 2013; 3:3353.

89. Guo SF, Liu L, Li N, Li Y. Fe-based bulk metallic glass matrix composite with large plasticity. Scripta Mater. 2010; 62:329.

90. Gao JE, Chen ZP, Du Q, Li HX, Wu Y, Wang H, Liu XJ, Lu ZP. Fe-based bulk metallic glass composites without any metalloid elements. Acta Mater. 2013; 61:3214.

91. Fan C, Ott RT, Hufnagel TC. Metallic glass matrix composite with precipitated ductile reinforcement. Appl. Phys. Lett. 2002; 81:1020.

92. Qiao JW, Zhang Y. Intermetallics 2011; 19:149.

93. He G, Zhang ZF, Löser W, Eckert J, Schultz L. Effect of Ta on glass formation, thermal stability and mechanical properties of a Zr52.25Cu28.5Ni4.75Al9.5Ta5 bulk metallic glass. Acta Mater. 2003; 51:2383.

94. Bian Z, Kato H, Qin C, Zhang W, Inoue A. Cu–Hf–Ti–Ag–Ta bulk metallic glass composites and their properties. Acta Mater. 2005; 53:2037.

95. Ott RT, Sansoz F, Jiao T, Warner D, Fan C, Molinari JF, Ramesh KT, Hufnagel TC. Yield criteria and strain-rate behavior of Zr57.4Cu16.4Ni8.2Ta8Al10 metallic-glass-matrix composites. Metall. Mater. Trans. A 2006; 37:3251.

96. Li C, Jang JSC, Li JB, Pan DJ, Jian SR, Huang JC, Nieh TG. Numerical and experimental studies on the shear band intervention in zirconium based bulk metallic glass composites Zr53Cu22Ni9Al8Ta8. Intermetallics 2012; 30:111.

97. Liu ZQ, Liu G, Qu RT, Zhang ZF, Wu SJ, Zhang T. Microstructural percolation assisted breakthrough of trade-off between strength and ductility in CuZr-based metallic glass composites. Sci. Rep. 2014; 4:4167.

98. Nan CW. Physics of inhomogeneous inorganic materials. Prog. Mater Sci. 1993; 37:1.

99. Song KK. Synthesis, microstructure, and deformation mechanisms of CuZr-based bulk metallic glass composites. Ph.D. Thesis 2013.

100. Wu Y, Zhou DQ, Song WL, Wang H, Zhang ZY, Ma D, Wang XL, Lu ZP. Ductilizing bulk metallic glass composite by tailoring stacking fault energy. Phys. Rev. Lett. 2012; 109:245506.

101. Inoue A, Yokoyama Y, Shinohara K, Masumoto T. Preparation of bulky Zr-based amorphous alloys by a zone melting method. Mater. Trans., JIM 1994; 35:923.

102. Wall JJ, Fan C, Liaw PK, Liu CT, Choo H. A combined drop/suction-casting machine for the manufacture of bulk-metallic-glass materials. Rev. Sci. Instrum. 2006; 77 033902.

103. Xie G, Louzguine-Luzgin DV, Kimura H, Inoue A, Wakai F. Large-size ultrahigh strength Ni-based bulk metallic glassy matrix composites with enhanced ductility fabricated by spark plasma sintering. Appl. Phys. Lett. 2008; 92:121907.

104. Tamura T, Amiya K, Rachmat R, Mizutani Y, Miwa K. Electromagnetic vibration process for producing bulk metallic glasses. Nat. Mater. 2005; 4:289.

105. Yang G, Lin X, Liu F, Hu Q, Ma L, Li J, Huang W. Laser solid forming Zr-based bulk metallic glass. Intermetallics 2012; 22:110.

106. Laws KJ, Gun B, Ferry M. Large-scale production of Ca65Mg15Zn20 bulk metallic glass samples by low-pressure die-casting. Mat. Sci. Eng. A 2008; 475:348.

107. Dong T, Yang B, He J, Zhang Y. Preparation of melt-atomized and spray-deposited La62Al15.7(Cu, Ni)22.3 amorphous alloy with large size. Acta Metallurgica Sinica 2008; 44 659.

108. Zhang T, Zhang X, Zhang W, Jia F, Inoue A, Hao H, Ma Y. Study on continuous casting of bulk metallic glass. Mater. Lett. 2011; 65:2257.

109. Sheng HW, Luo WK, Alamgir FM, Bai J, Ma E. Atomic packing and short-to-medium-range order in metallic glasses. Nature 2006; 439:419.

110. Miracle DB, Louzguine-Luzgin DV, Louzguina-Luzgina LV, Inoue A. An assessment of binary metallic glasses: Correlations between structure, glass forming ability and stability. Int. Mater. Rev. 2010; 55:218.

111. Li Y, Guo Q, Kalb JA, Thompson CV. Matching glass-forming ability with the density of the amorphous phase. Science 2008; 322:1816.

112. Ding S, Liu Y, Li Y, Liu Z, Sohn S, Walker FJ, Schroers J. Combinatorial development of bulk metallic glasses. Nat. Mater. 2014; 13:494.

113. Yang J, Chung DDL. Casting particulate and fibrous metal-matrix composites by vacuum infiltration of a liquid metal under an inert gas pressure. J. Mater. Sci. 1989; 24:3605.

114. Hillig WB. Melt infiltration approach to ceramic matrix composites. J. Am. Ceram. Soc. 1988; 71:96.

115. Xu YK, Ma H, Xu J, Ma E. Mg-based bulk metallic glass composites with plasticity and gigapascal strength. Acta Mater. 2005; 53:1857.

116. Chen C, Xue Y, Wang L, Cheng X, Wang F, Wang Z, Zhang H, Wang A. Effect of Temperature on the Dynamic Mechanical Behaviors of Zr-Based Metallic Glass Reinforced Porous Tungsten Matrix Composite. Adv. Eng. Mater. 2012; 14:439.

117. Xue YF, Cai HN, Wang L, Wang FC, Zhang HF. Strength-improved Zr-based metallic glass/porous tungsten phase composite by hydrostatic extrusion. Appl. Phys. Lett. 2007; 90:081901.

118. Jang JSC, Ciou JY, Hung TH, Huang JC, Du XH. Enhanced mechanical performance of Mg metallic glass with porous Mo particles. Appl. Phys. Lett. 2008; 92:011930.

119. Jang JSC, Ciou JY, Li TH, Huang JC, Nieh TG. Dispersion toughening of Mg-based bulk metallic glass reinforced with porous Mo particles. Intermetallics 2010; 18:451.

120. Sun Y, Zhang HF, Wang AM, Fu HM, Hu ZQ, Wen CE, Hodgson PD. Mg-based metallic glass/titanium interpenetrating phase composite with high mechanical performance. Appl. Phys. Lett. 2009; 95:171910.

121. Kinaka M, Kato H, Hasegawa M, Inoue A. High specific strength Mg-based bulk metallic glass matrix composite highly ductilized by Ti dispersoid. Mat. Sci. Eng. A 2008; 494:299.

122. Chen YL, Wang AM, Fu HM, Zhu ZW, Zhang HF, Hu ZQ, Wang L, Cheng HW. Preparation, microstructure and deformation behavior of Zr-based metallic glass/porous SiC interpenetrating phase composites. Mat. Sci. Eng. A 2011; 530:15.

123. Son C-Y, Kim CK, Shin SY, Lee S. In situ microfracture observation of Cu-based amorphous alloy matrix composites containing copper or brass particles. Mat. Sci. Eng. A 2009; 508:15.

124. Chu ZH, Kato H, Xie GQ, Yuan GY, Ding WJ. Consolidation and mechanical properties of Cu 46 Zr 42 Al 7 Y 5 metallic glass by spark plasma sintering. Metall. Mater. Trans. A 2013; 44:4595.

125. Madge SV, Sharma P, Louzguine-Luzgin DV, Greer AL, Inoue A. New La-based glass–crystal ex situ composites with enhanced toughness. Scripta Mater. 2010; 62:210.

126. Eardley ES, Flower HM. Infiltration and solidification of commercial purity aluminium matrix composites. Mat. Sci. Eng. A 2003; 359:303.

127. Tjong SC, Ma ZY. Microstructural and mechanical characteristics of in situ metal matrix composites. Mat. Sci. Eng. R 2000; 29:49.

128. Kong J, Ye Z-T, Lv F. Non-equilibrium solidification character of Zr56.2Ti13.8Nb5.0Cu6.9Ni5.6Be12.5 bulk metallic glass composites containing ductile dendrite phase. J. Alloys Compd. 2009; 478:202.

129. Qiao JW, Zhang Y, Zheng ZL, He JP, Wei BC. Synthesis of plastic Zr-based bulk metallic glass matrix composites by the copper-mould suction casting and the Bridgman solidification. J. Alloys Compd. 2009; 477:436.

130. Liu Z, Li R, Liu G, Su W, Wang H, Li Y, Shi M, Luo X, Wu G, Zhang T. Microstructural tailoring and improvement of mechanical properties in CuZr-based bulk metallic glass composites. Acta Mater. 2012; 60:3128.

131. Jeon C, Ha DJ, Kim CP, Lee S. Effects of dendrite size on tensile deformation behavior in Zr-based amorphous matrix composites containing ductile dendrites. Metall. Mater. Trans. A 2012; 43:3663.

132. Sun GY, Chen G, Liu CT, Chen GL. Innovative processing and property improvement of metallic glass based composites. Scripta Mater. 2006; 55:375.

133. Qiao JW, Zhang Y, Yang HJ, Sang SB. Dendritic and spherical crystal reinforced metallic glass matrix composites. Int. J. Miner. Metall. Mater. 2013; 20:386.

134. Huang HJ, Cai YH, Cui H, Huang JF, He JP, Zhang JS. Influence of Mn addition on microstructure and phase formation of spray-deposited Al–25Si–xFe–yMn alloy. Mat. Sci. Eng. A 2009; 502:118.

135. Hofmann DC, Suh J-Y, Wiest A, Johnson W. New processing possibilities for highly toughened metallic glass matrix composites with tensile ductility. Scripta Mater. 2008; 59:684.

136. Hofmann DC, Kozachkov H, Khalifa HE, Schramm JP, Demetriou MD, Vecchio KS, Johnson WL. Semi-solid induction forging of metallic glass matrix composites. JOM 2009; 61:11.

137. Kurz W, Giovanola B, Trivedi R. Theory of microstructural development during rapid solidification. Acta Metall. 1986; 34:823.

138. Zhang Y, Tan H, Li Y. Bulk glass formation of 12 mm Rod in La-Cu-Ni-Al alloys. Mat. Sci. Eng. A 2004; 375-377:436.

139. Li Y, Ng SC, Lu ZP, Feng YP. Easy glass formation in La55Ni20Al25 by Bridgman solidification. Mater. Lett. 1998; 34:318.

140. Tan H, Zhang Y, Hu X, Feng YP, Li Y. Synthesis of in situ bulk glass matrix composite in by Bridgman method. Mat. Sci. Eng. A 2004; 375-377:407.

141. Tan H, Zhang Y, Li Y. Synthesis of La-based in-situ bulk metallic glass matrix composite. Intermetallics 2002; 10:1203.

142. Qiao JW, Zhang Y, Liaw PK. Tailoring Microstructures and Mechanical Properties of Zr-Based Bulk Metallic Glass Matrix Composites by the Bridgman Solidification. Adv. Eng. Mater. 2008; 10 1039.

143. Qiao JW, Feng P, Zhang Y, Zhang QM, Chen GL. Quasi-static and dynamic deformation behaviors of Zr-based bulk metallic glass composites fabricated by the Bridgman solidification. J. Alloys Compd. 2009; 486:527.

144. Qiao JW, Feng P, Zhang Y, Zhang QM, Liaw PK, Chen GL. Quasi-static and dynamic deformation behaviors of in situ Zr-based bulk-metallic-glass-matrix composites. J. Mater. Res. 2010; 25:2264.

145. Zhang JT, Qiao JW, Zhang Y. Synthesis of plastic lightweight Ti-based metallic-glass-matirx composites by Bridgman solidification. Acta Metallurgica Sinica 2011; 47:236.

146. Wang YS, Hao GJ, Zhang Y, Lin JP, Qiao JW. Fabrication and Mechanical Characterization of Ti-Based Metallic Glass Matrix Composites by the Bridgman Solidification. Metall. Mater. Trans. A 2014; 45:2359.

147. Qiao JW, Jia HL, Liaw PK. Unpublished Work.

148. Stoudt M, Cammarata RC, Ricker RE. Suppression of fatigue cracking with nanometer-scale multilayered coatings. Scripta Mater. 2000; 43:491.

149. Kim KR, Suh CM, Murakami RI, Chung CW. Effect of intrinsic properties of ceramic coatings on fatigue behavior of Cr–Mo–V steels. Surf. Coat. Technol. 2003; 171:15.

150. Cairney JM, Tsukano R, Hoffman MJ, Yang M. Degradation of TiN coatings under cyclic loading. Acta Mater. 2004; 52:3229.

151. Chu JP, Huang JC, Jang JSC, Wang YC, Liaw PK. Thin film metallic glasses: Preparations, properties, and applications. JOM 2010; 62:19.

152. Chang YZ, Tsai PH, Li JB, Lin HC, Jang SCJ, Li C, Chen GJ, Chen YC, Chu JP, Liaw PK. Zr-based metallic glass thin film coating for fatigue-properties improvement of 7075-T6 aluminum alloy. Thin Solid Films 2013; 544:331

153. Jaeger G, Endler B, Bartsch K, Heilmaier M, Leonhardt A. Fatigue behavior of duplex treated TiC x N 1−x-and Ti 1− x Alx N-hard coating steel compounds. Surf. Coat. Technol. 2002; 150:282.

154. Mackerle J. Coatings and surface modification technologies: A finite element bibliography (1995–2005). Modell. Simul. Mater. Sci. Eng. 2005; 13:935.

155. Jia HL, Liu FX, An ZN, Li WD, Wang GY, Chu JP, Jang JSC, Gao YF, Liaw PK. Thin-film metallic glasses for substrate fatigue-property improvements. Thin Solid Films 2014; 561:2.

156. Liu FX, Liaw PK, Jiang WH, Chiang CL, Gao YF, Guan YF, Chu JP, Rack PD. Fatigue-resistance enhancements by glass-forming metallic films. Mat. Sci. Eng. A 2007; 468-470:246.

157. Liu FX, Chiang CL, Chu JP, Gao YF, Liaw PK. Effects of glass-forming metallic film on the fatigue behavior of C-2000 Ni-based alloy. Mater. Res. Soc. Symp. Proc. 2006; 903E:0903.

158. Lee CM, Chu JP, Chang WZ, Lee JW, Jang JSC, Liaw PK. Fatigue Property Improvements of Ti-6Al-4V by Thin Film Coatings of Metallic Glass and TiN: A Comparison Study. Thin Solid Films 2013; 561:33.

159. Chiang CL, Chu JP, Liu FX, Liaw PK, Buchanan RA. A 200nm thick glass-forming metallic film for fatigue-property enhancements. Appl. Phys. Lett. 2006; 88:131902.

160. Guo H, Yan PF, Wang YB, Tan J, Zhang ZF, Sui ML, Ma E. Tensile ductility and necking of metallic glass. Nat. Mater. 2007; 6:735.

161. Jang D, Greer JR. Transition from a strong-yet-brittle to a stronger-and-ductile state by size reduction of metallic glasses. Nat. Mater. 2000; 9:215.

162. Ma CL, Inoue A. Bulk glassy Pd-Cu-Ni-Cr-P alloys containing dispersed nanoparticles prepared by copper-mold casting. Mater. Trans., JIM 2002; 7:1737.

163. Ma CL, Inoue A. Microstructure and mechanical properties of Cr, Mo, Fe, Ta modified. Mater. Trans., JIM 2003; 1:188.

164. Ott RT, Sansoz F, Molinari JF, Almer J, Ramesh KT, Hufnagel TC. Micromechanics of deformation of metallic-glass–matrix composites from in situ synchrotron strain measurements and finite element modeling. Acta Mater. 2005; 53:1883.

165. Ott RT, Fan C, Li J, Hufnagel TC. Structure and properties of Zr–Ta–Cu–Ni–Al bulk metallic glasses and metallic glass matrix composites. J. Non-Cryst. Solids 2003; 317:158.

166. Qiao JW, Ma SG, Wang GY, Jiang F, Liaw PK, Zhang Y. Tension-tension-fatigue behaviors of a Zr-Based bulk-metallic-glass-matrix composite. Metall. Mater. Trans. A 2011; 42:2530.

167. Qiao JW, Zhang Y, Liaw PK, Chen GL. Micromechanisms of plastic deformation of a dendrite/Zr-based bulk-metallic-glass composite. Scripta Mater. 2009; 61:1087.

168. Qiao JW, Zhang Y, Jia HL, Yang HJ, Liaw PK, Xu BS. Tensile softening of metallic-glass-matrix composites in the supercooled liquid region. Appl. Phys. Lett. 2012; 100:121902.

169. Launey ME, Hofmann DC, Suh JY, Kozachkov H, Johnson WL, Ritchie RO. Fracture toughness and crack resistance curve behavior in metallic glass matrix composites. Appl. Phys. Lett. 2009; 94:241910.

170. Balch DK, Üstündag E, Dunand DC. Diffraction strain measurements in a partially crystallized bulk metallic glass composite containing ductile particles. J. Non-Cryst. Solids 2003; 317:176.

171. Balch DK, Üstündag E, Dunand DC. Elasto-plastic load transfer in bulk metallic glass composites containing ductile particles. Metall. Mater. Trans. A 2003; 34A:1787.

172. Clausen B, Lee SY, Üstündag E, Kim CNP, Brown DW, Bourke MAM. Deformation of in-situ-reinforced bulk metallic glass matrix composites. Mater. Sci. Forum 2002; 404-407:553.

173. Clausen B, Lee S, Üstündag E, Kim C, Brown D, Bourke M. Compressive deformation of in situ formed bulk metallic glass composites. Scripta Mater. 2006; 54:343.

174. Li L, Ungár T, Wang YD, Morris JR, Tichy G, Lendvai J, Yang YL, Ren Y, Choo H, Liaw PK. Microstructure evolution during cold rolling in a nanocrystalline Ni–Fe alloy determined by synchrotron X-ray diffraction. Acta Mater. 2009; 57:4988.

175. Li L, Ungar T, Wang Y, Fan G, Yang Y, Jia N, Ren Y, Tichy G, Lendvai J, Choo H, Liaw PK. Simultaneous reductions of dislocation and twin densities with grain growth during cold rolling in a nanocrystalline Ni–Fe alloy. Scripta Mater. 2009; 60:317.

176. Li H, Choo H, Ren Y, Saleh T, Lienert U, Liaw P, Ebrahimi F. Strain-dependent deformation behavior in nanocrystalline metals. Phys. Rev. Lett. 2008; 101:015502.

177. Wang YD, Huang EW, Ren Y, Nie ZH, Wang G, Liu YD, Deng JN, Choo H, Liaw PK, Brown DE, Zuo L. In situ high-energy X-ray studies of magnetic-field-induced phase transition in a ferromagnetic shape memory Ni–Co–Mn–In alloy. Acta Mater. 2008; 56:913.

178. Wang YD, Ren Y, Huang EW, Nie ZH, Wang G, Liu YD, Deng JN, Zuo L, Choo H, Liaw PK, Brown DE. Direct evidence on magnetic-field-induced phase transition in a NiCoMnIn ferromagnetic shape memory alloy under a stress field. Appl. Phys. Lett. 2007; 90:101917.

179. Barabash R, Gao Y, Sun Y, Lee SY, Choo H, Liaw PK, Brown DW, Ice GE. Neutron and X-ray diffraction studies and cohesive interface model of the fatigue crack deformation behavior. Philos. Mag. Lett. 2008; 88:553.

180. Huang SY, Brown DW, Clausen B, Teng ZK, Gao YF, Liaw PK. In situ neutron-diffraction studies on the creep behavior of a ferritic superalloy. Metall. Mater. Trans. A 2011; 43:1497.

181. Zheng LL, Gao YF, Lee SY, Barabash RI, Lee JH, Liaw PK. Intergranular strain evolution near fatigue crack tips in polycrystalline metals. J. Mech. Phys. Solids 2011; 59:2307.

182. Zheng LL, Gao YF, Wang YD, Stoica AD, An K, Wang XL. Grain orientation dependence of lattice strains and intergranular damage rates in polycrystals under cyclic loading. Scripta Mater. 2013; 68:265.

183. McCusker LB, Von Dreele RB, Cox DE, LoueÈrd D, Scardie P. Rietveld refinement guidelines. J. Appl. Cryst. 1999; 32:36.

184. Chen MW, Inoue A, Zhang W, Sakurai T. Extraordinary plasticity of ductile bulk metallic glasses. Phys. Rev. Lett. 2006; 96:245502.

185. Jiang QK, Liu P, Ma Y, Cao QP, Wang XD, Zhang DX, Han XD, Zhang Z, Jiang JZ. Super elastic strain limit in metallic glass films. Sci. Rep. 2012; 2:852.

186. Jia HL, Zheng LL, Li WD, Li N, Qiao JW, Wang GY, Ren Y, Liaw PK, Gao Y. Insights from the lattice-strain evolution on deformation mechanisms in metallic-glass-matrix composites. Metall. Mater. Trans. A 2015; In Press, DOI:10.1007/s11661.

187. Hammersley AP, Svensson SO, Hanfland M, Fitch AN, Hausermann D. Two-dimensional detector software: From real detector to idealised image or two-theta scan. High Pressure Res. 1996; 14:a235.

188. Huang YG, A user-material subroutine incorporating single crystal plasticity in the ABAQUS finite element program, Mechanics Report 179, Division of Engienering and Applied Science, Harvard University, 1991.

189. Gao YF. An implicit finite element method for simulating inhomogeneous deformation and shear bands of amorphous alloys based on the free-volume model. Modell. Simul. Mater. Sci. Eng. 2006; 14:1329.

190. Spaepen F. A microscopic mechanism for steady state inhomogeneous flow in metallic glasses. Acta Metall. 1977; 25:407.

191. An ZN, Li WD, Liu FX, Liaw PK, Gao YF. Interface constraints on shear band patterns in bonded metallic glass films under microindentation. Metall. Mater. Trans. A 2012; 43:2729.

192. Liu MC, Huang JC, Chen KW, Lin JF, Li WD, Gao YF, Nieh TG. Is the compression of tapered micro- and nanopillar samples a legitimate technique for the identification of deformation mode change in metallic glasses? Scripta Mater. 2012; 66:817.

193. Peirce D, Asaro RJ, Needleman A. An analysis of nonuniform and localized deformation in ductile single crystals. Acta Metall. 1982; 30:1087.

194. Bower AF, Wininger E. A two-dimensional finite element method for simulating the constitutive response and microstructure of polycrystals during high temperature plastic deformation. J. Non-Cryst. Solids 2004; 52:1289.

195. Wong SL, Dawson PR. Influence of directional strength-to-stiffness on the elastic–plastic transition of fcc polycrystals under uniaxial tensile loading. Acta Mater. 2010; 58:1658.

196. Eshelby JD. The determination of the elastic field of an ellipsoidal inclusion, and related problems. P. Roy. Soc. Lond. A 1957; 241:376.

197. Lee S-Y, Clausen B, Üstündag E, Choi-Yim H, Aydiner CC, Bourke MAM. Compressive behavior of wire reinforced bulk metallic glass matrix composites. Mat. Sci. Eng. A 2005; 399:128.

198. Clausen B, Lee SY, Üstündag E, Aydiner CC, Conner RD, Bourke MAM. Compressive yielding of tungsten fiber reinforced bulk metallic glass composites. Scripta Mater. 2003; 49:123.

199. Dragoi D, Üstündag E, Clausen B, Bourke MAM. Investigation of thermal residual stresses in tungsten-fiber bulk metallic glass matrix composites. Scripta Mater. 2001; 45:245.

200. Kim YC, Fleury E, Lee J-C, Kim DH. Origin of the simultaneous improvement of strength and plasticity in Ti-based bulk metallic glass matrix composites. J. Mater. Res. 2005; 20:2474.

201. Sarac B, Schroers J. Designing tensile ductility in metallic glasses. Nat. Commun. 2013; 4:2158.

202. Pauly S, Liu G, Wang G, Kühn U, Mattern N, Eckert J. Microstructural heterogeneities governing the deformation of Cu47.5Zr47.5Al5 bulk metallic glass composites. Acta Mater. 2009; 57:5445.

203. Montanari R, Sili A, Costanza G. Improvement of the fatigue behaviour of Al 6061/20% SiC p composites by means of titanium coatings. Compos. Sci. Technol. 2001; 61:2047.

204. Tsuchiya T, Hirata M, Chiba N, Udo R, Yoshitomi Y, Ando T, Sato K, Takashima K, Higo Y, Saotome Y, Ogawa H, Ozaki K. Cross comparison of thin-film tensile-testing methods examined using single-crystal silicon, polysilicon, nickel, and titanium film. J. Microelectromech. S. 2005; 14:1178

205. Pardoen T, Coulombier M, Boe A, Safi A, Brugger C, Ryelandt S, Carbonnelle P, Gravier S, Raskin J-P. Ductility of Thin Metallic Films. Mater. Sci. Forum 2009; 633-634:615.

206. Colla MS, Wang B, Idrissi H, Schryvers D, Raskin JP, Pardoen T. High strength-ductility of thin nanocrystalline palladium films with nanoscale twins: On-chip testing and grain aggregate model. Acta Mater. 2012; 60:1795.

207. Niu RM, Liu G, Ding XD, Sun J. Ductility of metal thin film in flexible electronics. Sci. China Ser. E-Tech. Sci. 2008; 51:1971.

208. Hu K, Cao ZH, Wang L, She QW, Meng XK. Annealing improved ductility and fracture toughness of nanocrystalline Cu films on flexible substrates. J. Phys. D: Appl. Phys. 2012; 45:375305.

209. Augis JA, Lo CC, Pineel MR. The hardness and ductility of sputtered gold films. Thin Solid Films 1979; 58:357

210. Qin M, Ji V, Xu JH, Li JB, Xu KW, Ma SL. Yield strength determination of TiN film by in-situ XRD stress analysis method. Mater. Sci. Forum 2002; 404-407:671.

211. Ogbuji LUJT, Harding DR. A novel method for determining the strength of PECVD silicon nitride films. Thin Solid Films 1995; 263:194.

212. Edwards RL, Coles G, Sharpe WN. Comparison of tensile and bulge tests for thin-film silicon nitride. Exp. Mech. 2004; 44:49.

213. Mearini GT, Hoffman RW. Tensile properties of aluminum/alumina multi-layered thin films. J. Electron. Mater. 1993; 22:623

214. Liu MC, Huang JC, Chou HS, Lai YH, Lee CJ, Nieh TG. A nanoscaled underlayer confinement approach for achieving extraordinarily plastic amorphous thin film. Scripta Mater. 2009; 61:840.

215. Tian L, Cheng YQ, Shan ZW, Li J, Wang CC, Han XD, Sun J, Ma E. Approaching the ideal elastic limit of metallic glasses. Nat. Commun. 2012; 3:609.

216. Deng QS, Cheng YQ, Yue YH, Zhang L, Zhang Z, Han XD, Ma E. Uniform tensile elongation in framed submicron metallic glass specimen in the limit of suppressed shear banding. Acta Mater. 2011; 59:6511.

217. Jang DC, Greer JR. Transition from a strong-yet-brittle to a stronger-and-ductile state by size reduction of metallic glasses. Nat. Mater. 2010; 9:215.

218. Zhu Z, Zhang H, Pan D, Sun W, Hu Z. Fabrication of binary Ni-Nb bulk metallic glass with high strength and compressive plasticity. Adv. Eng. Mater. 2006; 8:953.

219. Chu JP, Lee CM, Huang RT, Liaw PK. Zr-based glass-forming film for fatigue-property improvements of 316L stainless steel: Annealing effects. Surf. Coat. Technol. 2011; 205:4030.

220. http://www.aksteel.com/pdf/markets_products/stainless/austenitic/316_316L_Data_Bulletin.pdf.

221. http://www.haynesintl.com/HASTELLOYC2000Alloy/HASTELLOYC2000AlloyPF.htm.

222. http://www.firmetal.com/Grade702.asp.

223. http://asm.matweb.com/search/SpecificMaterial.asp?bassnum=MTP642.

224. http://asm.matweb.com/search/SpecificMaterial.asp?bassnum=MA7075T6.

225. Chu J, Liu C, Mahalingam T, Wang S, O'Keefe M, Johnson B, Kuo C. Annealing-induced full amorphization in a multicomponent metallic film. Phys. Rev. B 2004; 69:113410.

226. Chiang CL. Study on multicomponent Cu- and Zr-based metallic films and their applications. Ph.D. Thesis 2006.

227. Jun SI, Rack PD, Mcknight TE, Melechko AV, Simpson ML. Electrical and microstructural characterization of molybdenum tungsten electrodes using a combinatorial thin film sputtering technique. Appl. Phys. Lett. 2005; 87:132108.

228. Chu JP. Annealing-induced morphization in a glass-forming thin film. JOM 2009; 61:72.

229. Chu JP, Wang CY, Chen LJ, Chen Q. Annealing-induced amorphization in a sputtered glass-forming film: In-situ transmission electron microscopy observation. Surf. Coat. Technol. 2011; 205:2914.

230. Rudnicki JW, Rice JR. Conditions for the localization of deformation in pressure-sensitive dilatant materials. J. Mech. Phys. Solids 1975; 23:371.

231. Gao YF, Wang L, Bei H, Nieh TG. On the shear band direction in metallic glasses. Acta Mater. 2011; 59:4159.

232. Hemphill MA, Yuan T, Wang GY, Yeh JW, Tsai CW, Chuang A, Liaw PK. Fatigue behavior of Al0.5CoCrCuFeNi high entropy alloys. Acta Mater. 2012; 60:5723.

233. Liu CT, Heatherly L, Easton DS, Carmichael CA, Schneibel JH, Chen CH, Wright JL, Yoo MH, Horton JA, Inoue A. Test environments and mechanical properties of Zr-base bulk amorphous alloys. Metall. Mater. Trans. A 1998; 29A:1811.

234. Wang G, Liaw P, Peter A, Yang B, Benson M, Yuan W, Peter W, Huang L, Freels A, Buchanan R, Liu C, Brooks C. Fatigue behavior of Zr-Ti-Ni-Cu-Be bulk-metallic glasses. Intermetallics 2005; 13:429.

235. Wang GY, Liaw PK, Peker A, Yang B, Benson ML, Yuan W, Peter WH, Huang L, Freels M, Buchanan RA, Liu CT, Brooks CR. Fatigue behavior of Zr–Ti–Ni–Cu–Be bulk-metallic glasses. Intermetallics 2005; 13:429.

236. Gilbert CJ, Schroeder V, Ritchie RO. Mechanisms for fracture and fatigue-crack propagation in a bulk metallic glass. Metall. Mater. Trans. A 1999; 30A:1739.

237. Yokoyama Y, Nishiyama N, Fukaura K, Sunada H. Fatigue properties and microstructures of Zr55Cu30Al10Ni5 bulk glassy alloys. Mater. Trans., JIM 2000; 41:675.

238. Tatschl A, Gilbert CJ, Schroeder V, Pippan R, Ritchie RO. Stereophotogrammetric investigation of overload and cyclic fatigue fracture surface morphologies in a Zr–Ti–Ni–Cu–Be bulk metallic glass. J. Mater. Res. 2000; 15:898.

239. Wang GY, Liaw PK, Peter WH, Yang B, Yokoyama Y, Benson ML, Green BA, Kirkham MJ, White SA, Saleh TA, McDaniels RL, Steward RV, Buchanan RA, Liu CT, Brooks CR. Fatigue behavior of bulk-metallic glasses (official). Intermetallics 2004; 12:885.

240. Steif PS, Spaepen F, Hutchinson JW. Strain localization in amorphous metals. Acta Metall. 1982; 30:447.

241. Cheng YQ, Ma E. Intrinsic shear strength of metallic glass. Acta Mater. 2011; 59:1800.

242. Wang GY, Liaw PK, Yokoyama Y, Inoue A, Liu CT. Fatigue behavior of Zr-based bulk-metallic glasses. Mat. Sci. Eng. A 2008; 494:314.

243. Lee CJ, Lai YH, Huang JC, Du XH, Wang L, Nieh TG. Strength variation and cast defect distribution in metallic glasses. Scripta Mater. 2010; 63:105.

244. Greer AL, Cheng YQ, Ma E. Shear bands in metallic glasses. Materials Science and Engineering: R: Reports 2013; 74:71.

245. Wang S, Ye YF, Sun BA, Liu CT, Shi SQ, Yang Y. Softening-induced plastic flow instability and indentation size effect in metallic glass. J. Mech. Phys. Solids 2015; 77:70.

246. Schuh CA, Nieh TG. A nanoindentation study of serrated flow in bulk metallic glasses. Acta Mater. 2003; 51:87.

247. Schuh CA, Hufnagel TC, Ramamurty U. Mechanical behavior of amorphous alloys. Acta Mater. 2007; 55:4067.

248. Li HQ, Li L, Fan C, Choo H, Liaw PK. Nanocrystalline coating enhanced ductility in a Zr-based bulk metallic glass. J. Mater. Res. 2007; 22:508.

249. Xie S, George EP. Hardness and shear band evolution in bulk metallic glasses after plastic deformation and annealing. Acta Mater. 2008; 56:5202.

250. Wang GY, Liaw PK. Bending-fatigue behavior of bulk metallic glasses and their composites. JOM 2010; 62:25.

251. Liu FX. Microstructures and Mechanical Behavior of Multicomponent Metallic-Glass Thin Film. Dissertation (University of Tennessee) 2009.

APPENDICES

APPENDIX I

Table 1. Strength-stiffness ratios of a number of [hkl] grains in the crystalline phase and the metallic-glass (MG) matrix, with an initial yield stress of 150 MPa for the crystalline phase. [186]

Parameters for the crystalline phase

Parameter	Slip system	[200] grains	[220] grains	[211] grains	[310] grains
E (GPa)	-	129	158	158	138
r_{cry}^{hkl} (10^{-3})	[110]<111>	2.85	1.17	1.17	1.67
r_{cry}^{hkl} (10^{-3})	[112]<111>	4.94	2.01	1.22	2.88
r_{cry}^{hkl} (10^{-3})	[123]<111>	7.53	2.06	1.32	3.51
"Hard" – "Soft"		[200] – [310] – [220] / [211]			

Parameters for the MG matrix

Parameter	Value	Parameter	Value	Parameter	Value
r_{MG} (10^{-3})	20.22	E_{MG} (GPa)	89	σ_{MG} (GPa)	1.8

Table 2. Parameters used in the finite element simulations with results matching the lattice strain evolution in the composites, as shown in Figure 32. [186]

Crystal parameters	Value		
C_{11}, C_{12}, C_{44} (GPa)	91.0, 69.5, 31.0		
Slip systems	[110]<111>	[112]<111>	[123]<111>
n	10	6.3	10
τ_0 (GPa)	0.30	0.20	0.50
τ_s (GPa)	0.80	0.35	0.80
h_0 (GPa)	0.0050	0.0050	0.10
q	1.4	1.4	1.4

Parameter	Value	Parameter	Value	Parameter	Value
E_{MG} (GPa)	89	ν_{MG}	0.37	σ_{MG}^{Y} (GPa)	1.45

Table 3. Chemical compositions (in weight percent) of 316L stainless steel, C-2000® Ni-based alloy, 7075-T6 Al-based alloy, Zr-based alloy, and Ti-based alloy substrates. [155]

316L Stainless Steel [220]										
Content	C	Mn	Si	P	S	Cr	Mo	Ni	N	Fe
Min value (wt. %)	-	-	-	-	-	16.0	2.0	10.0	-	bal.
Max value (wt. %)	0.03	2.0	0.75	0.04	0.03	18.0	3.0	14.0	0.1	bal.

C-2000® Ni-based alloy [221]						
Content	Ni	Cr	Mo	Cu	C	Si
Min value (wt. %)	59	23	16	1.6	0.01	0.08
Max value (wt. %)	-	-	-	-	Max	Max

Zr-based alloy ($ZrHf_{4.5}$) [222]			Ti-based alloy (Ti-6Al-4V) [223]			
Content	Zr	Hf	Content	Ti	Al	V
Value (wt. %)	95.5	4.5	Value (wt. %)	90	6	4

Al-based alloy (7075-T6) [224]									
Content	Al	Mg	Cr	Zn	Cu	Ti	Mn	Si	Fe
Min value (wt. %)	87.1	2.1	0.18	5.1	1.2	-	-	-	-
Max value (wt. %)	91.4	2.9	0.28	6.1	2	0.2	0.3	0.4	0.5

Table 4. Ultimate tensile strengths of substrate materials, including 316L stainless steel, C-2000® Ni-based alloy, 7075-T6 Al-based alloy, Zr-based alloy, and Ti-based alloy, as well as Zr-based and Cu-based BMGs. [155]

Alloys	UTS (MPa)	Alloys	UTS (MPa)
316L stainless steel [220]	820	C-2000® Ni-based alloy [221]	752
$ZrHf_{4.5}$ alloy [222]	379	Al-based alloy (7075-T6) [224]	572
Ti-6Al-4V alloy [223]	1,170	$(Cu_{60}Zr_{30}Ti_{10})_{99}Sn_1$ [250]	1,800
$Zr_{55}Cu_{30}Ni_5Al_{10}$ [250]	1,560	-	-

APPENDIX II

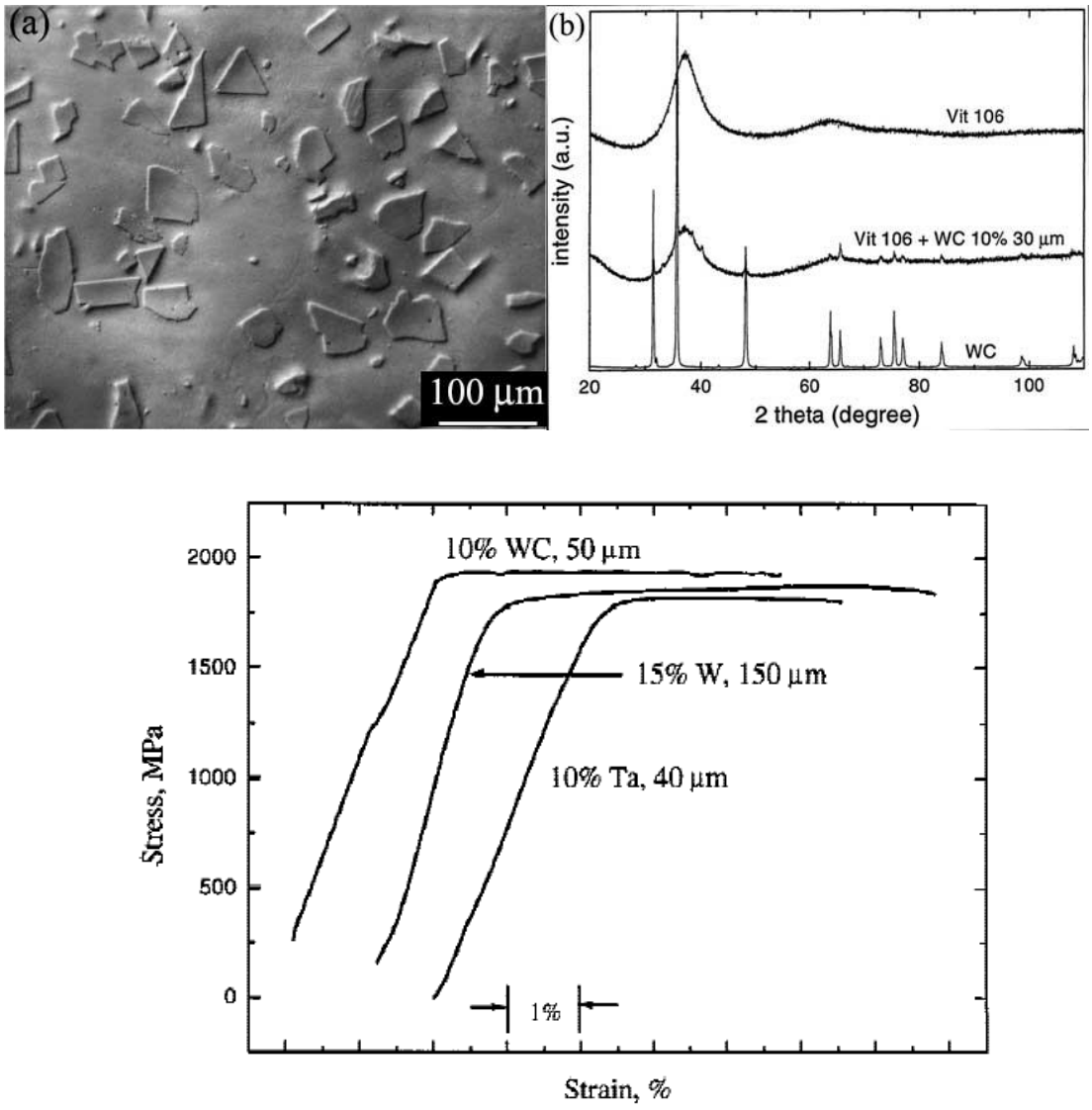

Figure 1. (a) An optical micrograph showing uniformly-distributed WC particles in the V106 matrix; (b) X-ray diffraction patterns of the V106 matrix, the alloy reinforced with 10 vol. % WC, and pure WC particle; and (c) Quasi-static compression stress–strain curves of V106 composites reinforced with Ta, W, and WC particles. [35, 37]

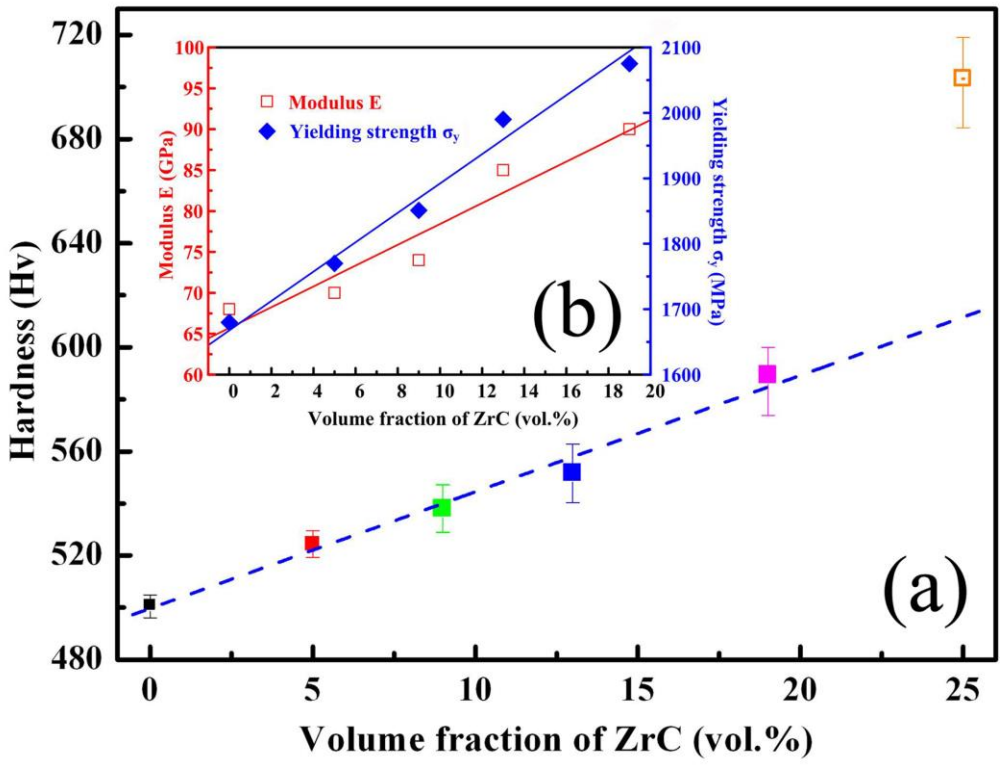

Figure 2. (a) Hardness values of the matrix reinforced by different volumes of the ZrC particles and (b) linear fitness of the modulus, E, and yielding strength, σ_y, with increasing the volume fraction (V_f) of ZrC. [40]

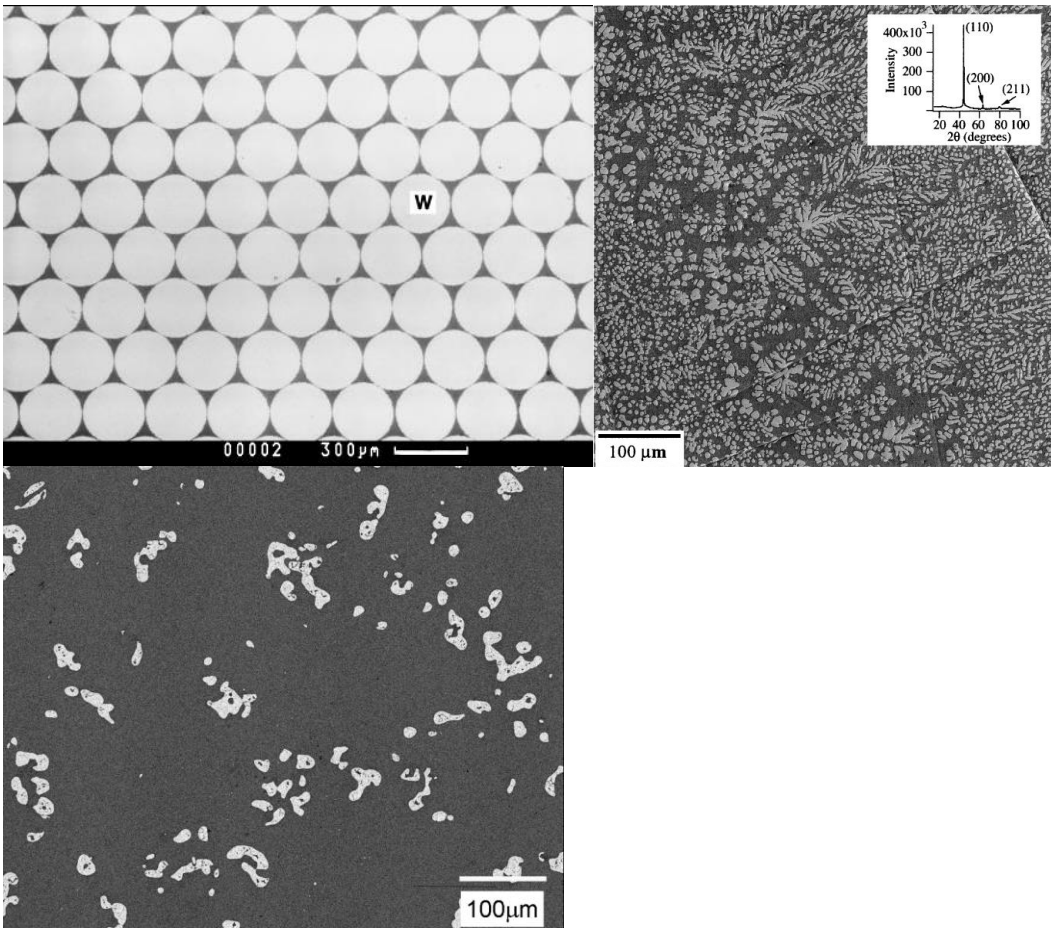

Figure 3. (a) SEM micrograph in the backscatter mode of 80 vol. % W wire / bulk metallic glass matrix composite. The sample is polished and cut normal to the uniaxial reinforcement; [41] (b) SEM backscattered-electron image of *in-situ* composite microstructure (Inset: X-ray diffraction pattern for the $(Zr_{75}Ti_{18.34}Nb_{6.66})_{75}X_{25}$ *in-situ* composite. [67] (c) Backscattered SEM of the *in-situ* composite with a composition of $(Zr_{70}Ni_{10}Cu_{20})_{82}Ta_8Al_{10}$. [91]

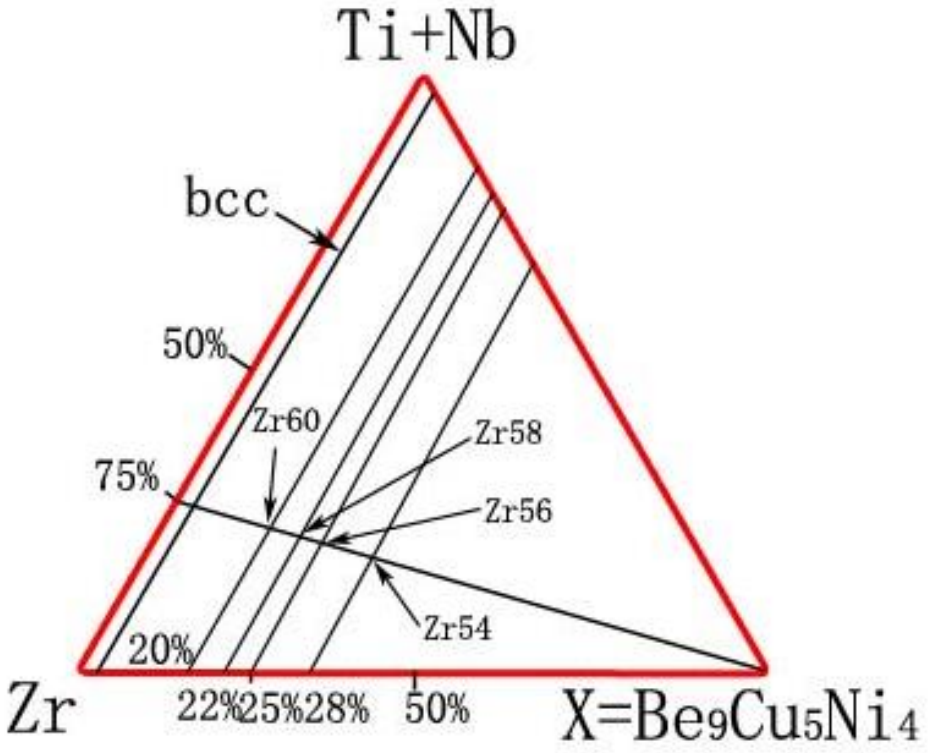

Figure 4. A pseudo ternary phase diagram with apexes of zirconium, (titanium + niobium), and X, where X represents the moiety $Cu_5Ni_4Be_9$. [69]

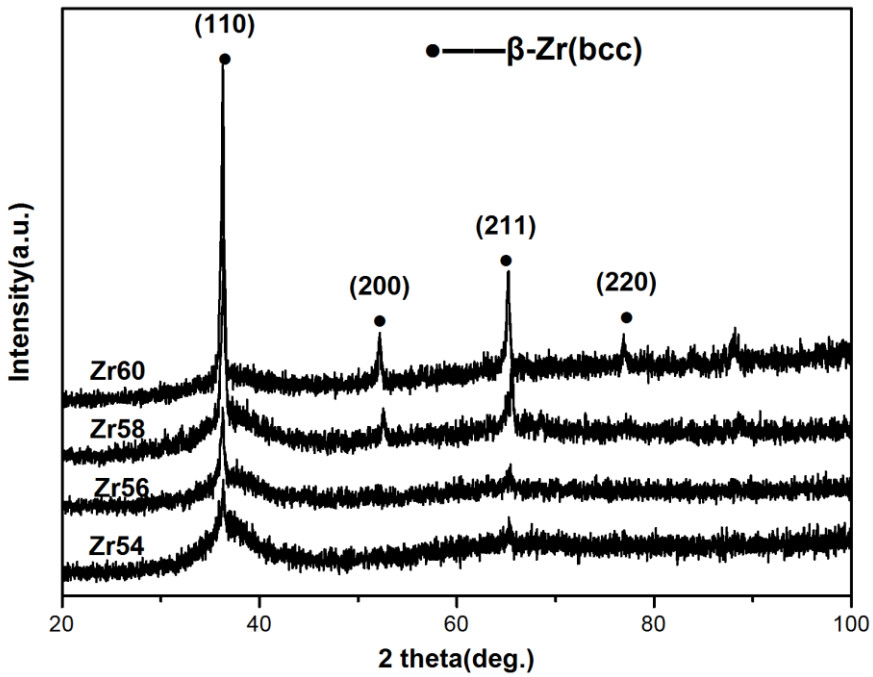

Figure 5. X-ray diffraction patterns of four samples with different compositions (labeled as Zr54, Zr56, Zr58, and Zr60, respectively). [69]

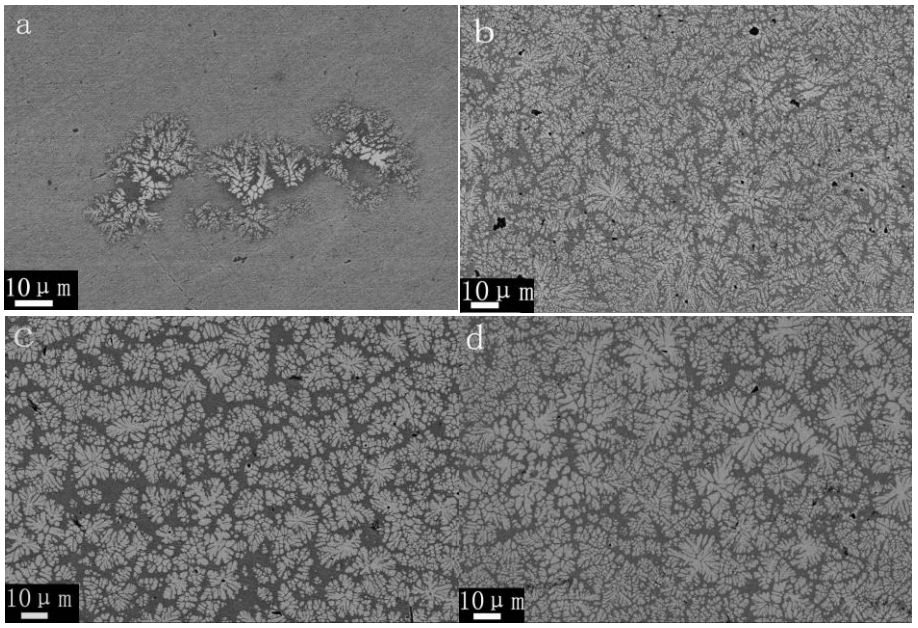

Figure 6. SEM images of the cross sections of the composites with the compositions of: (a) Zr54, (b) Zr56, (c) Zr58, and (d) Zr60. [69]

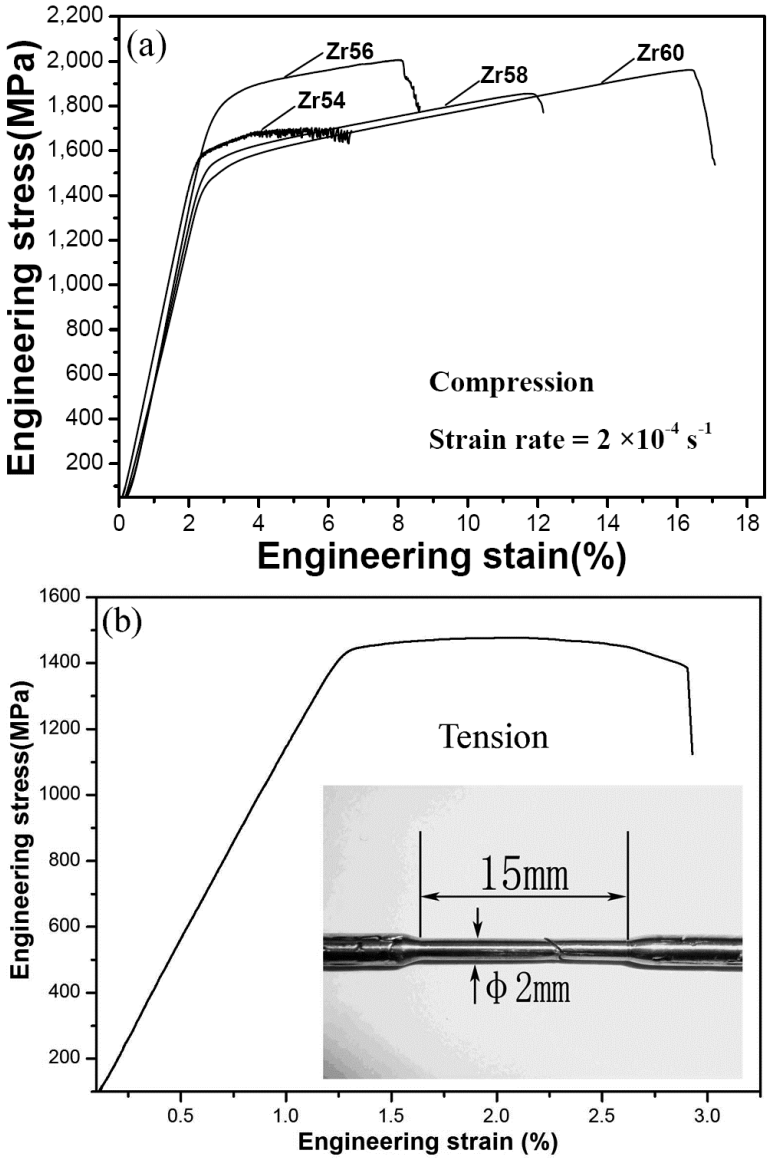

Figure 7. (a) the compressive engineering stress-strain curves of the four composites, [69] and (b) the tensile engineering stress-strain curves of the Zr60 composite. [71]

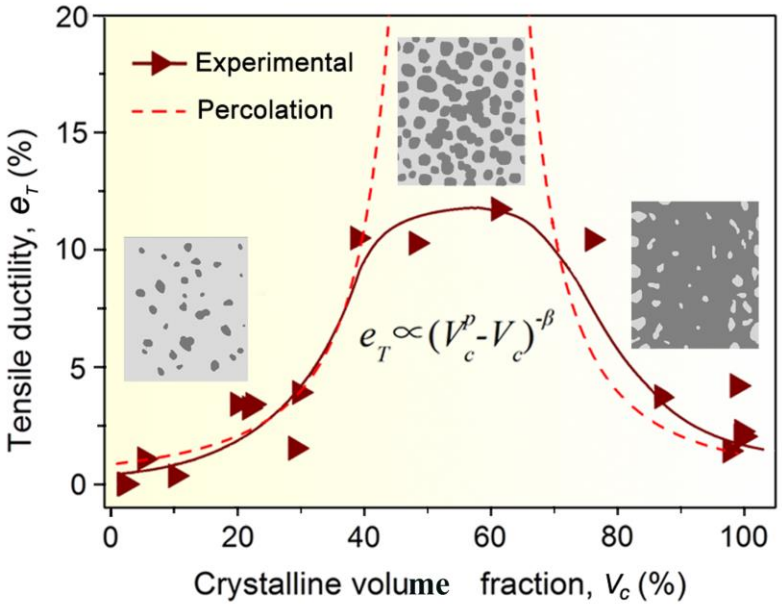

Figure 8. Dependence of tensile ductility on crystalline volume fraction. [97]

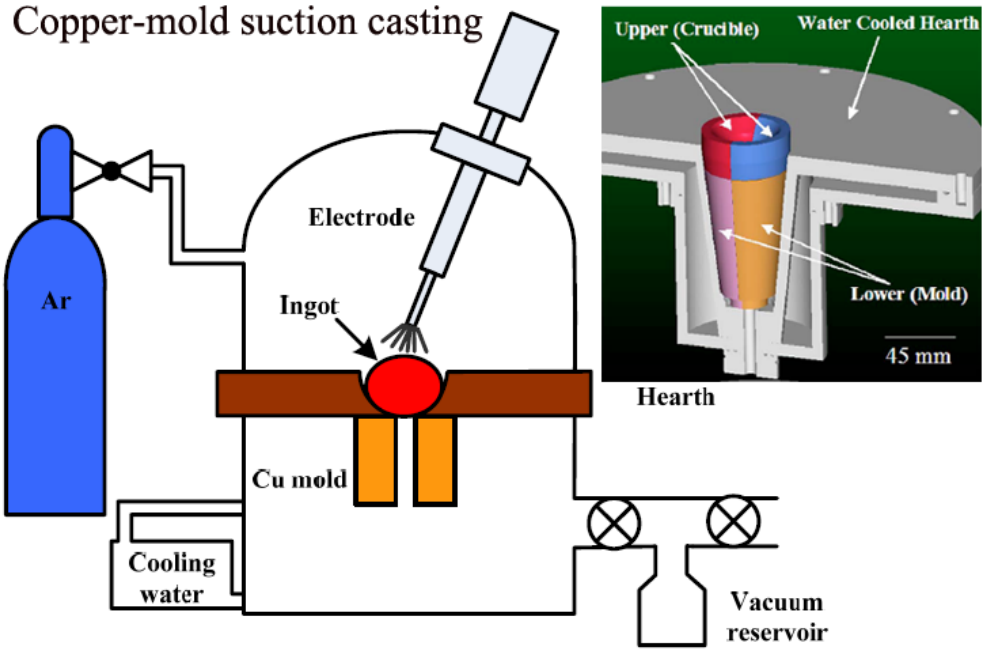

Figure 9. Typical schematic illustration of copper-mold suction casting, and the arc melter at The University of Tennessee shown in the inset. [102]

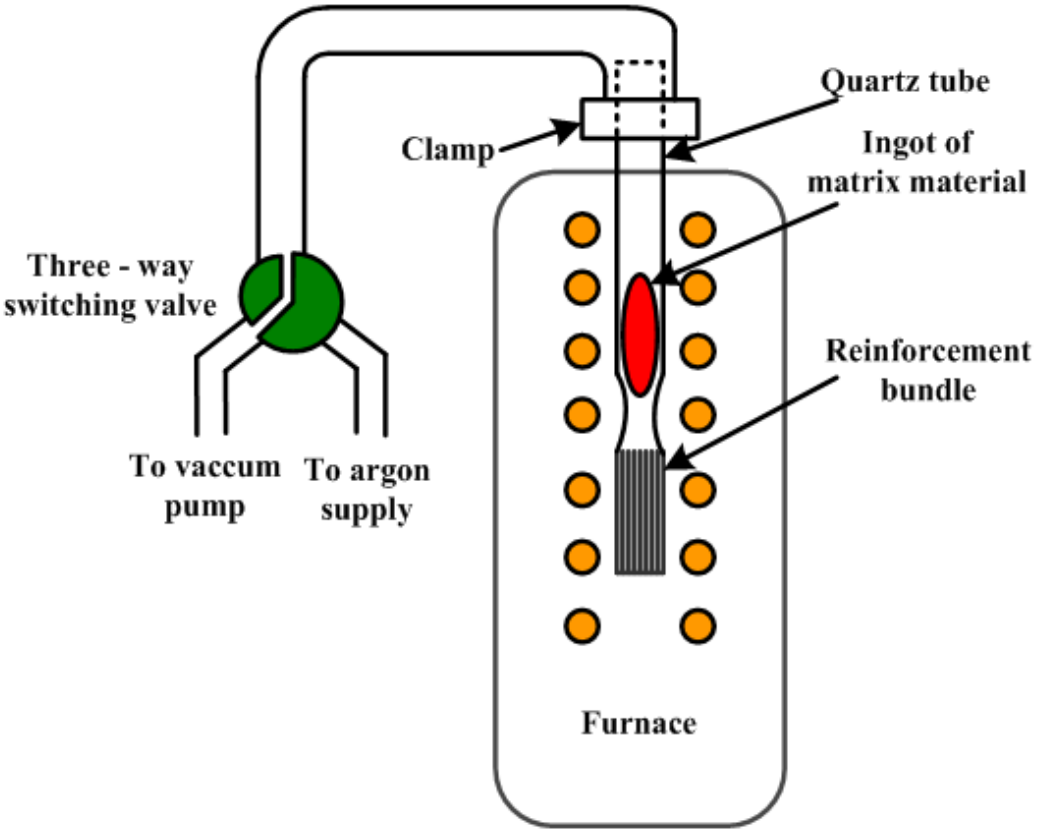

Figure 10. Schematic diagram of the apparatus for casting bulk MGMCs. [35]

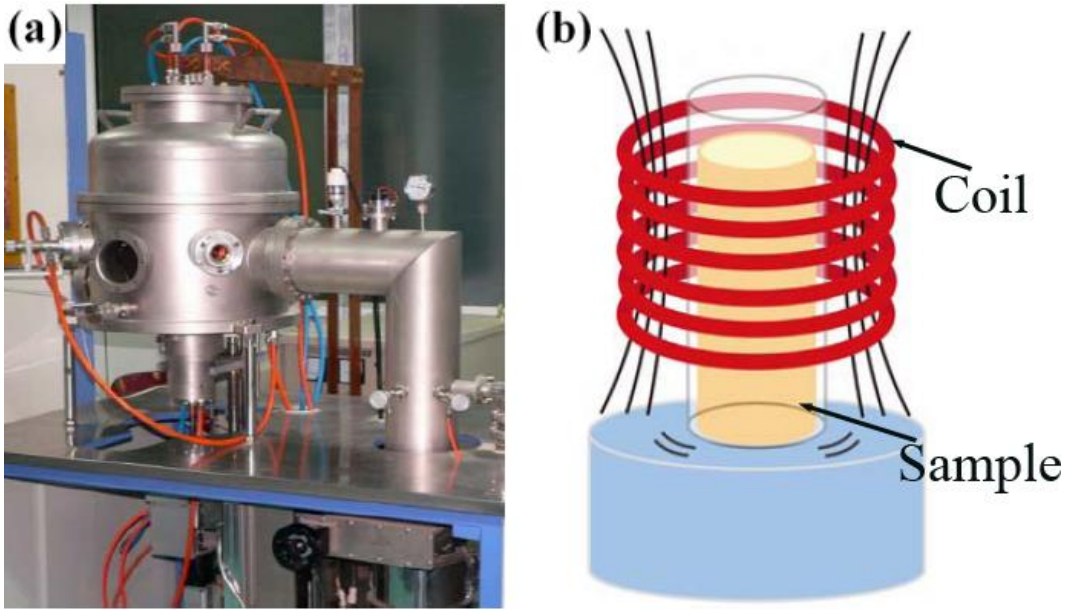

Figure 11. The Bridgman solidification apparatus used by Qiao *et al.* (a), and the corresponding illustration exhibited in (b). [147]

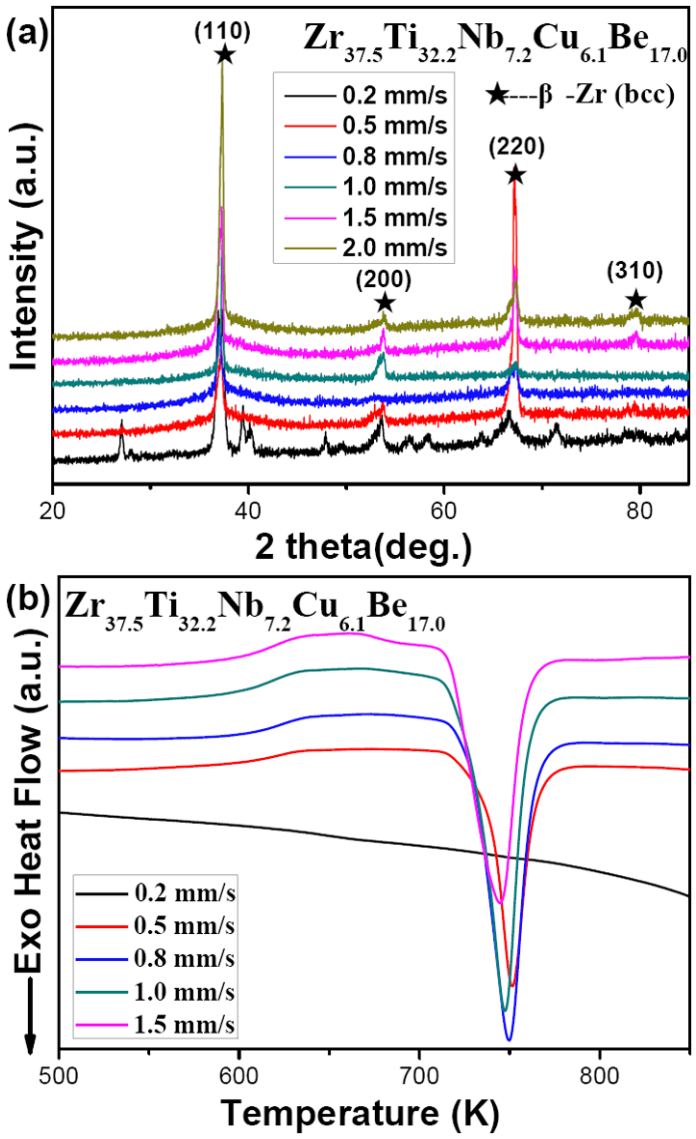

Figure 12. XRD patterns (a) and DSC traces (b) of the composites synthesized with different withdrawal velocities. [53]

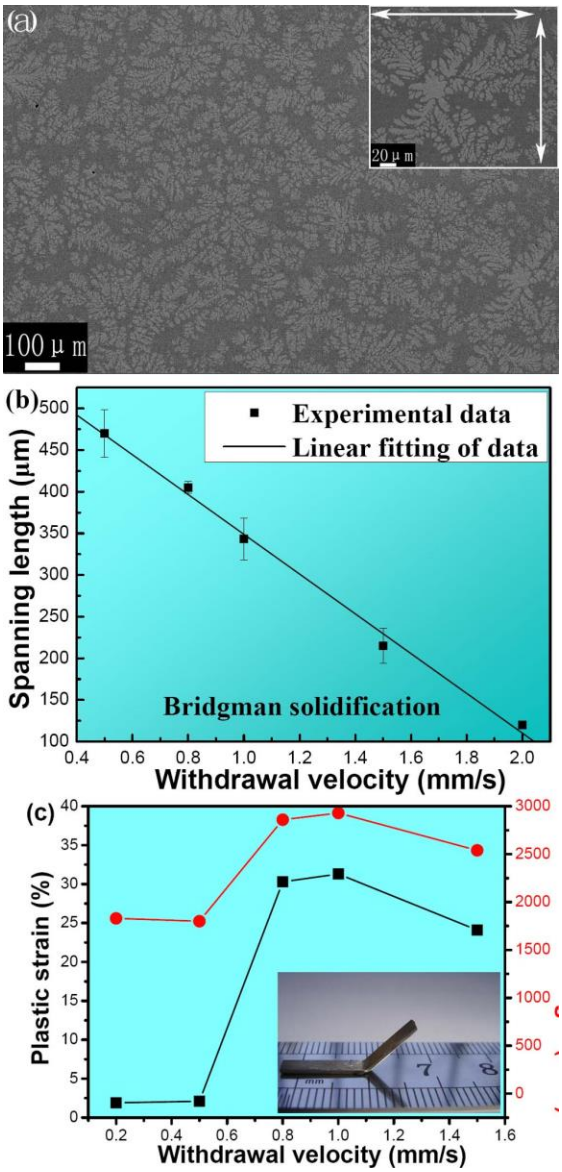

Figure 13. The microstructure of the sample with v = 1.0 mm/s is illustrated in (a), the dependences of spanning lengths of individual dendrite trees on varied withdrawal velocities shown in (b), and the dependences of fracture strengths and plastic strains of the composites developed by the Bridgman solidification on the v (c), the inset in (c) indicating the sample with v = 1.0 mm/s after bending. [29]

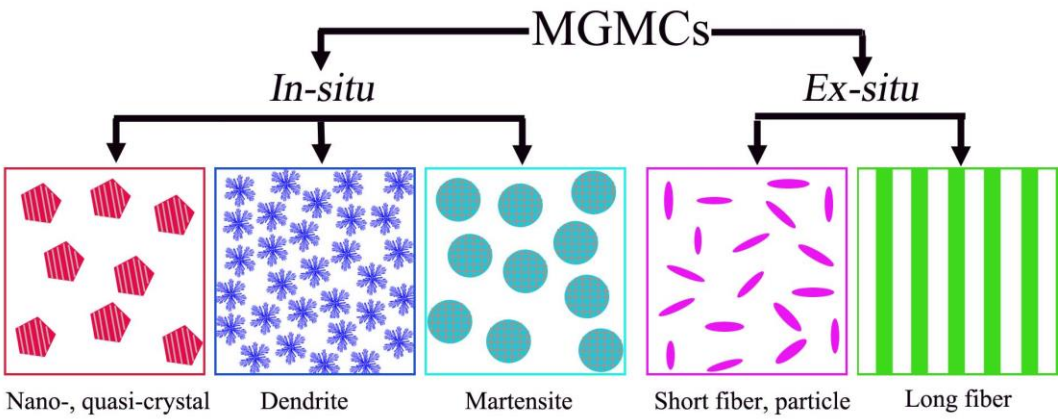

Figure 14. Classification of MGMCs. [147]

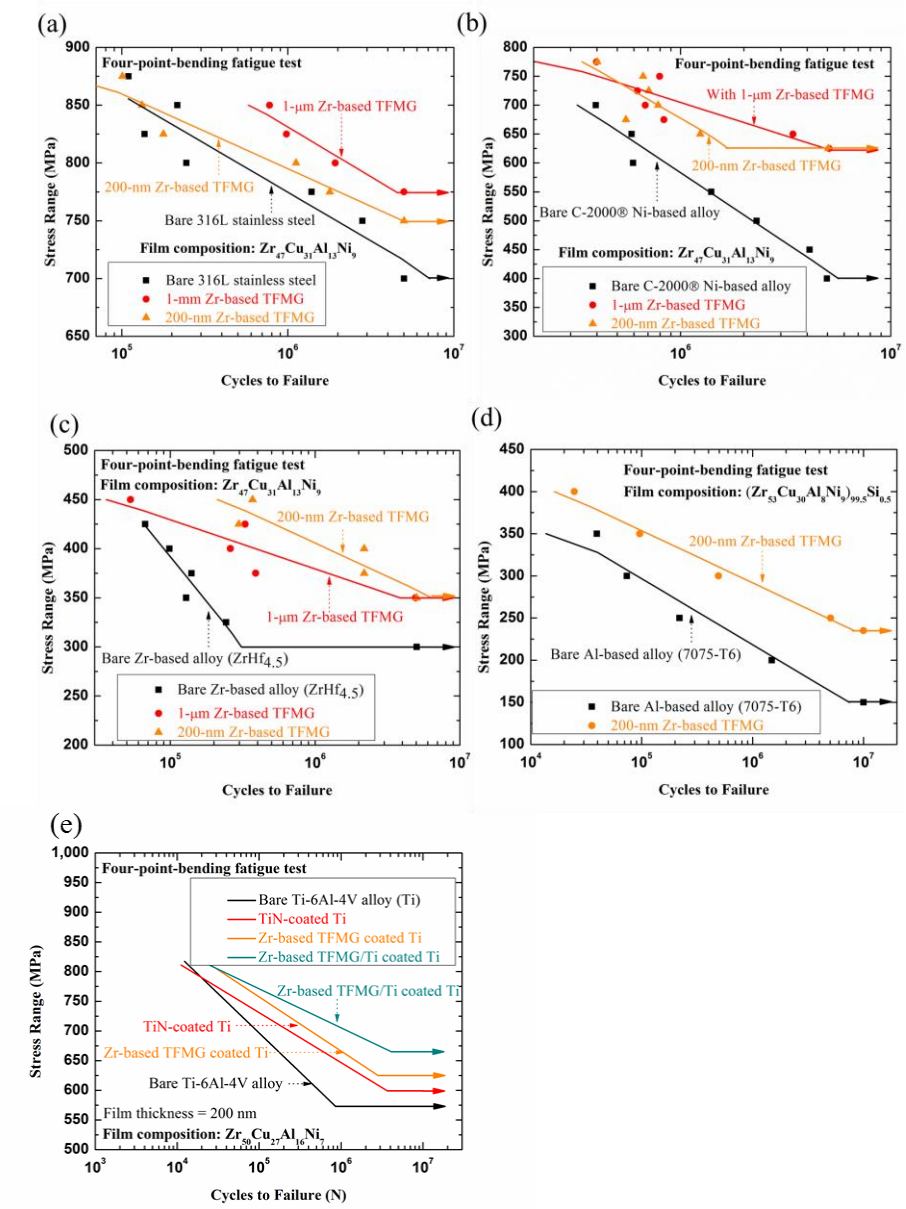

Figure 15. (a) S–N curves of 316L stainless-steel specimens coated with Zr-based metallic-glass films of different thicknesses (200 nm and 1 μm), as well as the bare substrate, under four-point-bending fatigue tests. (b) S–N curves of a Ni-based alloy and specimens coated with Zr-based metallic-glass films of different thicknesses, 200 nm and 1 μm. (c) S–N curves of a Zr-based alloy substrate, as well as coated specimens with Zr-based TFMGs of different thicknesses, 200 nm and 1 μm.(d) S–N curves of 7075-T6 aluminum alloys with and without ZrCuNiAlSi TFMG coatings. (e) S–N curves for Ti–6Al–4V alloy substrates coated with TiN, TFMG ($Zr_{50}Cu_{27}Al_{16}Ni_7$, at.%), and TFMG/Ti. (Redrawn from [152, 156, 157, 251])

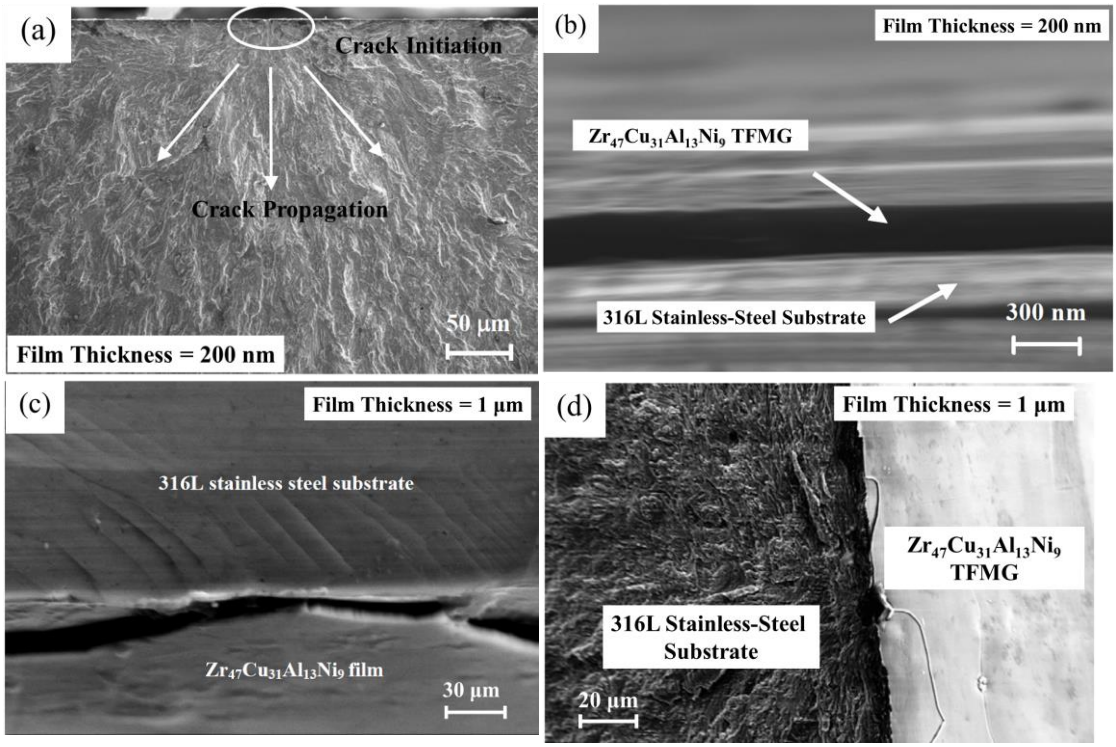

Figure 16. SEM fractographs of failed 316L stainless-steel specimens coated with a $Zr_{47}Al_{13}Cu_{31}Ni_9$ TFMG of different thicknesses: (a) 200-nm-thick and (b) 1-µm-thick; (c) good adhesion between the 1-µm-thick film and substrate is shown at the crack-initiation site; and (d) blockage of the substrate-slip deformation by the 1-µm-thick thin film (Reproduced with permission from [156]).

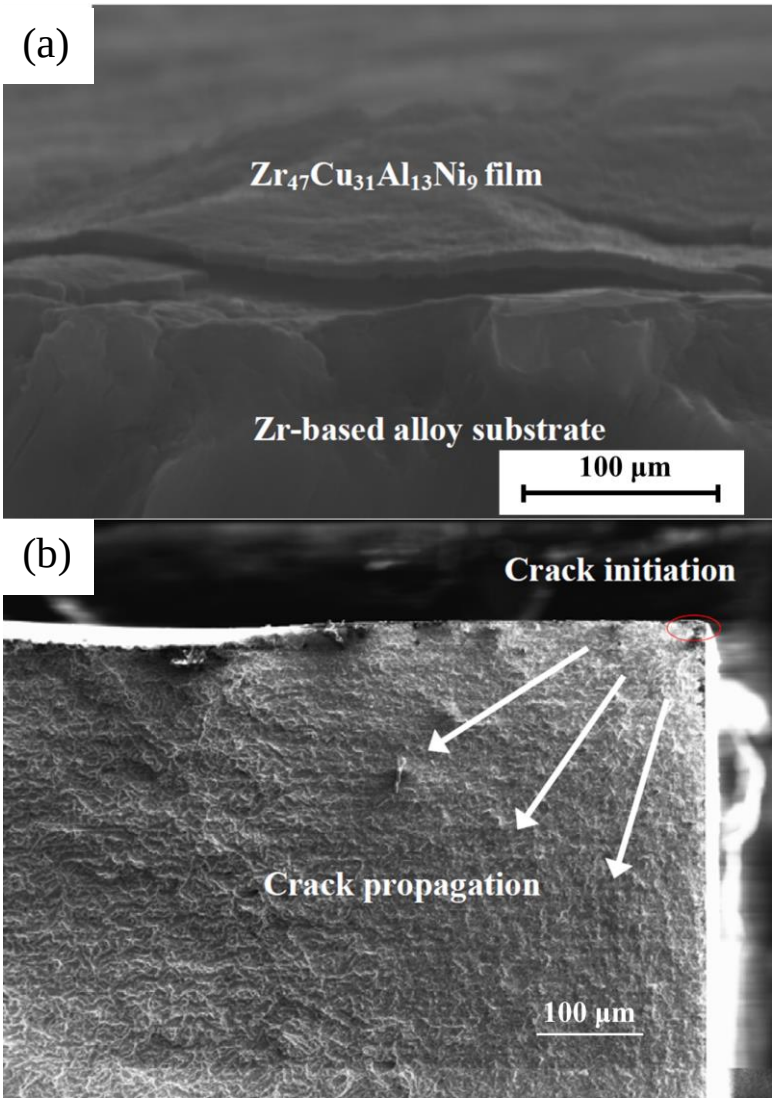

Figure 17. SEM fractographs of (a) the interface between the substrate and film, illustrating partial delamination of the Zr-based film due to severe slip deformation of the substrate, and (b) the fracture surface of the TFMG-coated Zr-based alloy after a four-point bending fatigue test [251].

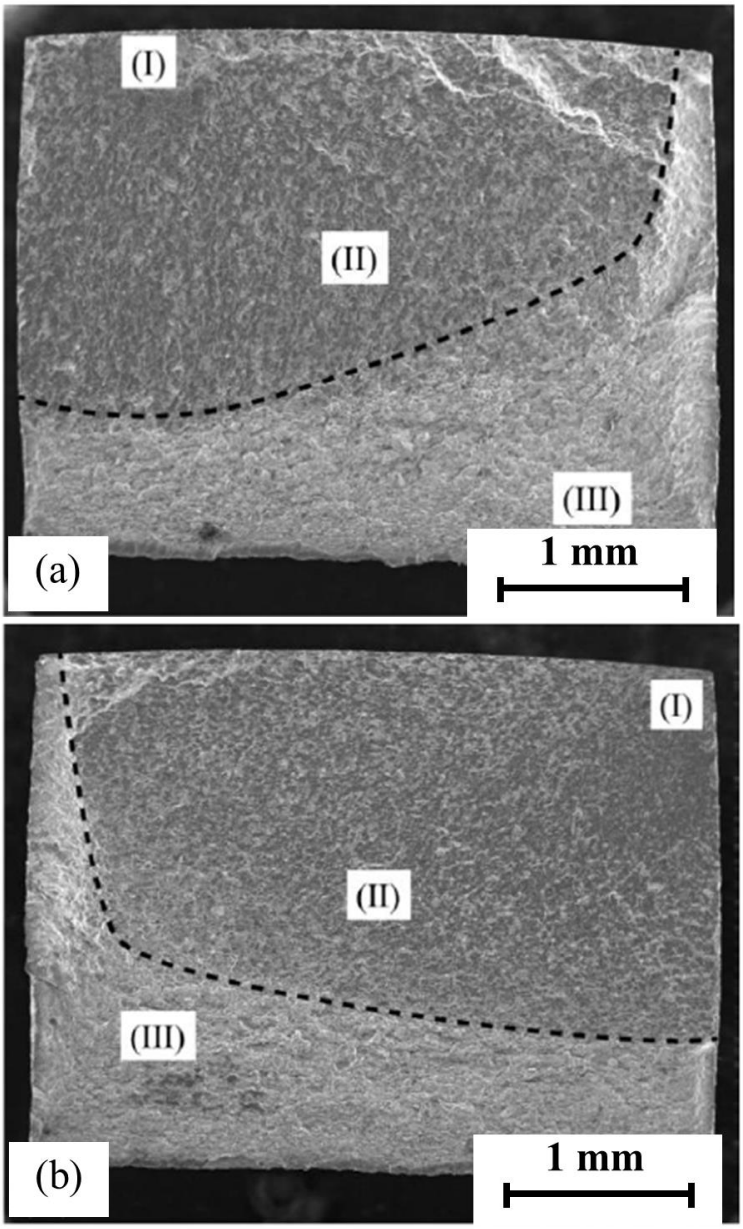

Figure 18. SEM fractographs of (a) uncoated and (b) TFMG-coated 7075-T6 Al alloy specimens fractured at σmax. = 300 and 350 MPa, respectively, under four-point-bending fatigue tests. (I), (II), and (III) on images (a) and (b) represent crack-initiation, crack propagation, and final-fast-fracture regions, respectively [152].

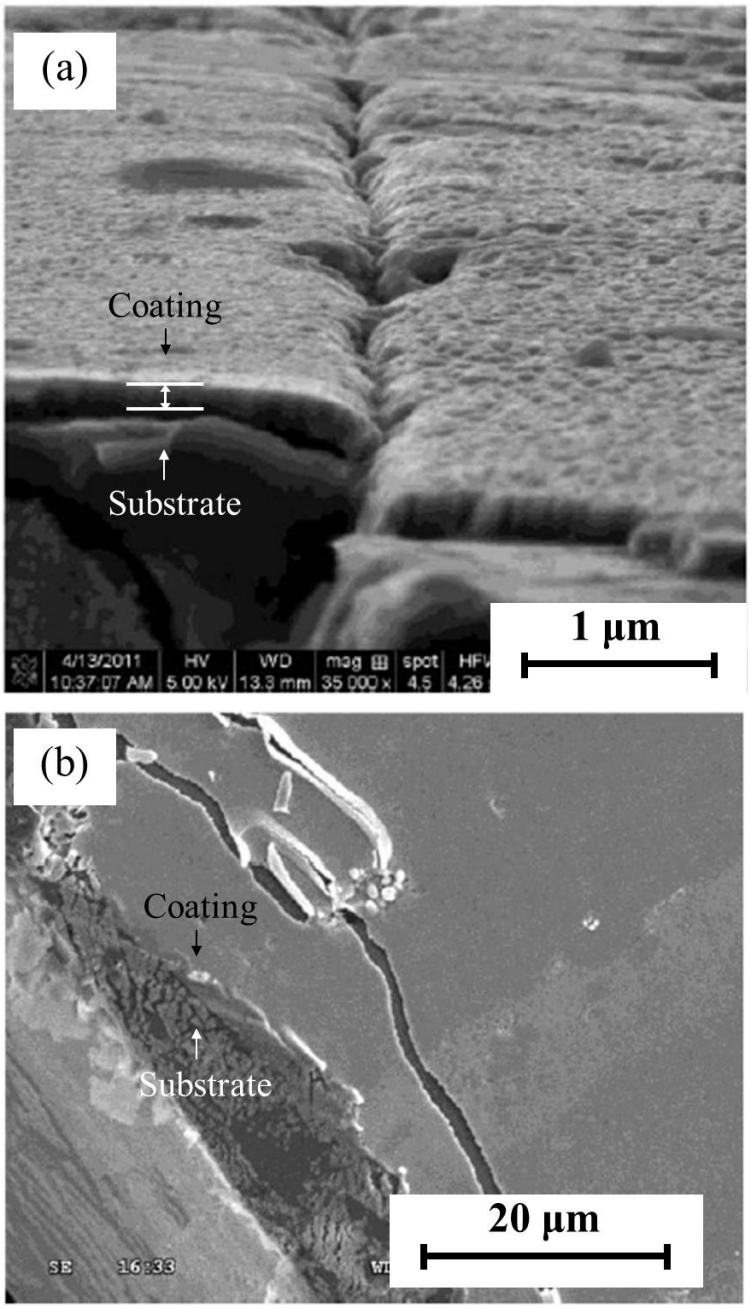

Figure 19. SEM fractographs of a 7075-T6 Al alloy specimen coated with the Zr-based TFMG and fractured at σmax. = 350 MPa under four-point-bending fatigue tests in two views: (a) top-view image and (b) enlarged tilt-view image of the tension surface [152].

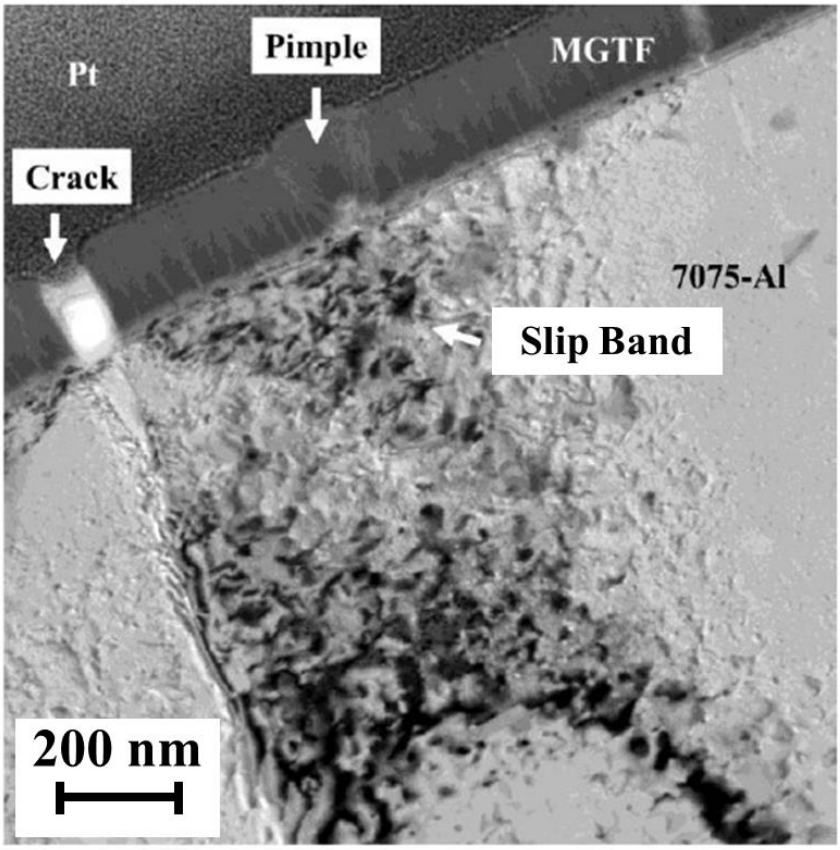

Figure 20. Cross-sectional TEM micrograph obtained from an Al-alloy-substrate specimen coated with a Zr-based TFMG after fatigue tests at σmax. = 350 MPa; the arrows indicate slip bands in the Al-alloy substrate, the offset, and cracking regions in the Zr-based TFMG [152].

Figure 21. TEM cross-sectional fractographs of a coated Ti–6Al–4V substrate with σmax. = 675 MPa, (a) before load, (b–d) interrupted after 5 × 105, 5 × 106, and 6.4 × 106 fatigue cycles, respectively. (e–h) corresponding AFM morphology images with the values of rms surface roughness. [158]

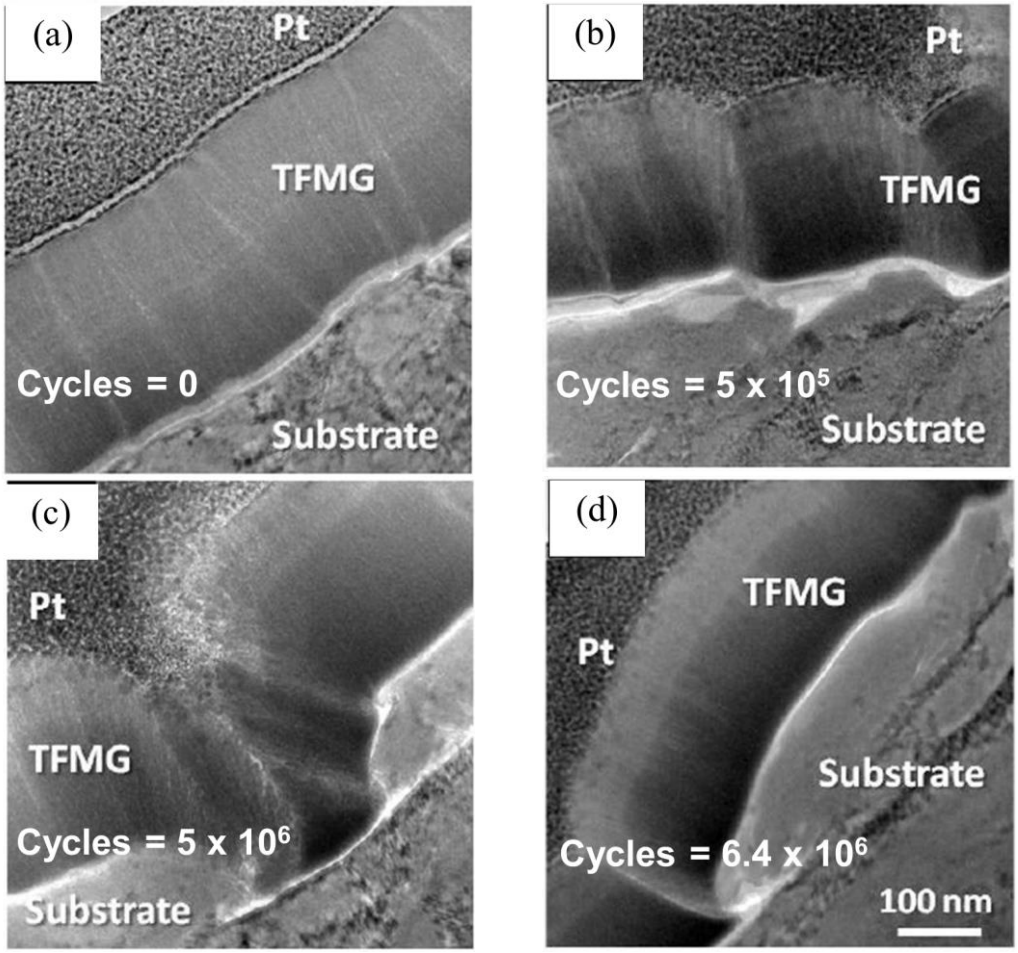

Figure 21 continued

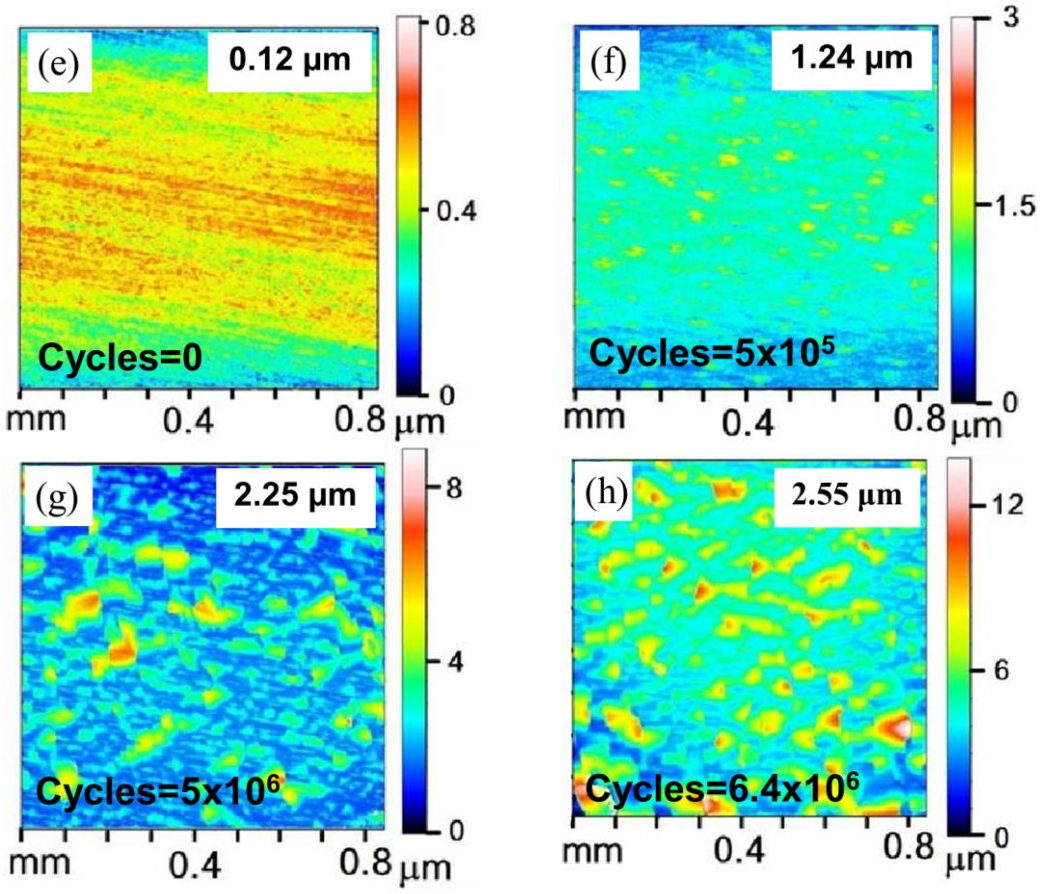

Figure 21 continued

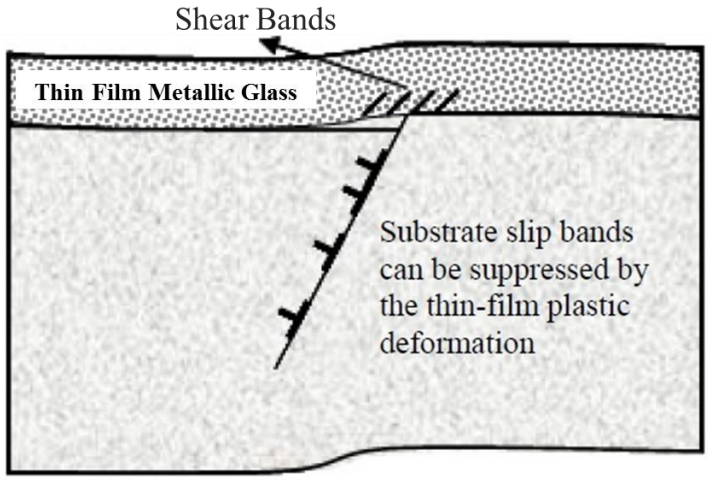

Figure 22. A proposed mechanism for fatigue-crack-initiation in the film/substrate system, showing that substrate dislocation pileups are suppressed by the high ductility and strength of the amorphous film [156, 159].

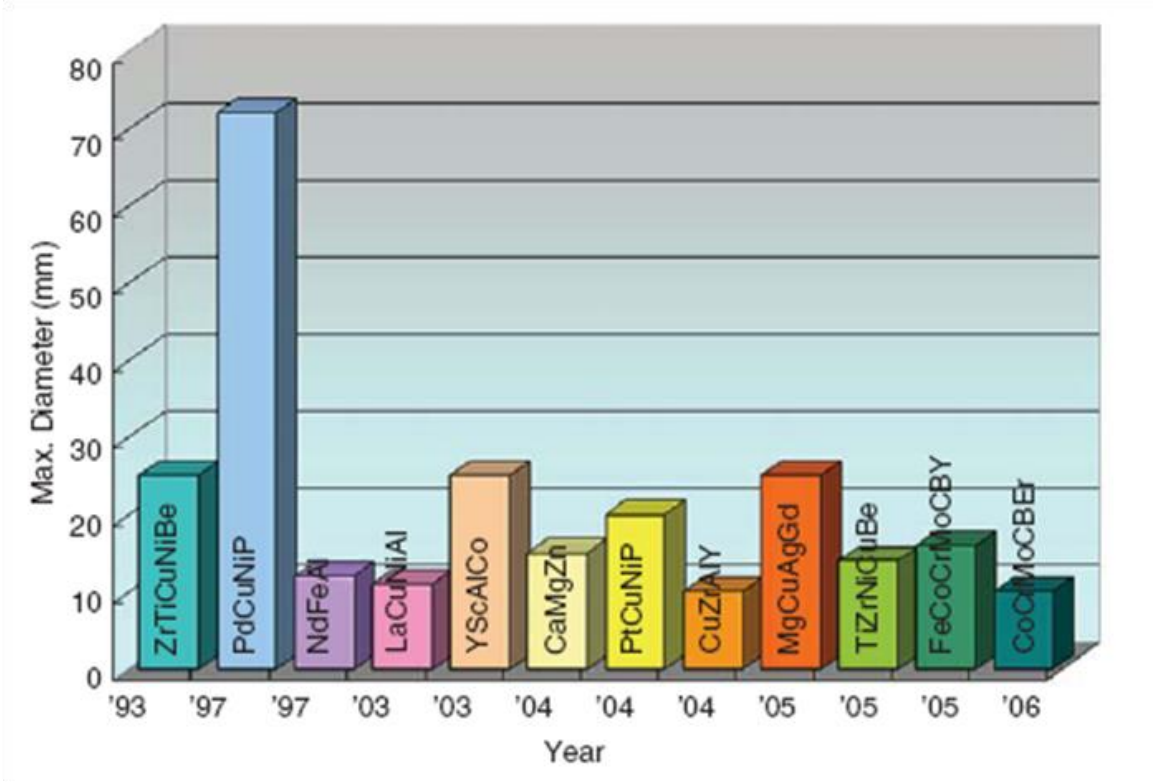

Figure 23. Representative reported BMG alloys. [9]

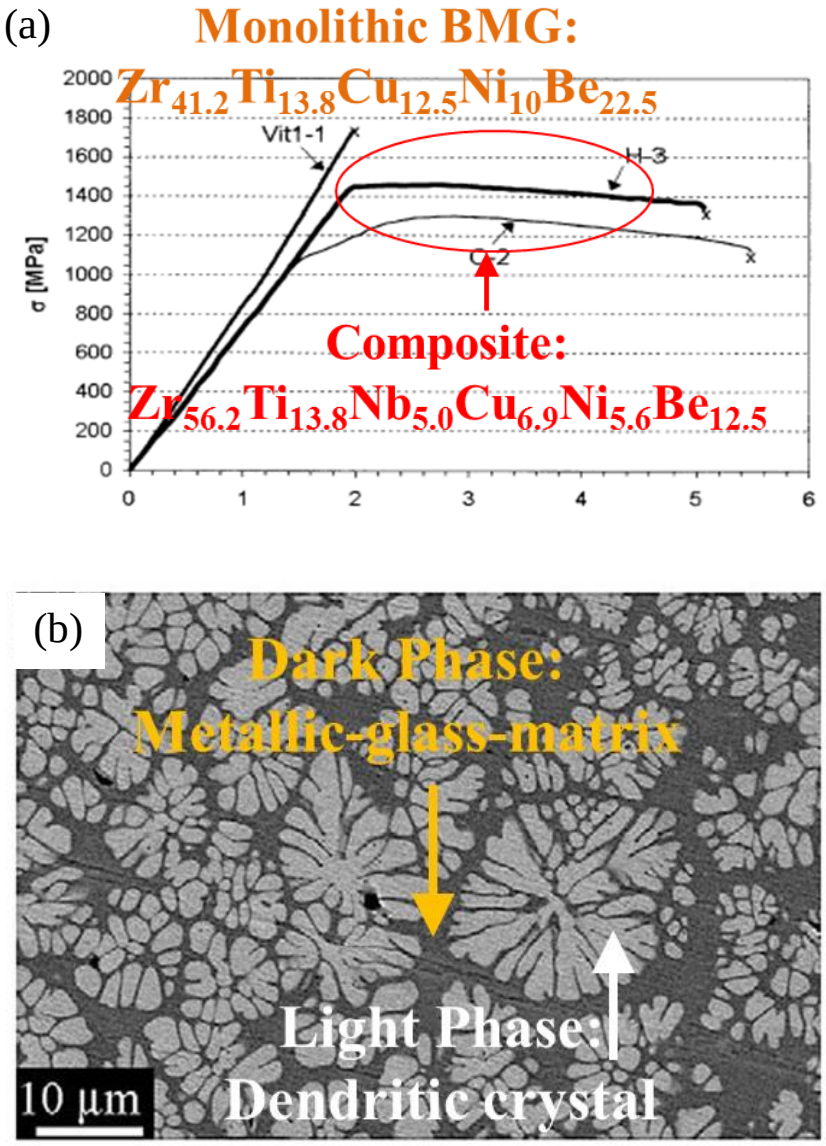

Figure 24. (a) Engineering stress vs. strain curves of monolithic BMG and MGMCs; (b) SEM images of composites. [30, 70]

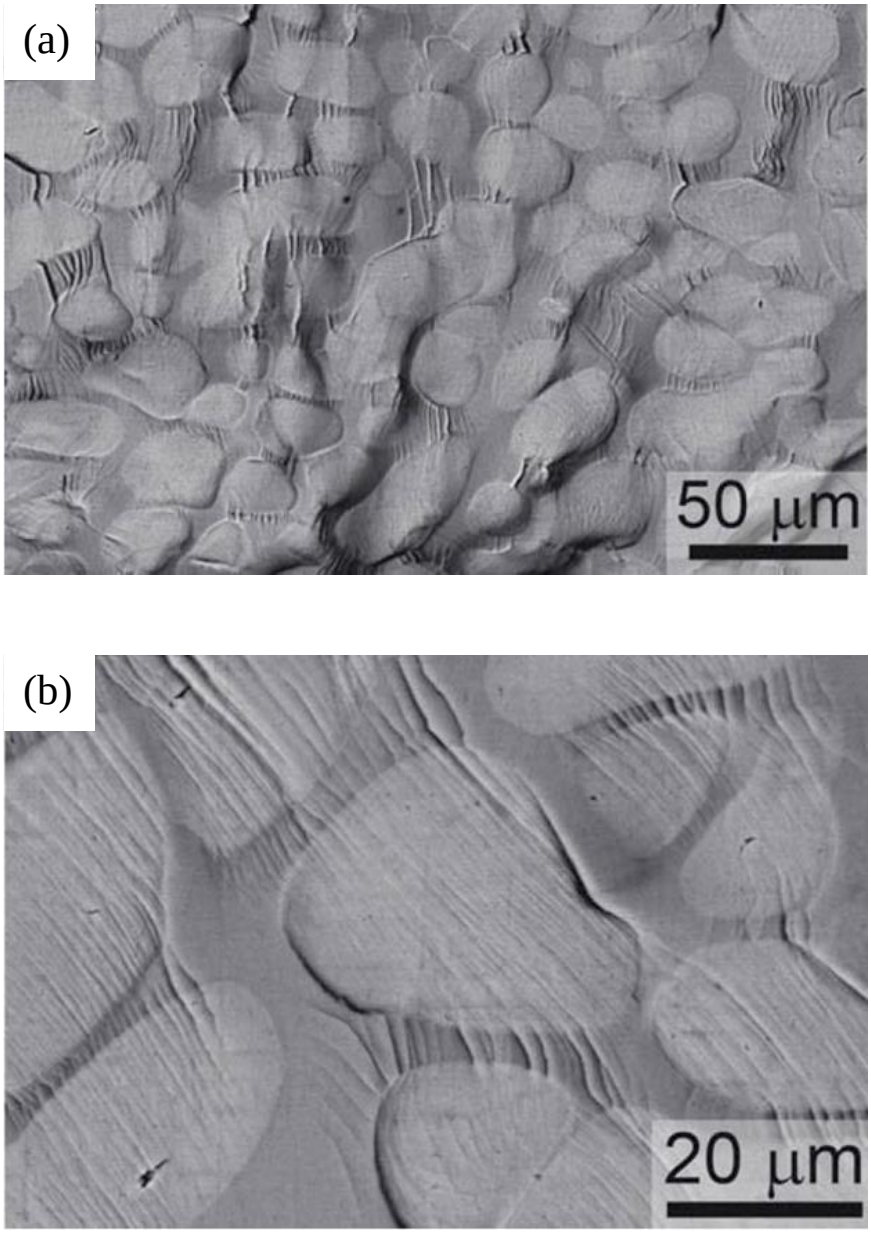

Figure 25. (a) Deformation in composites occuring through the development of highly-organized patterns of regularly-spaced shear bands distributed uniformly along the crack path; (b) Microcracks in composites are nucleated along the shear bands or at the matrix/dendrite interface. [169]

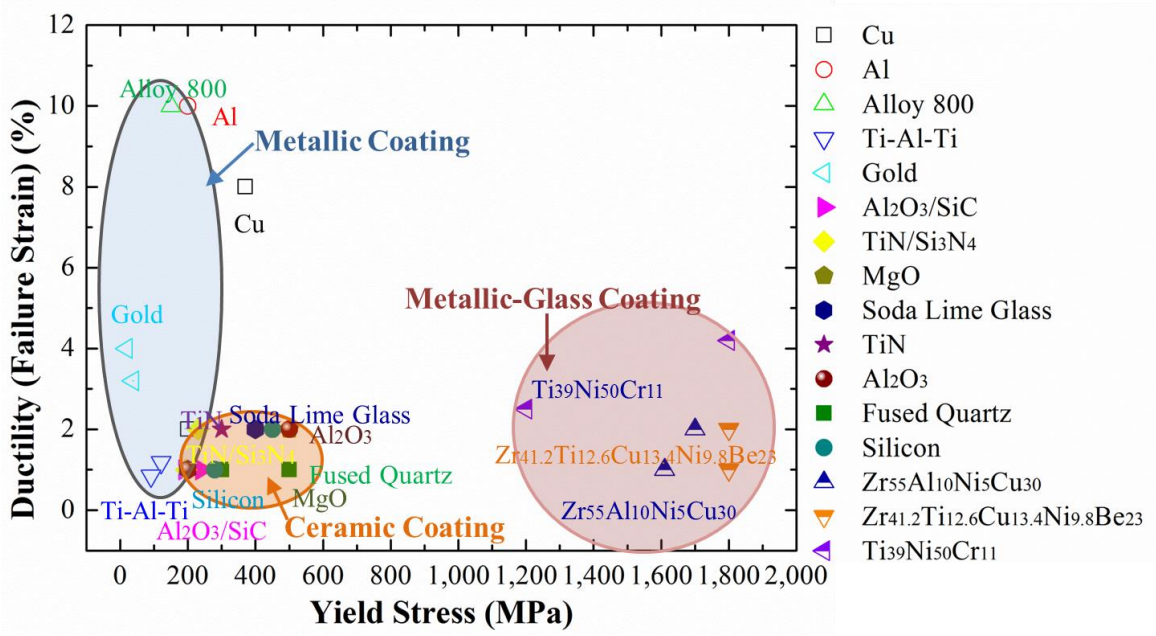

Figure 26. A review of the ductility and yield strength of different kinds of coatings, including TFMGs, metallic coatings, and ceramic coatings applied to improve mechanical properties of substrate materials. [155]

Figure 27. (a) Scanning electron microscope image of the dendritic crystalline phase (β) in the metallic glass matrix with the composite composition of $Zr_{58.5}Ti_{14.3}Nb_{5.2}Cu_{6.1}Ni_{4.9}Be_{11.0}$ (at.%) and the crystalline phase volume percentage of ~ 55%. (b) Schematic illustration of the in situ synchrotron X-ray diffraction experiment on the compression sample. (c) X-ray diffraction pattern of the as-cast specimen before deformation. (d) Line profiles for the specimens before deformation and at an applied stress of ~ 1,500 MPa [186].

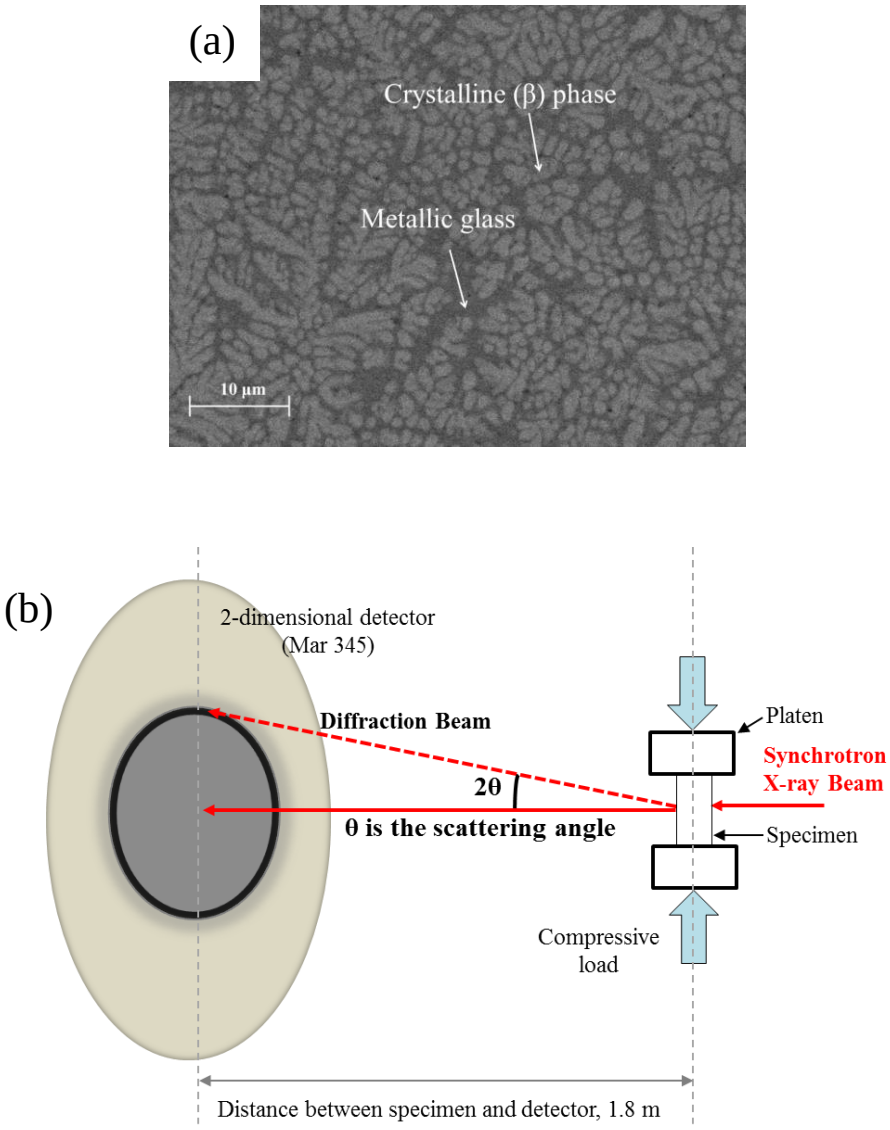

Figure 27 continued

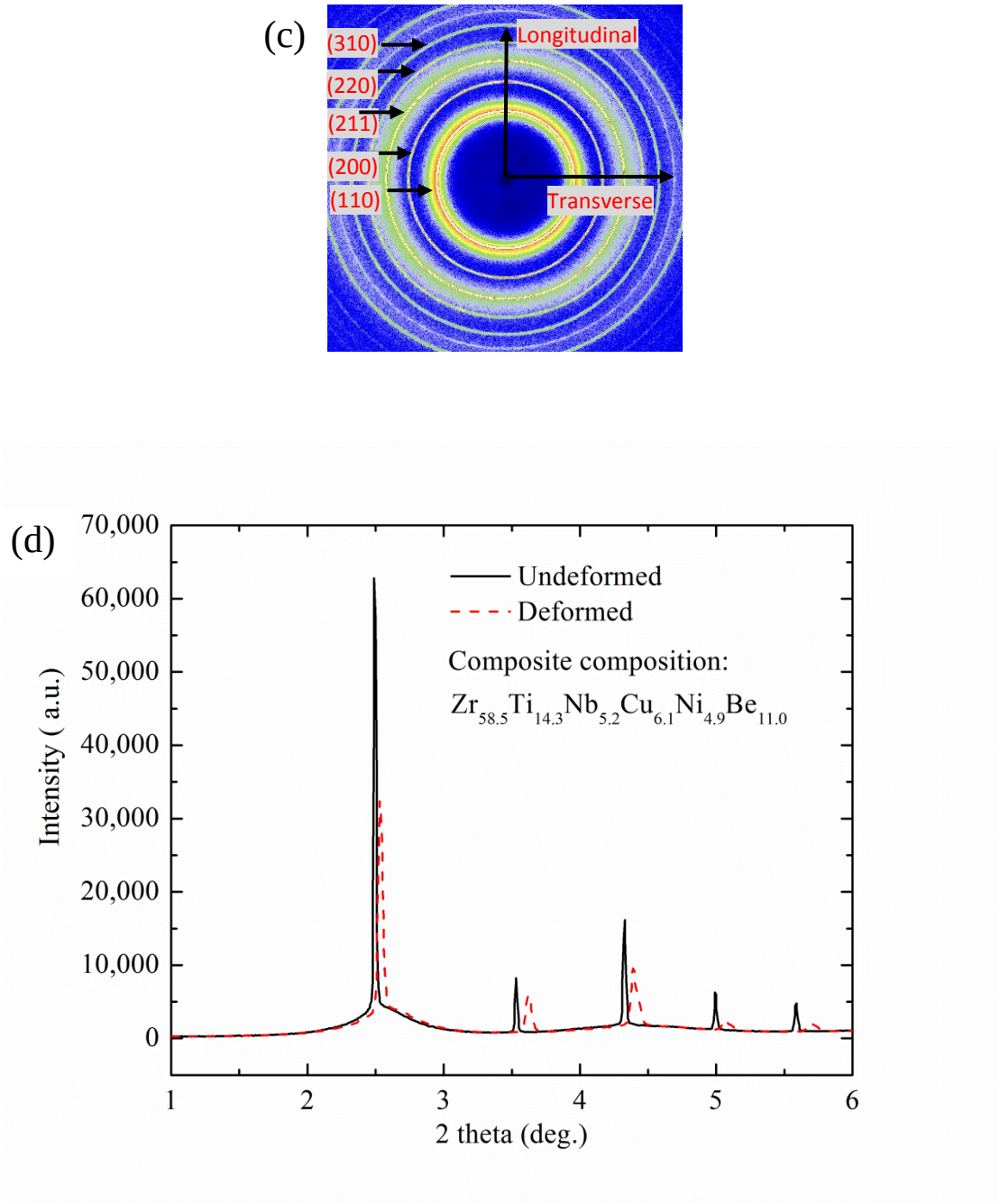

Figure 27 continued

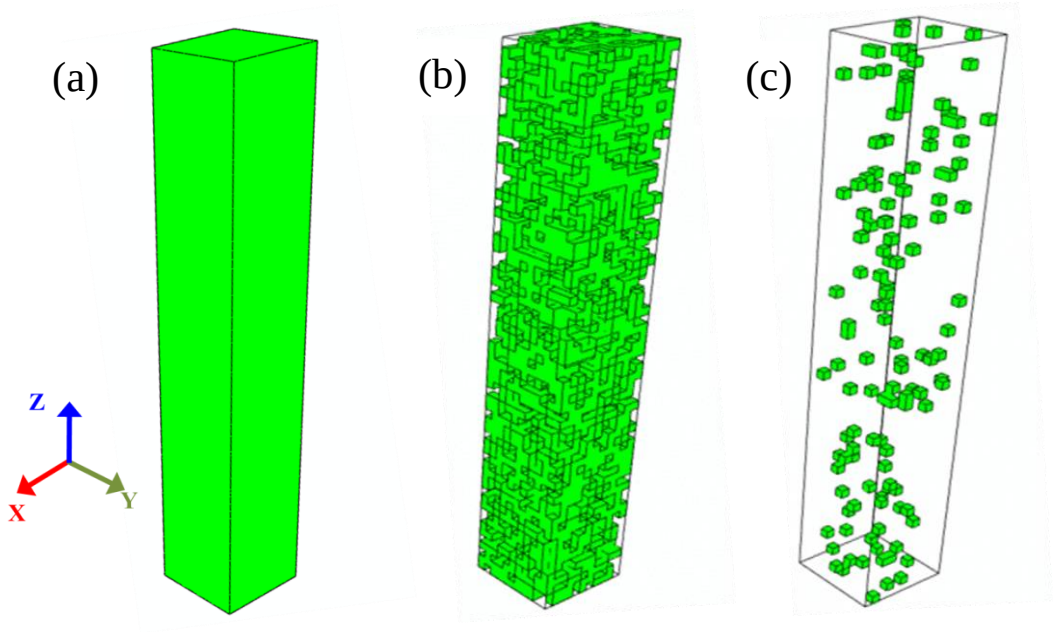

Figure 28. (a) The finite element simulation is conducted on a compression specimen with cubic elements in ABAQUS model. (b) and (c) display all the crystalline grains and the [310] grains, respectively. [186]

Figure 29. (a) The macroscopic compressive engineering stress - strain curve shows considerable plastic deformation. (b) A representative stress - lattice strain curve can be divided into 3 stages. This example is particularly for grains with their <310> directions parallel to the loading direction. [186]

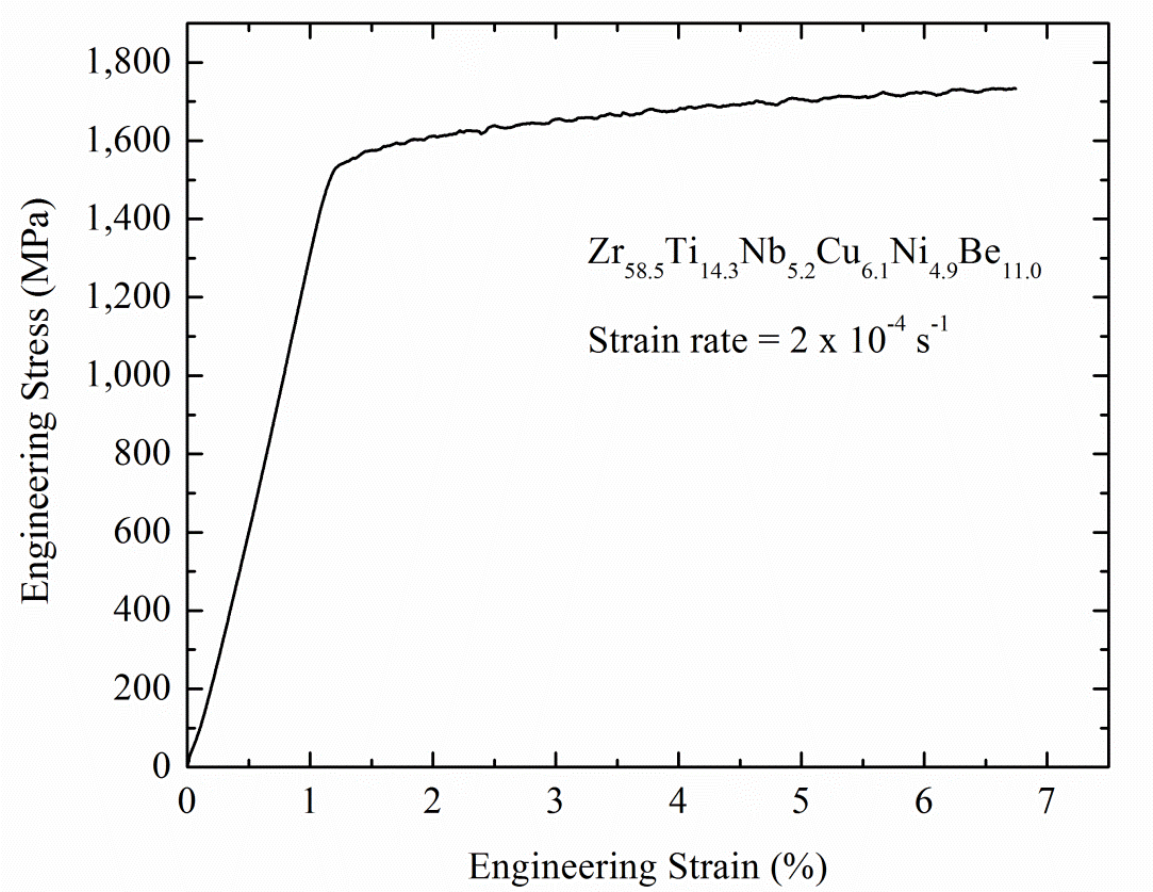

(a)

Figure 29 continued

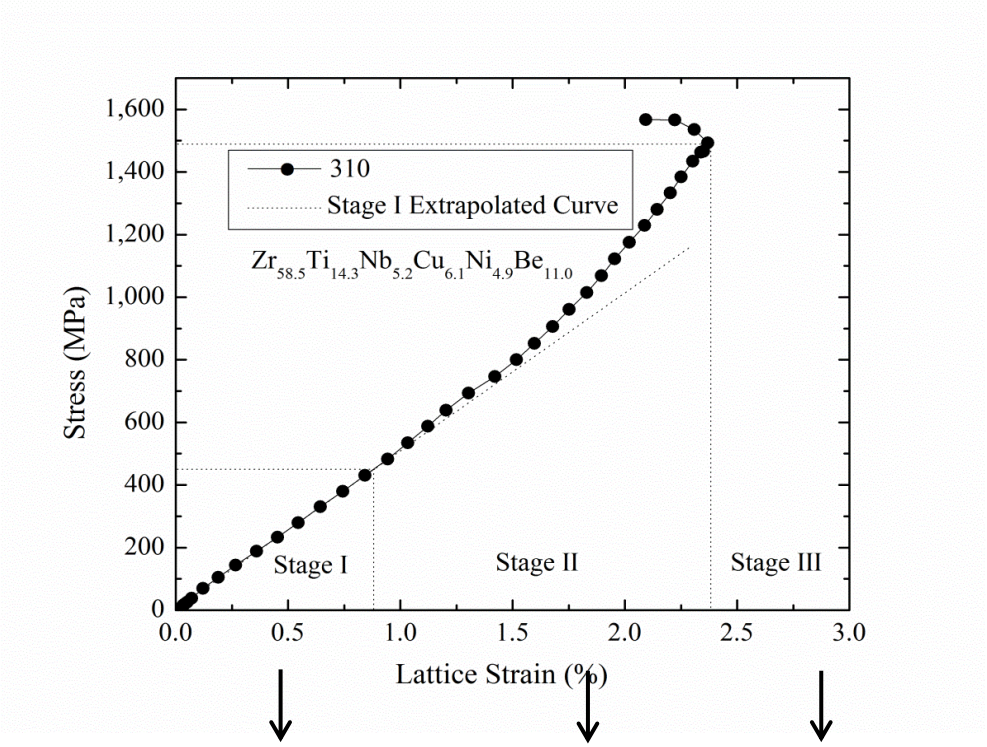

Elastic-elastic stage, in which both the MG matrix and crystalline inclusion deform elastically.	***Elastic-plastic*** stage, in which the MG matrix deforms elastically and the crystalline phase yields around 450 MPa.	***Plastic-plastic*** stage, in which both phases deform plastically, and the lattice strain evolution makes a "turnover".

(b)

Figure 29 continued

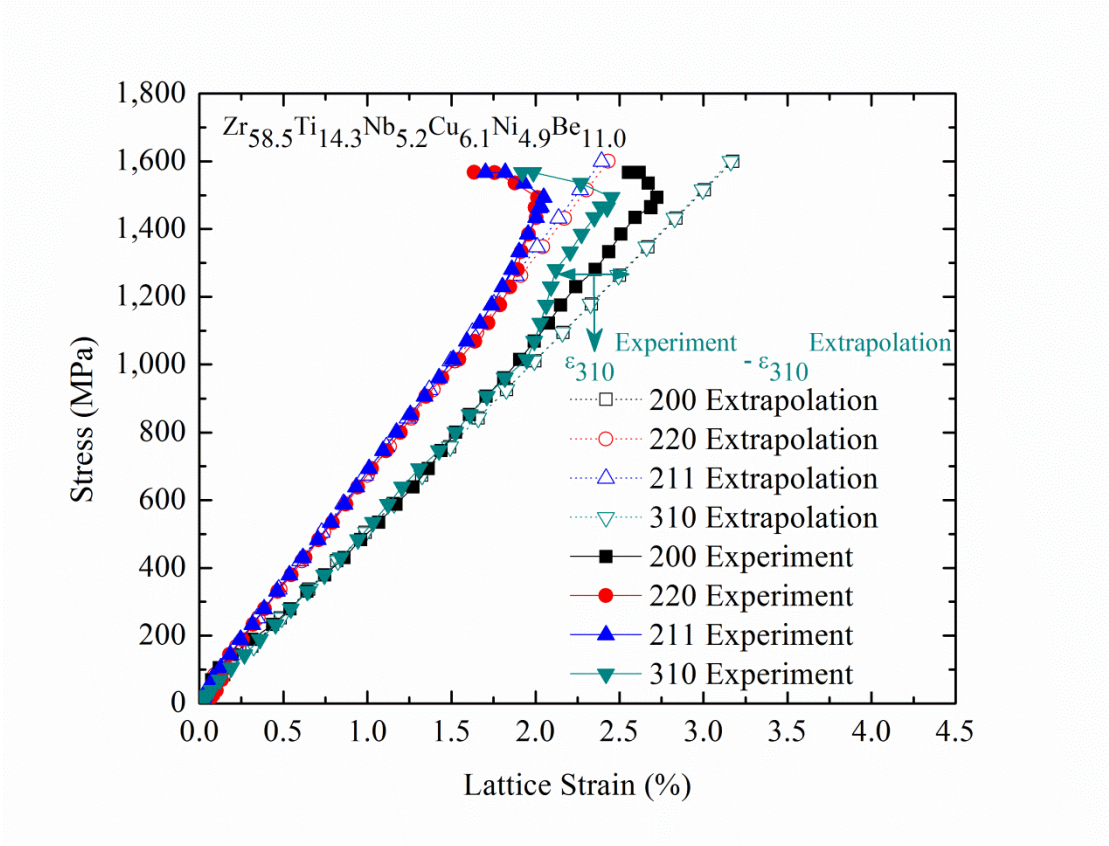

Figure 30. Stress versus lattice strain curves from the X-ray diffraction with the extrapolated lines from the elastic stage of each curve. Four grain families, [200], [211], [220], and [310], have been measured. [186]

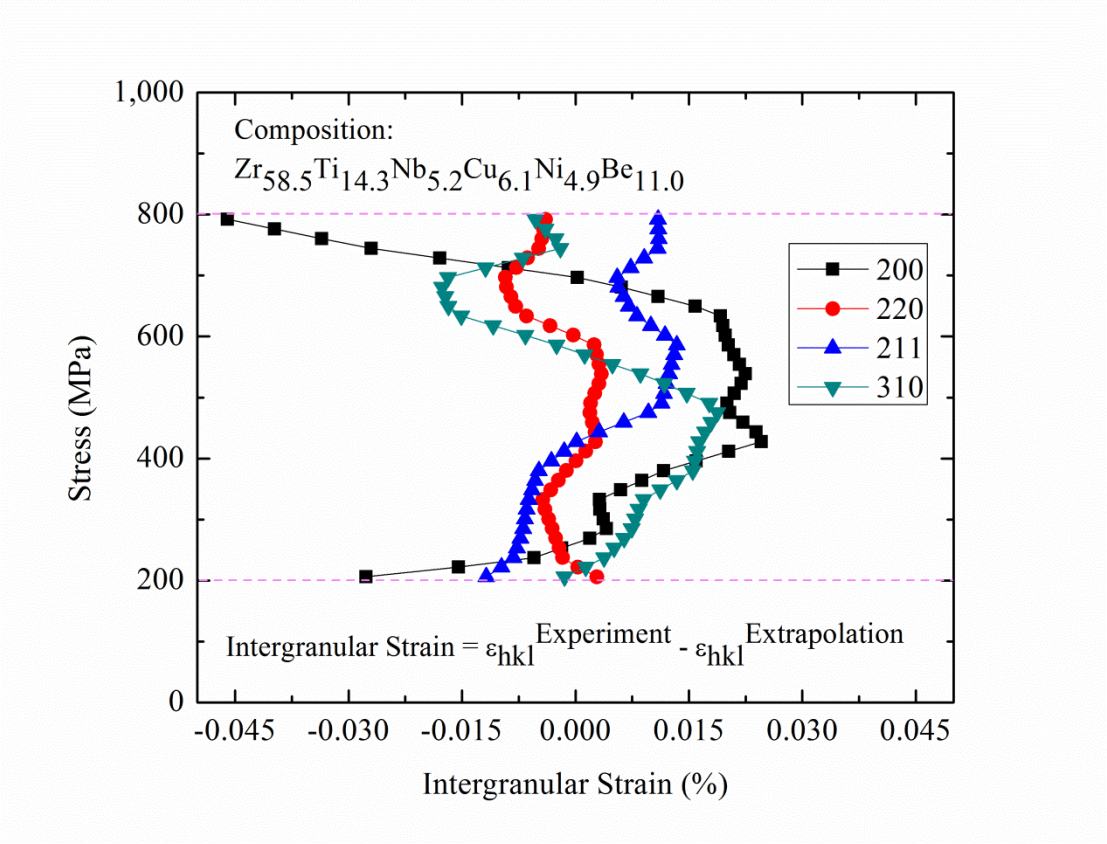

Figure 31. Stress versus intergranular strain curves for [200], [211], [220], and [310] grains in the transition from Stages I to II. [186]

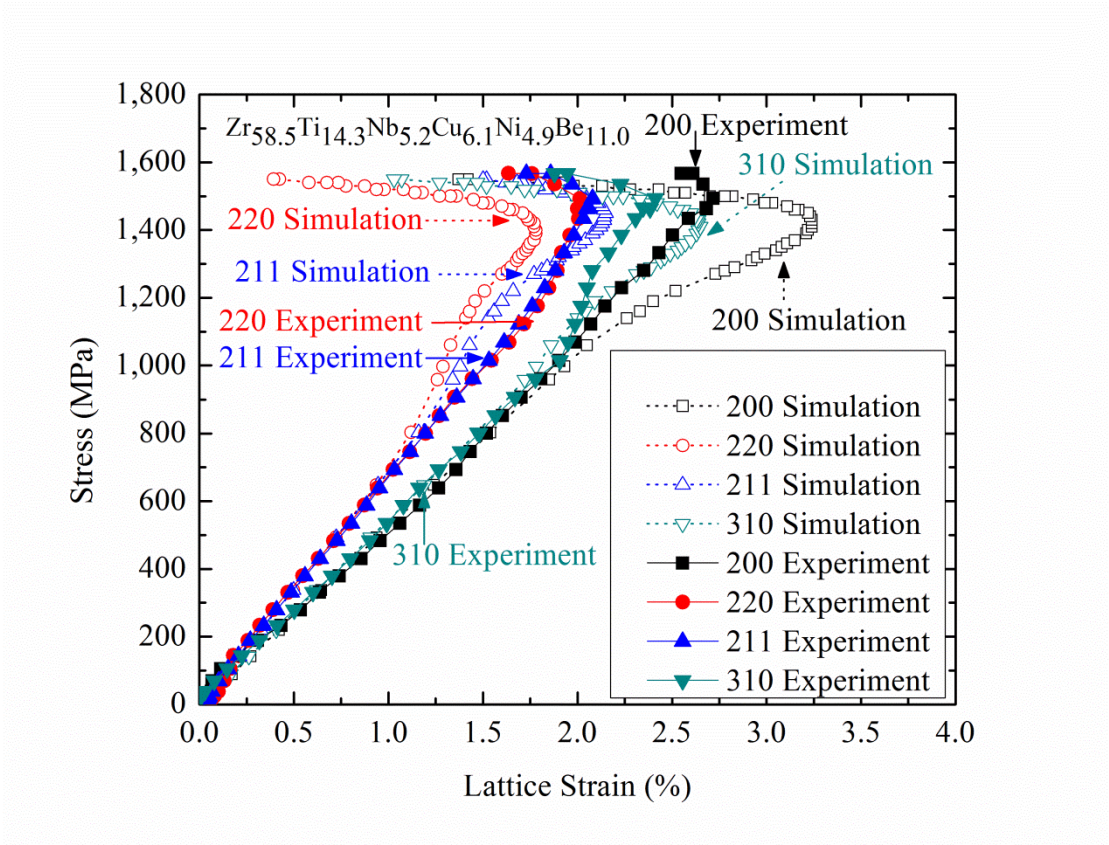

Figure 32. Experimental and finite element simulation results of the lattice strain evolution curves for [200], [211], [220], and [310] grains. [186]

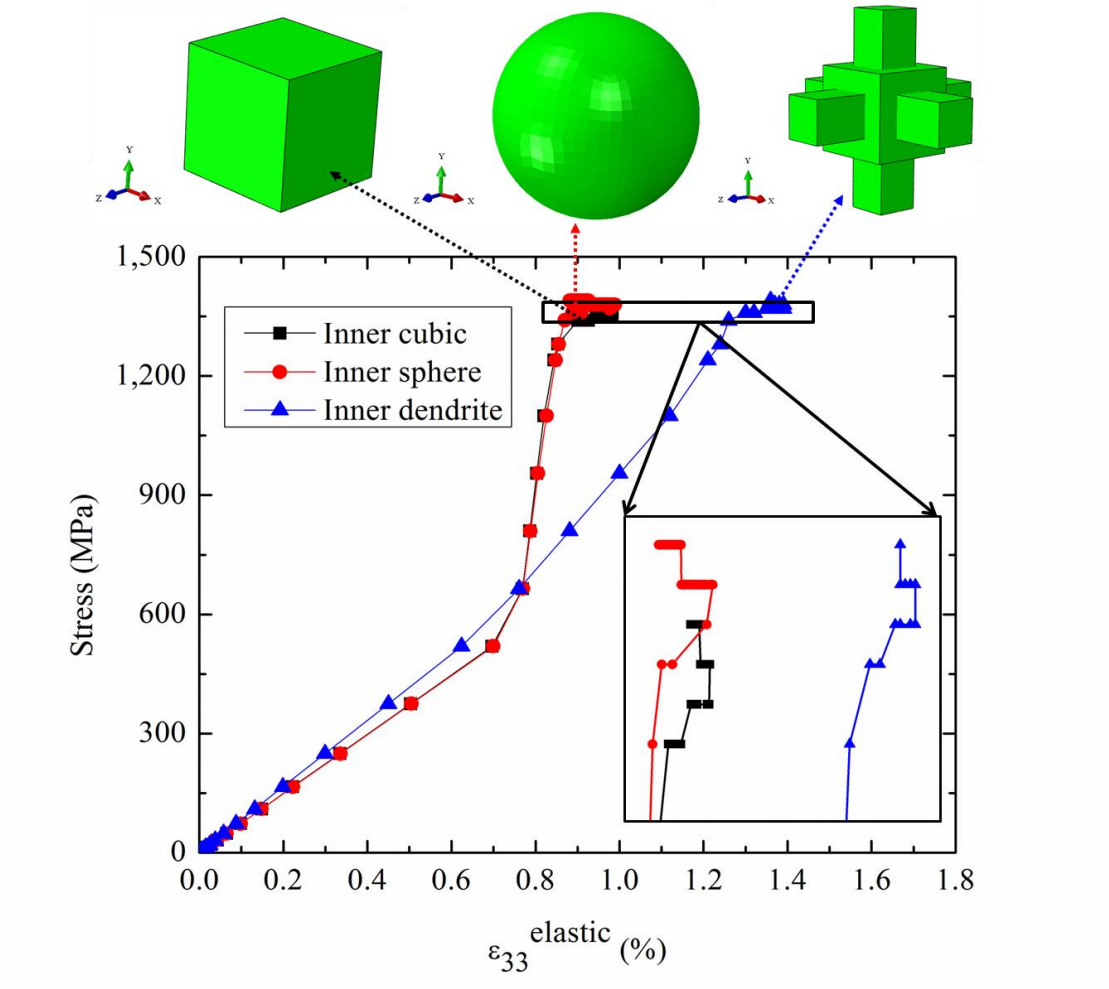

Figure 33. Stress versus $\varepsilon_{33}^{elastic}$ curves of the single inclusion model with cubic, spherical, and dendritic inclusion shapes (inset). [186]

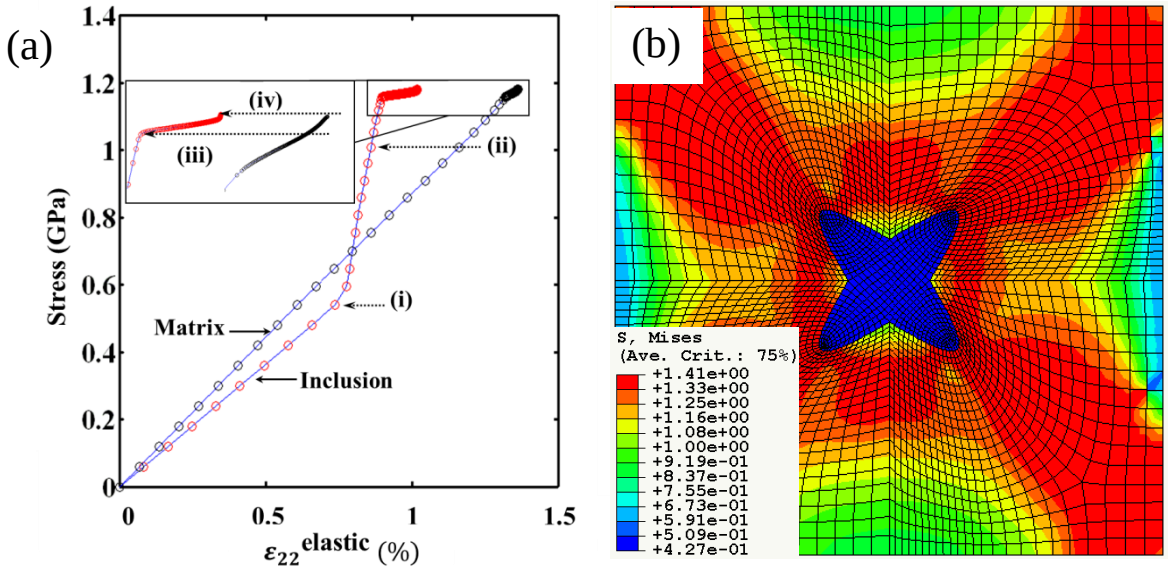

Figure 34. (a) Stress versus $\varepsilon_{22}^{elastic}$ curves for both the inclusion and matrix in the composite with the dendrite inclusion shown in (b), which shows the Mises stress contours at stress level (iv). Both the matrix and inclusion are simulated as elastic-perfectly plastic solids, with Young's modulus, Poisson's ratio, and yield stress being 89 GPa, 0.37, and 1.4 GPa for the matrix, and 60 GPa, 0.37, and 0.45 GPa for the inclusion. [186]

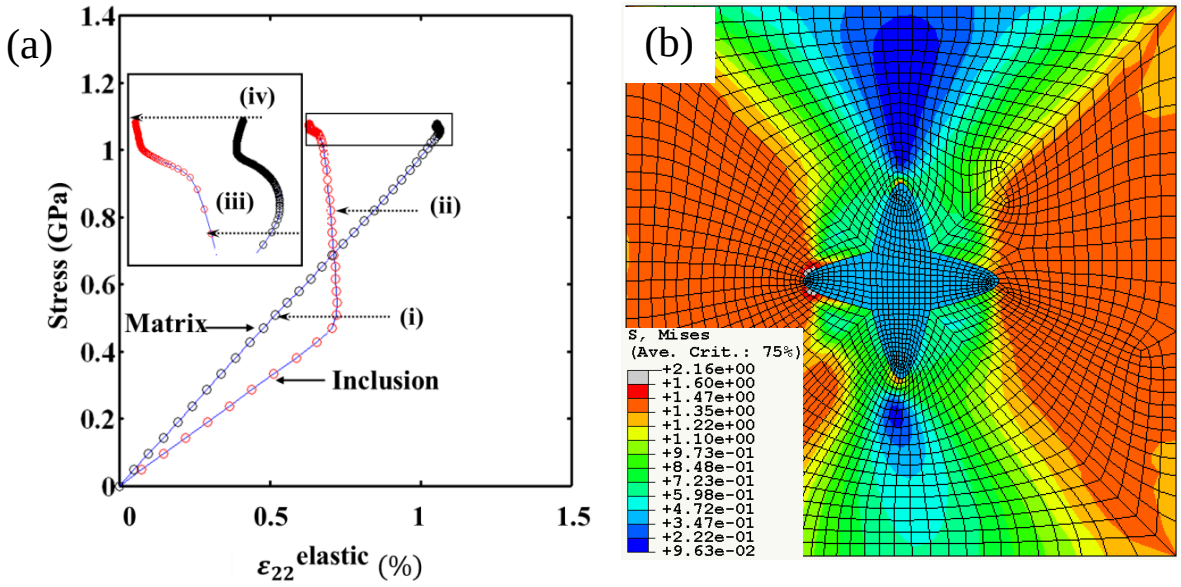

Figure 35. (a) Everything else being the same as Figure 34(a), the rotation of the dendritic crystalline phase by 45 ºleads to a dramatic change of the lattice strain evolution when the matrix yields (i.e., at the very end of the stress - $\varepsilon_{22}^{elastic}$ curves). (b) The Mises stress contours of model in (a) at stress level (iv). [186]

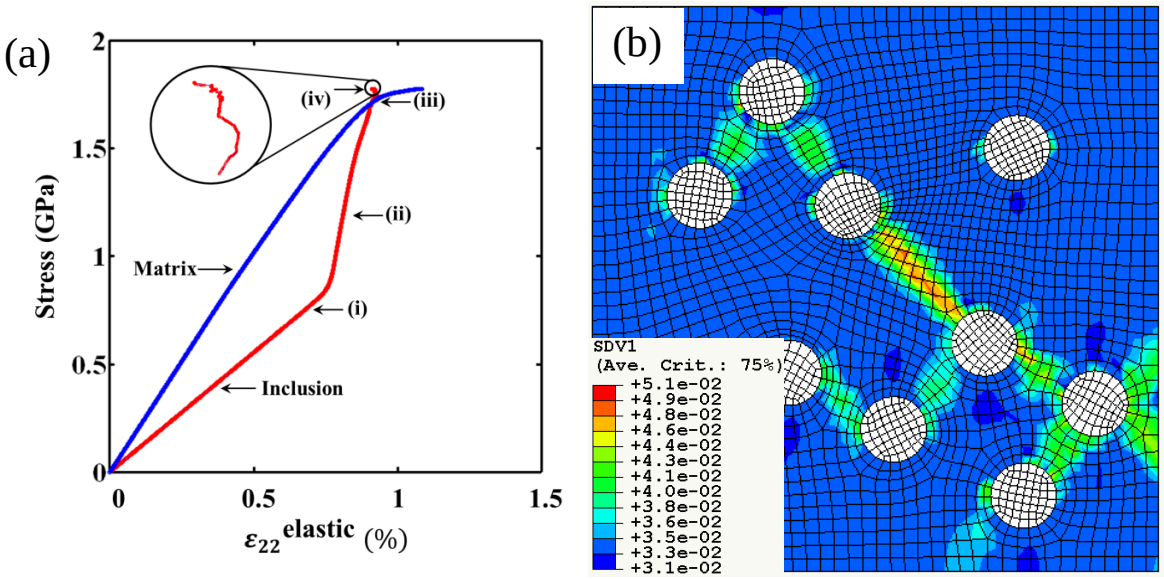

Figure 36. (a) Stress versus $\varepsilon_{22}^{elastic}$ curves for both the inclusion and matrix in the composite with multiple circular inclusions; (b) The Mises stress contour is shown at stress level (iv). The matrix is described by the free volume constitutive model, with the Young's modulus and Poisson's ratio being 200 GPa and 0.37, respectively. Other parameters can be found in the text. The inclusion phase is an elastic-perfectly plastic solid with the Young's modulus, Poisson's ratio, and yield stress being 60 GPa, 0.37, and 0.45 GPa, respectively. All figures are given in a deformed mesh with a displacement magnification ratio of 1, and the state-dependent variable 1 (SDV1) specifies the free volume. [186]

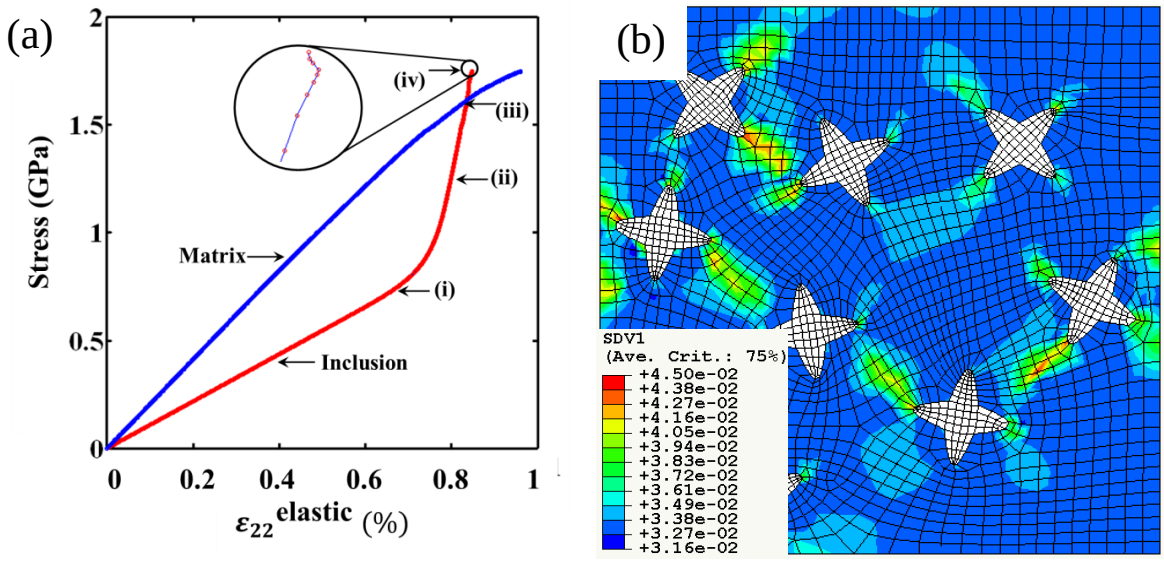

Figure 37. (a) Stress versus $\varepsilon_{22}^{elastic}$ curves for both the inclusion and matrix in the composite with multiple dendritic inclusions. (b) The Mises stress contour is shown at stress level (iv). The material parameters are all same as these in the Figure 36. [186]

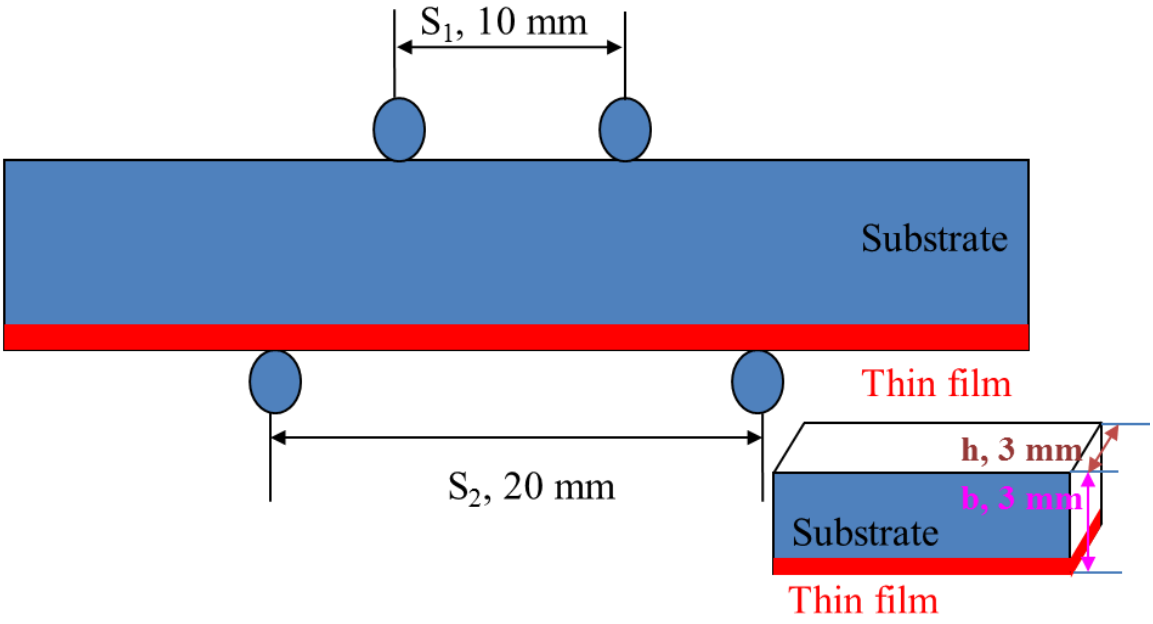

Figure 38. Specimen sketches for four-point-bending fatigue tests. [155]

Figure 39. (a) S-N and (b) S/UTS-N curves for all the reported TFMGs on different kinds of substrates. Five regions are separated in (a) by: A) low fatigue-endurance limit region; B) medium fatigue-endurance limit region; C) high fatigue-endurance limit region; D) tension-tension region; and E) monolithic BMG region. In (b), the regions, corresponding to (a), are represented by A', B', C', D', and E'. [155]

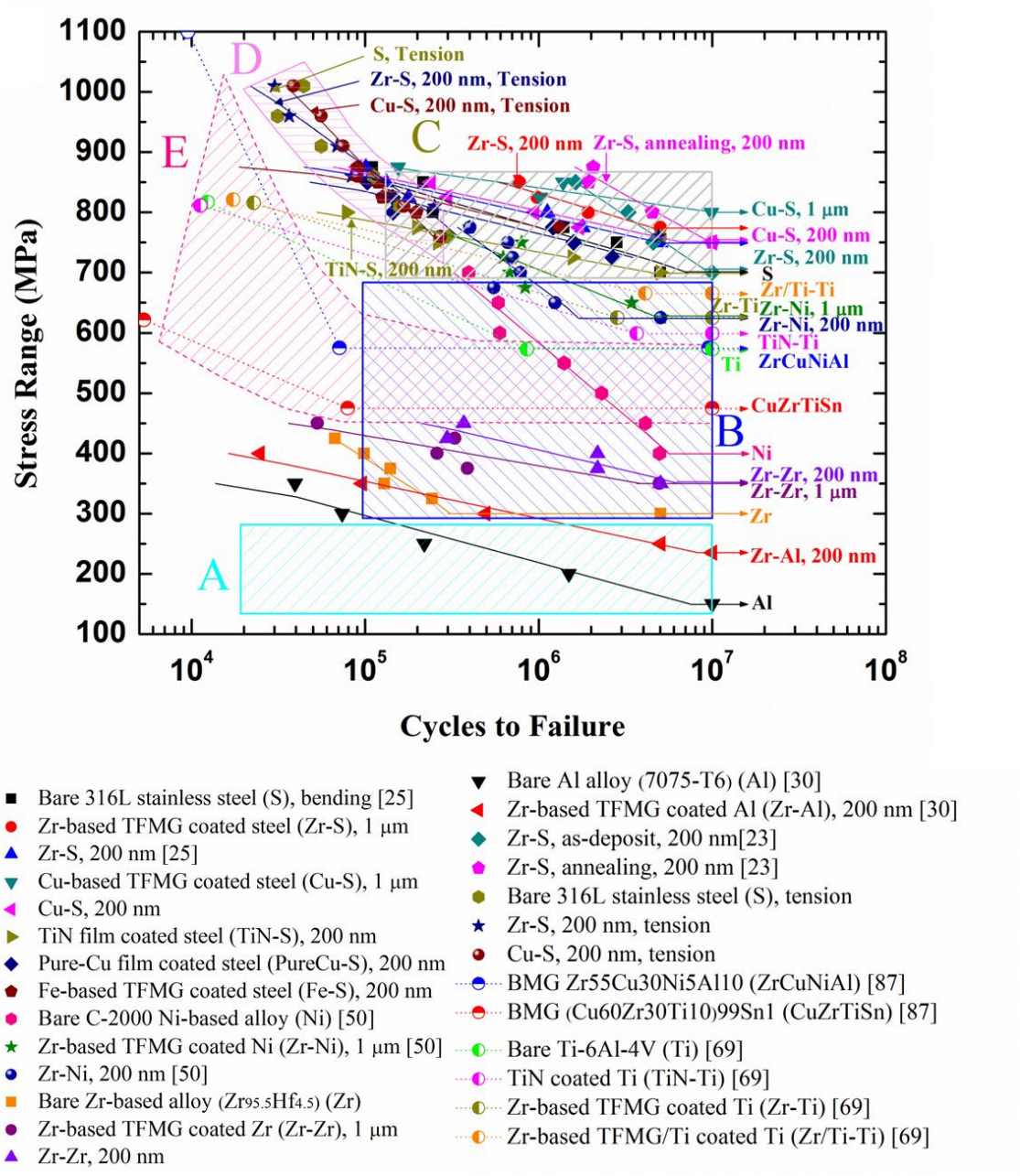

Figure 39 continued

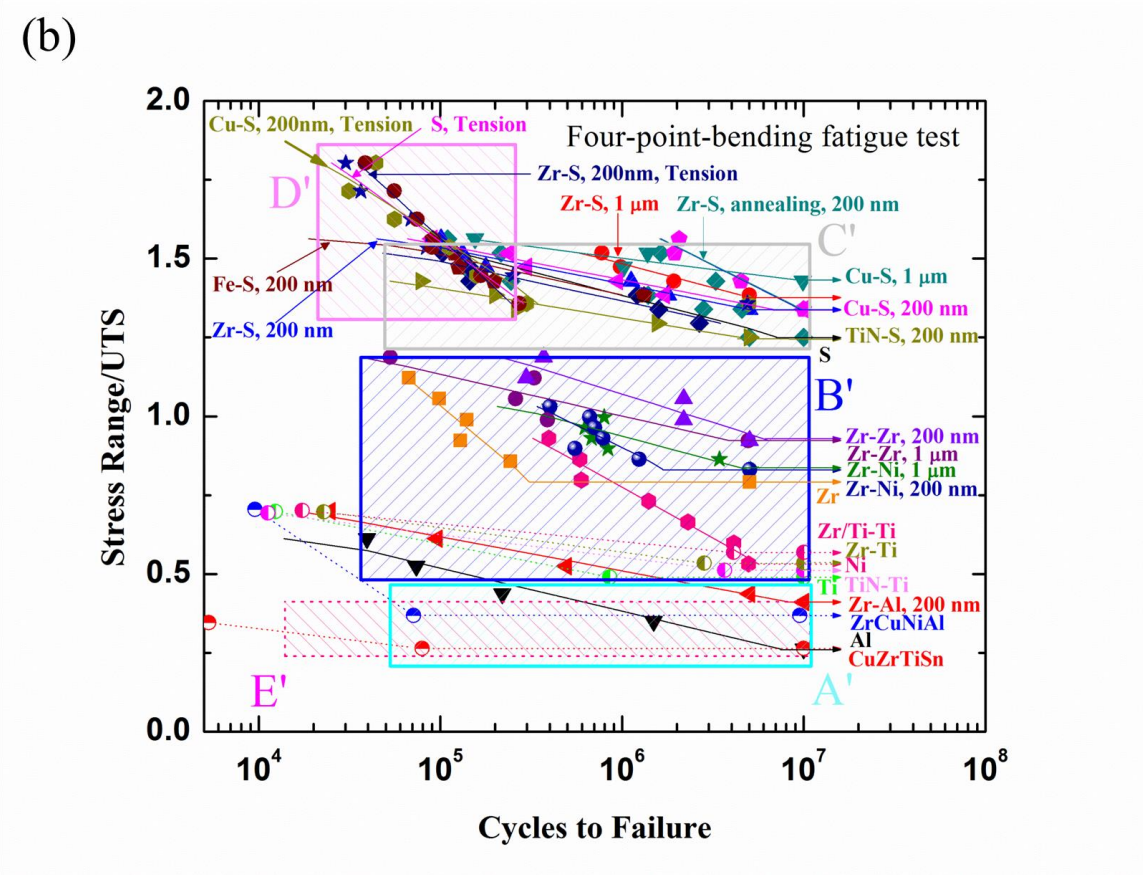

Figure 39 continued

Figure 40. (a) and (b) show the improvement of fatigue-endurance limit vs. UTS, improvement of fatigue-endurance limit/UTS vs. UTS, respectively, for all the reported substrate materials, including 316L steel, Ni-based alloy, Zr-based alloy, Ti-based alloy, and Al-based alloy. [155]

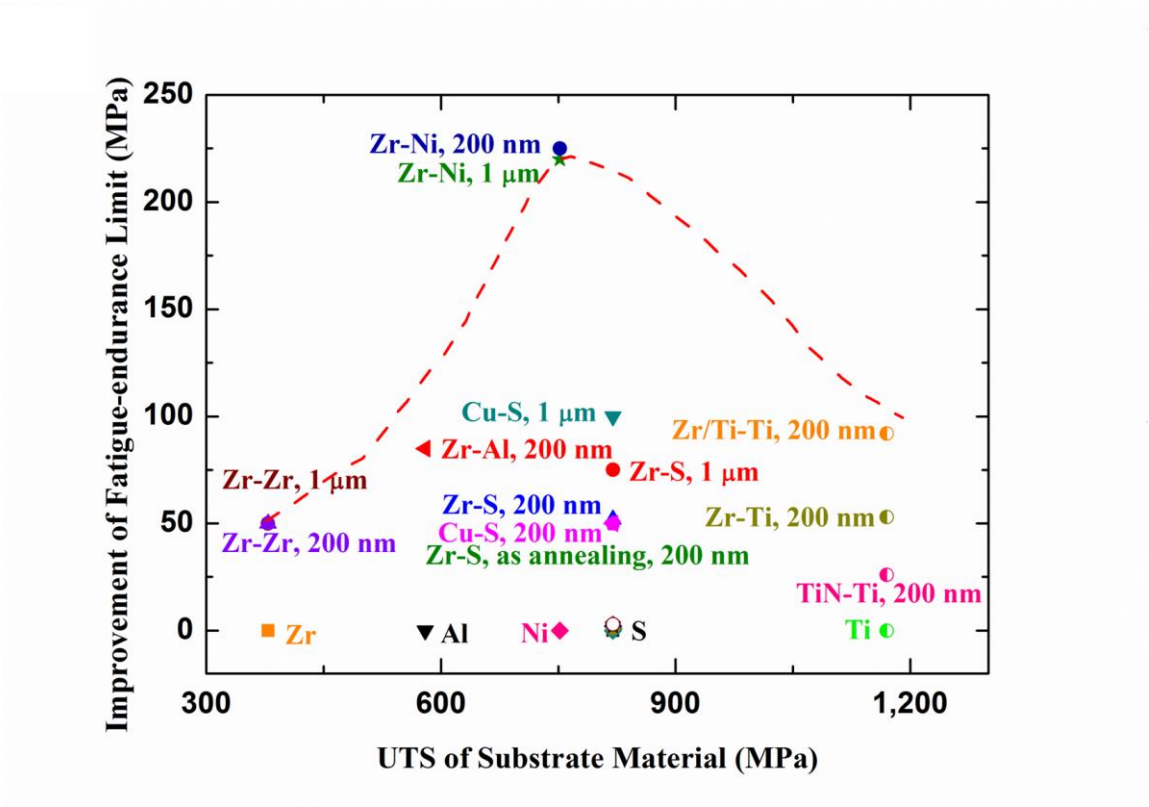

Figure 40 continued

(b)

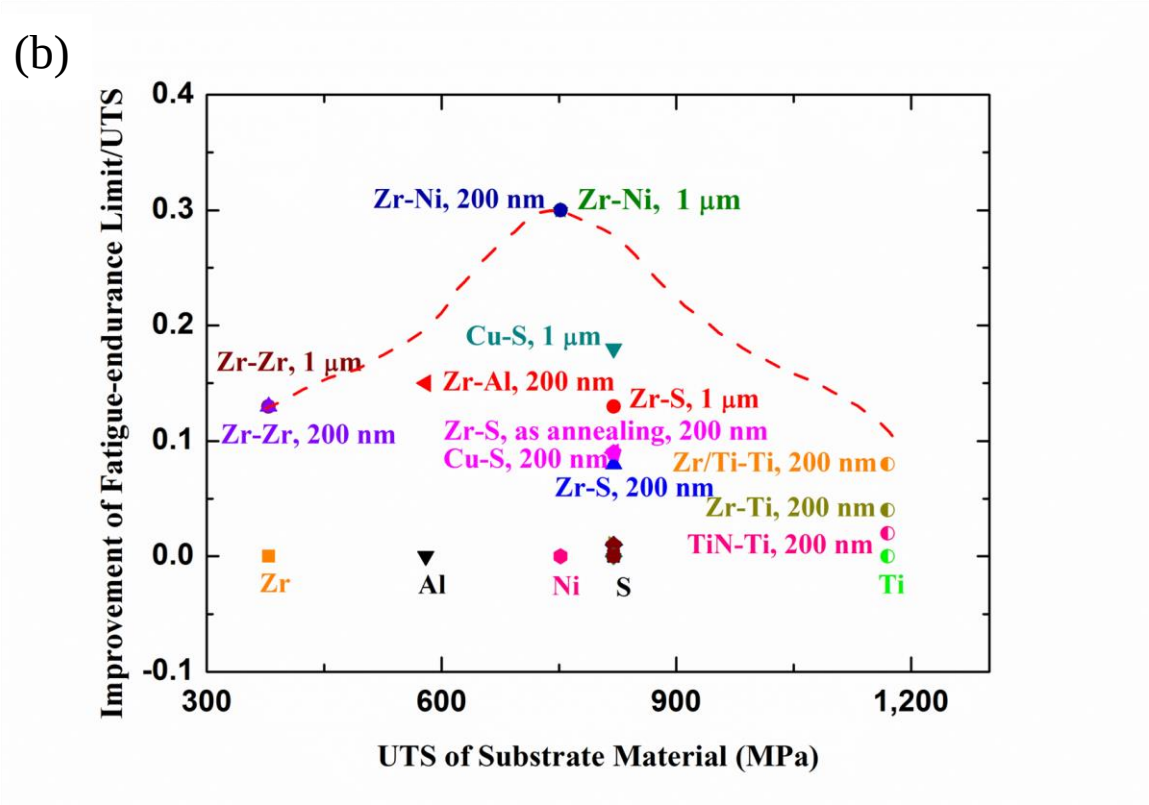

Figure 40 continued

Figure 41. (a), (b) and (c) show the improvement of fatigue-endurance limit vs. fatigue-endurance limit, improvement of fatigue-endurance limit/UTS vs. fatigue-endurance limit, and fatigue-endurance limit vs. UTS, respectively, for all the reported substrate materials, including 316L steel, Ni-based alloy, Zr-based alloy, Ti-based alloy, and Al-based alloy. [155]

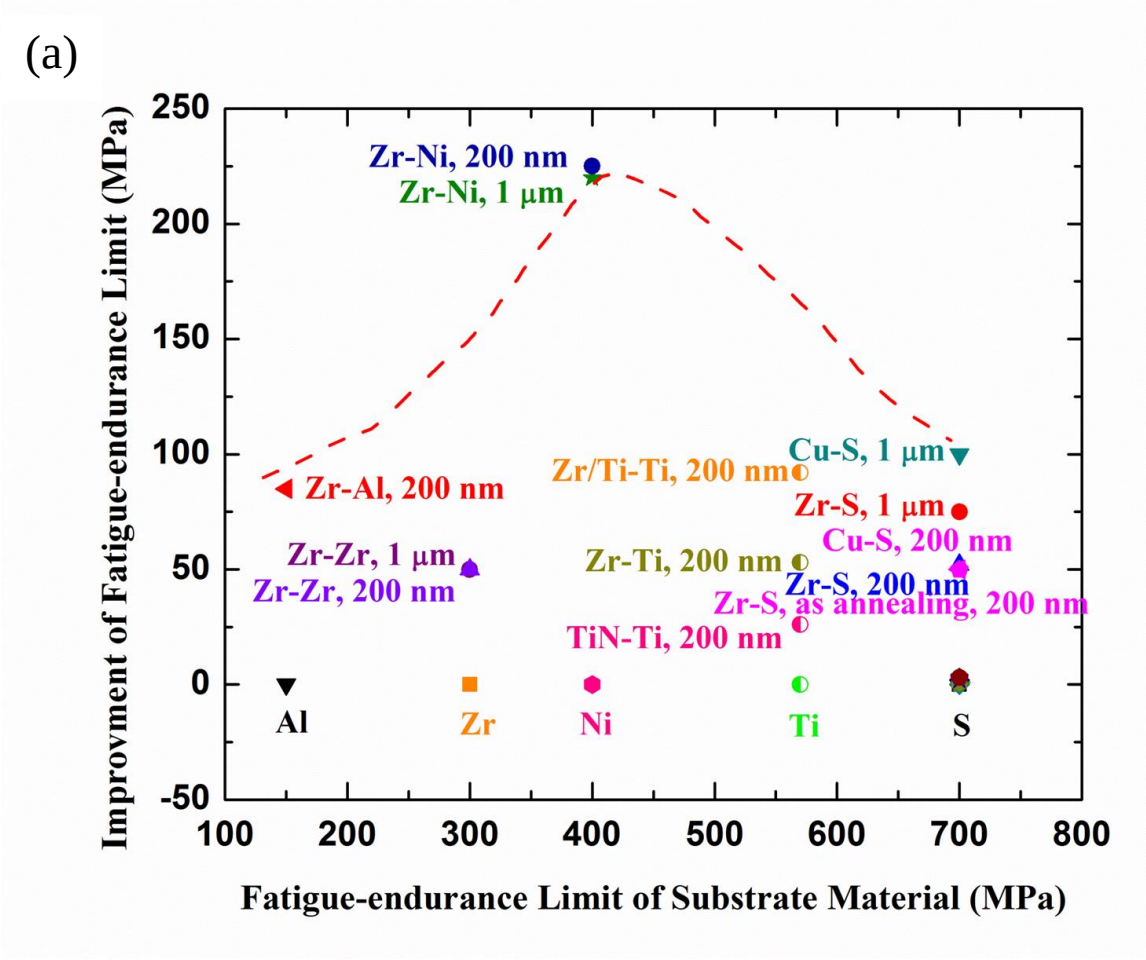

Figure 41 continued

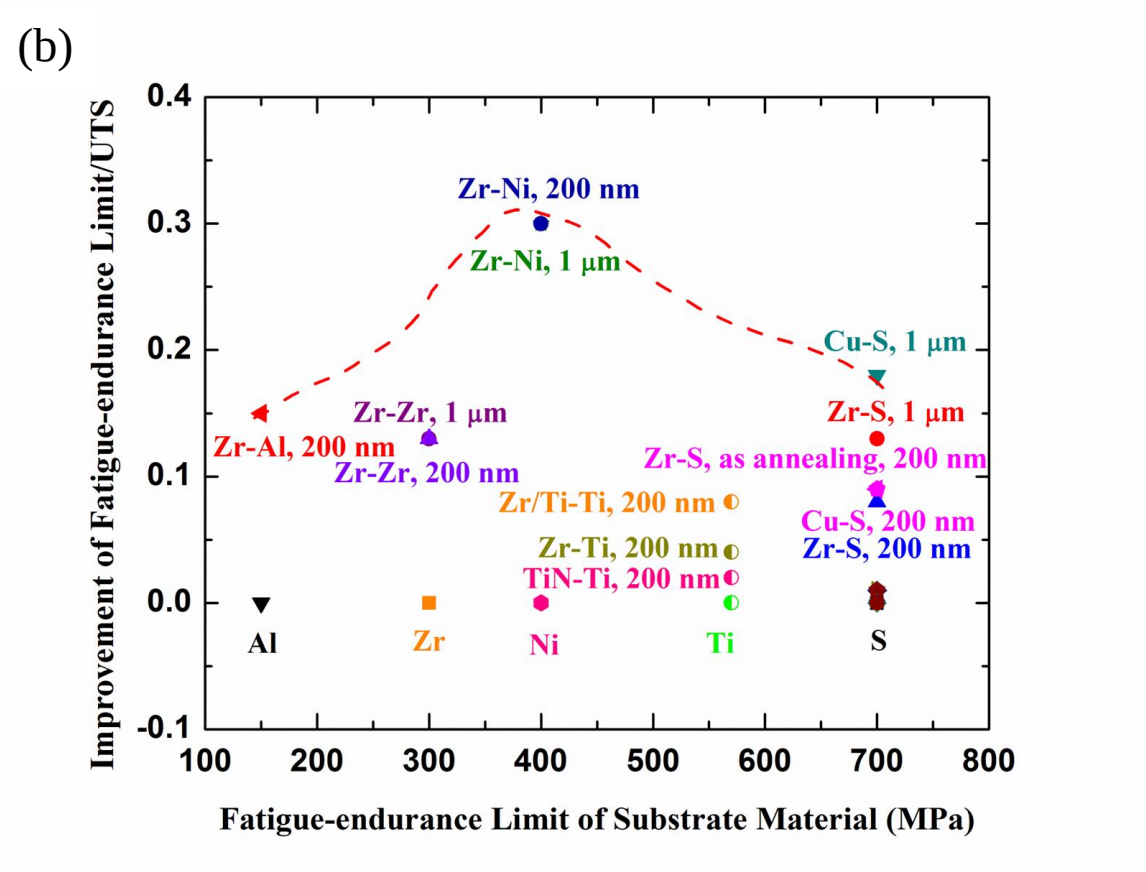

Figure 41 continued

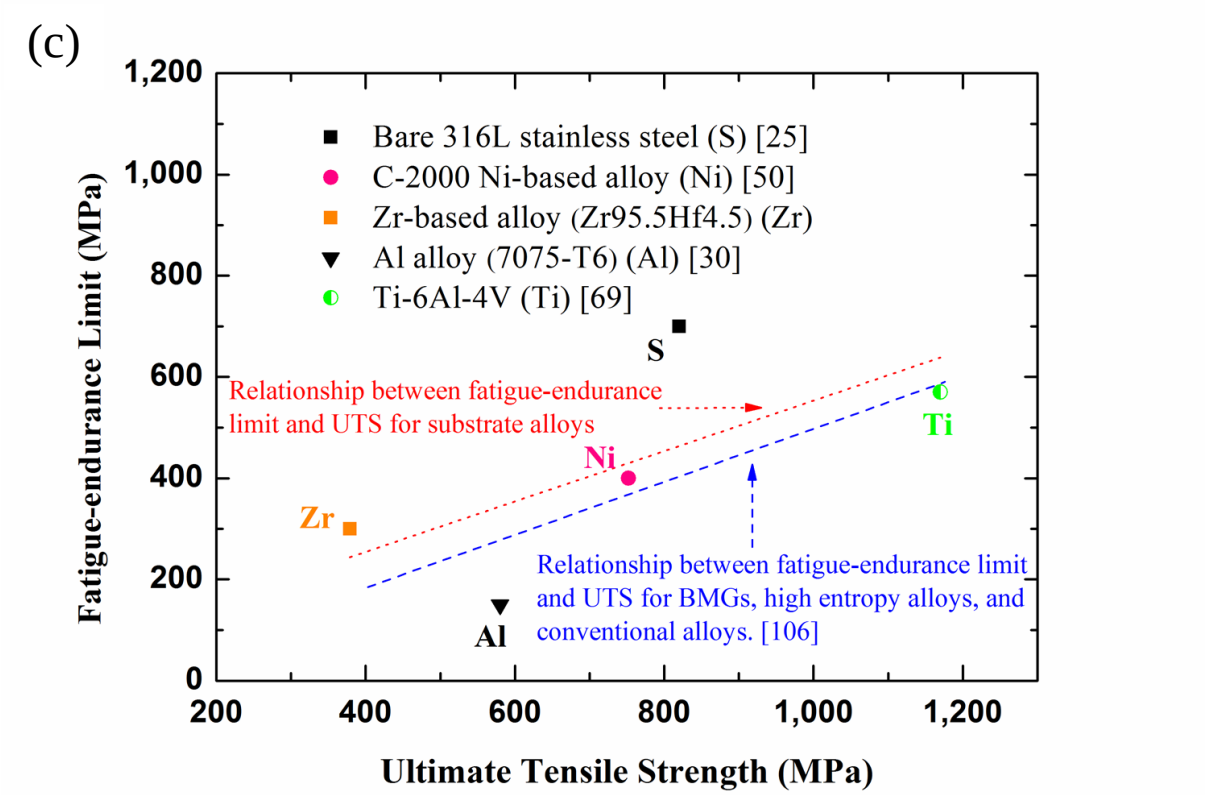

Figure 41 continued

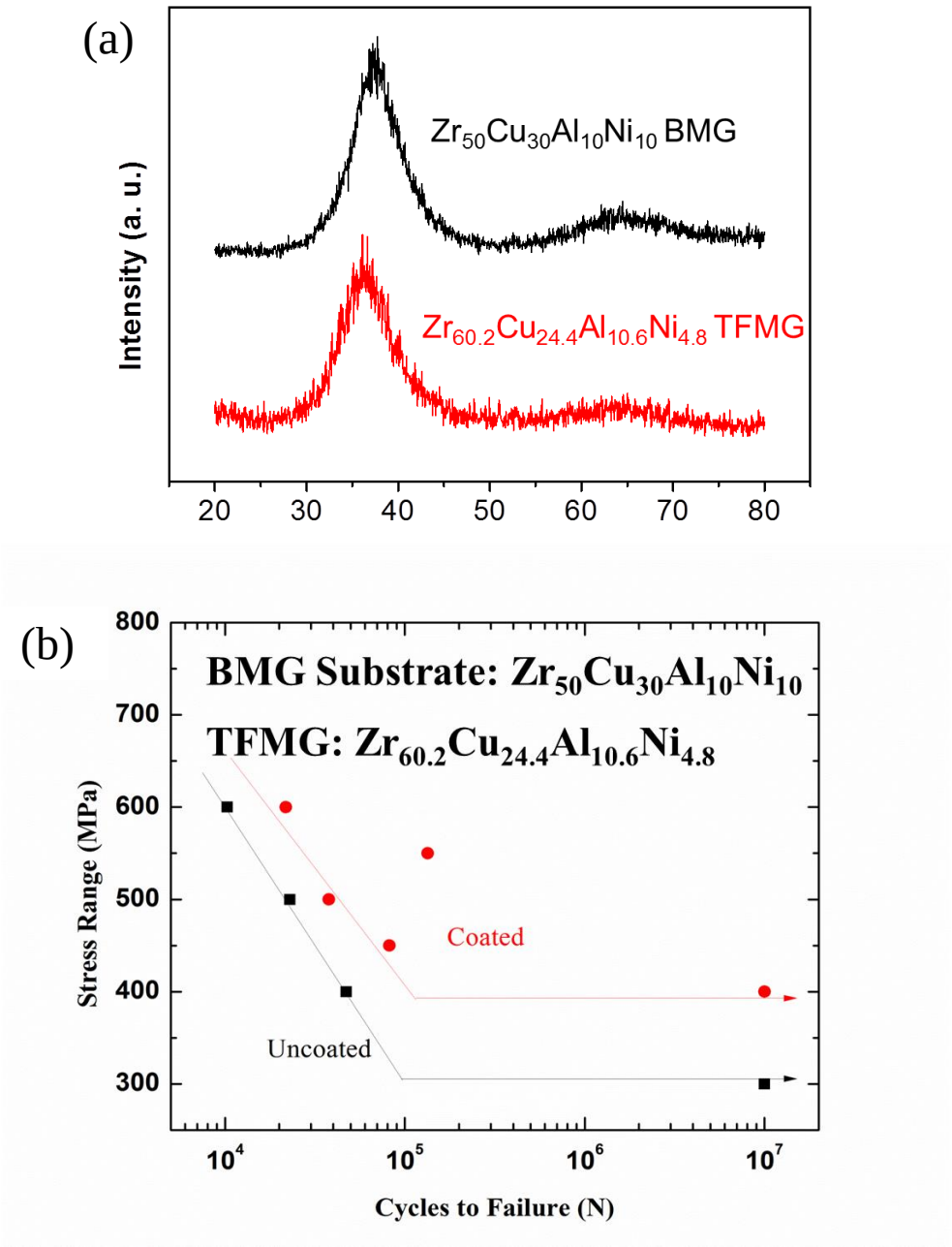

Figure 42. (a) XRD patterns for the BMG substrate and TFMG; and (b) S-N curves of bare BMG and BMG substrate with Zr-based TFMG.

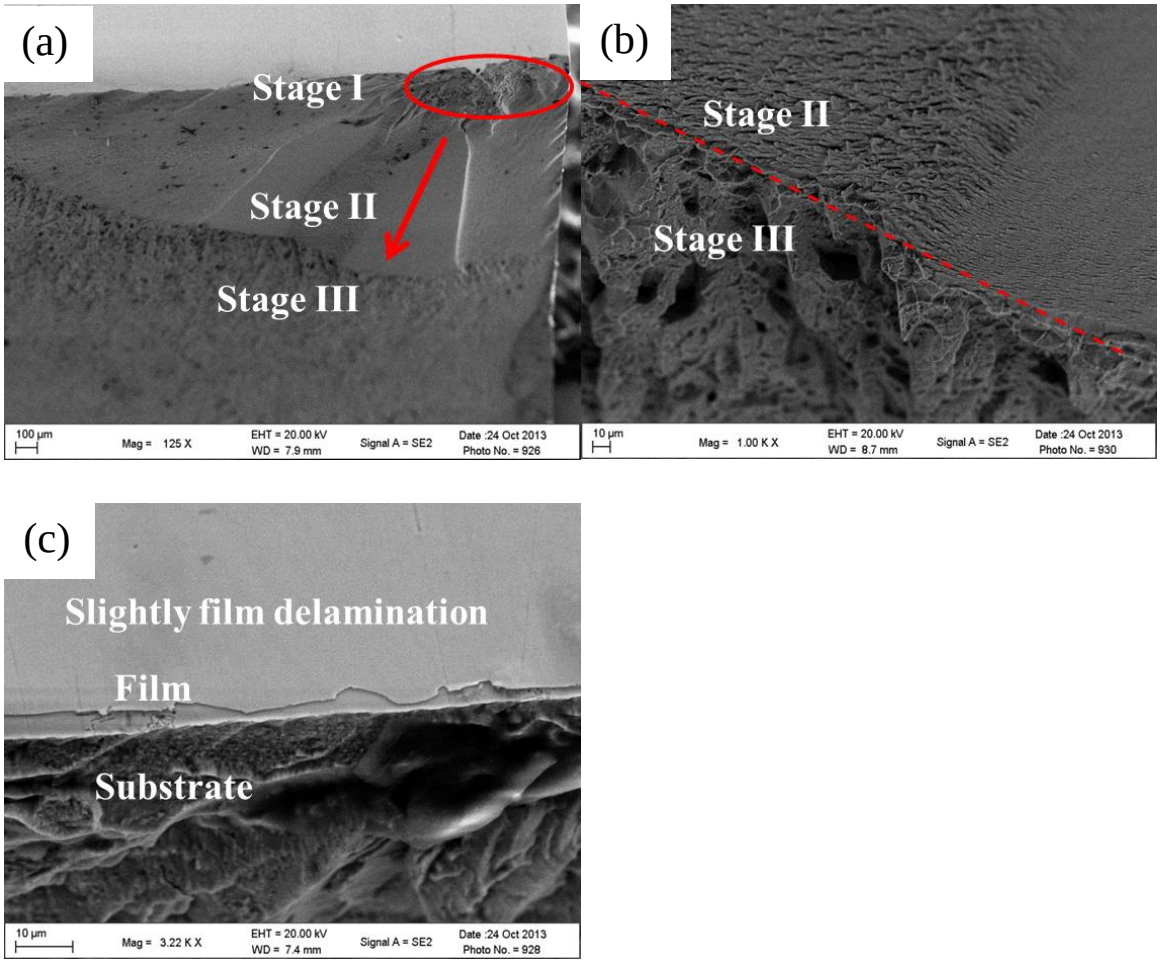

Figure 43. (a) SEM fractography micrograph of the BMG substrate with a 200 nm-thick Zr-based TFMG after fatigue fractured at σ_{max} = 450 MPa, (b) transition regions between Stage II and Stage III, and (c) partial film delamination due to the severe deformation of the BMG substrate.

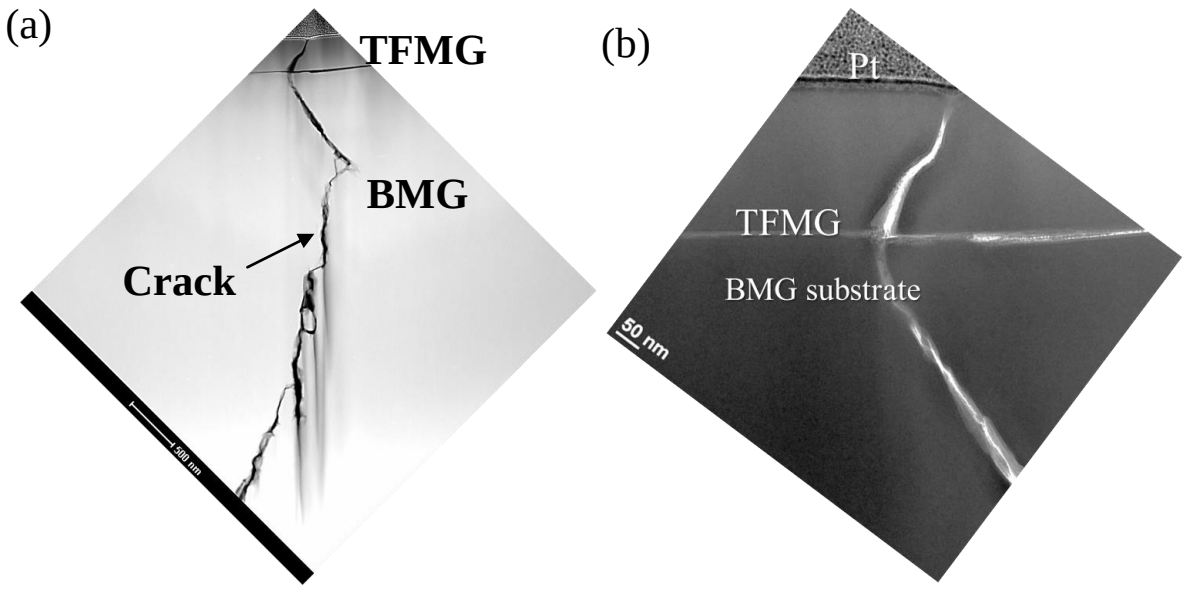

Figure 44. (a) TEM cross-sectional images of TFMG-coated BMG specimen after fatigue fractured at σ_{max} = 450 MPa. (b) Amplified image of the interface area in (a).

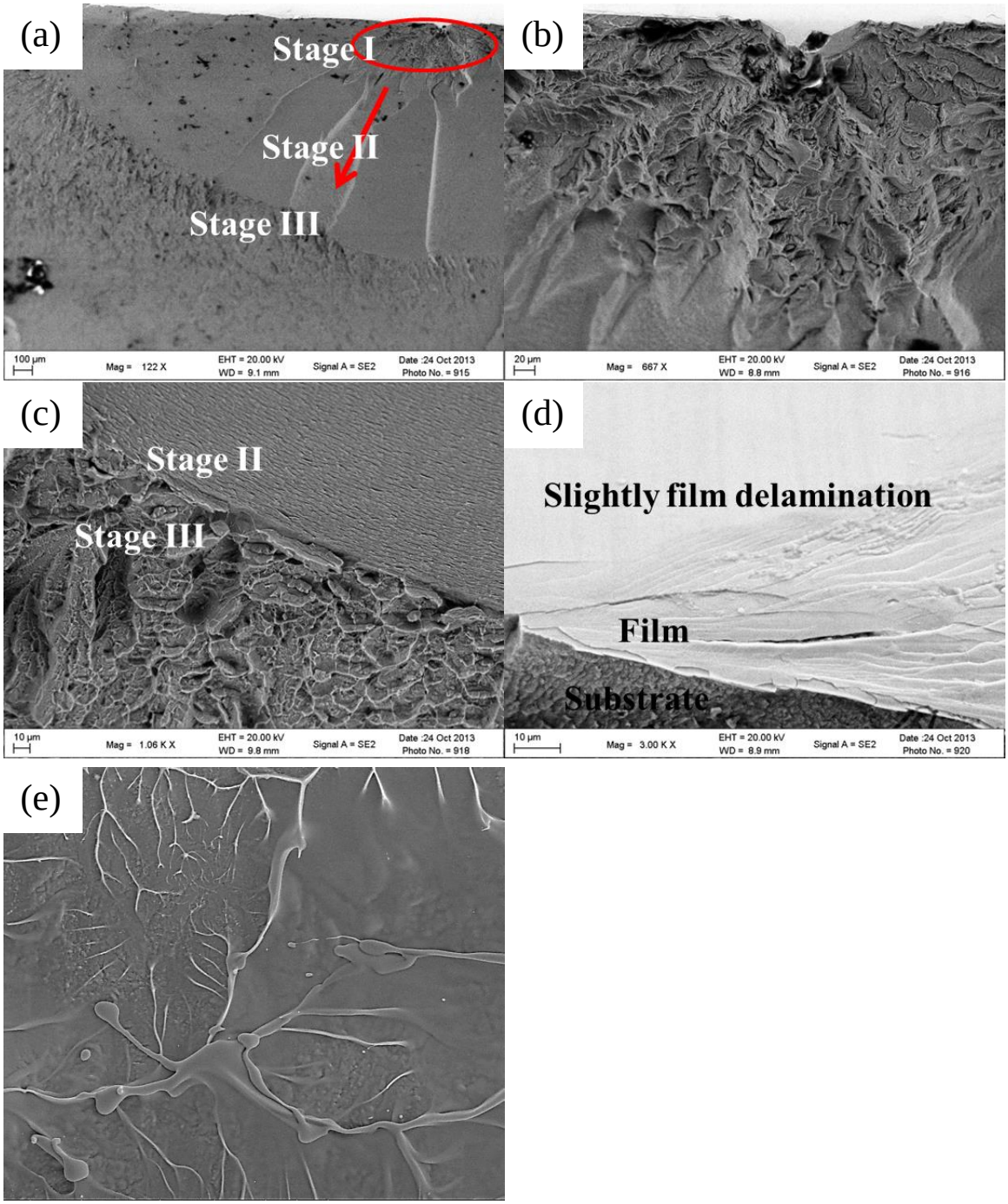

Figure 45. (a) SEM fractography micrograph of the BMG substrate with a 200 nm-thick Zr-based TFMG after fatigue fractured at σ_{max} = 500 MPa, (b) enlarged image of crack-initiation region, (c) transition regions between Stage II and Stage III, (d) partial film delamination due to the severe deformation of the BMG substrate, and (e) fast-failure region.

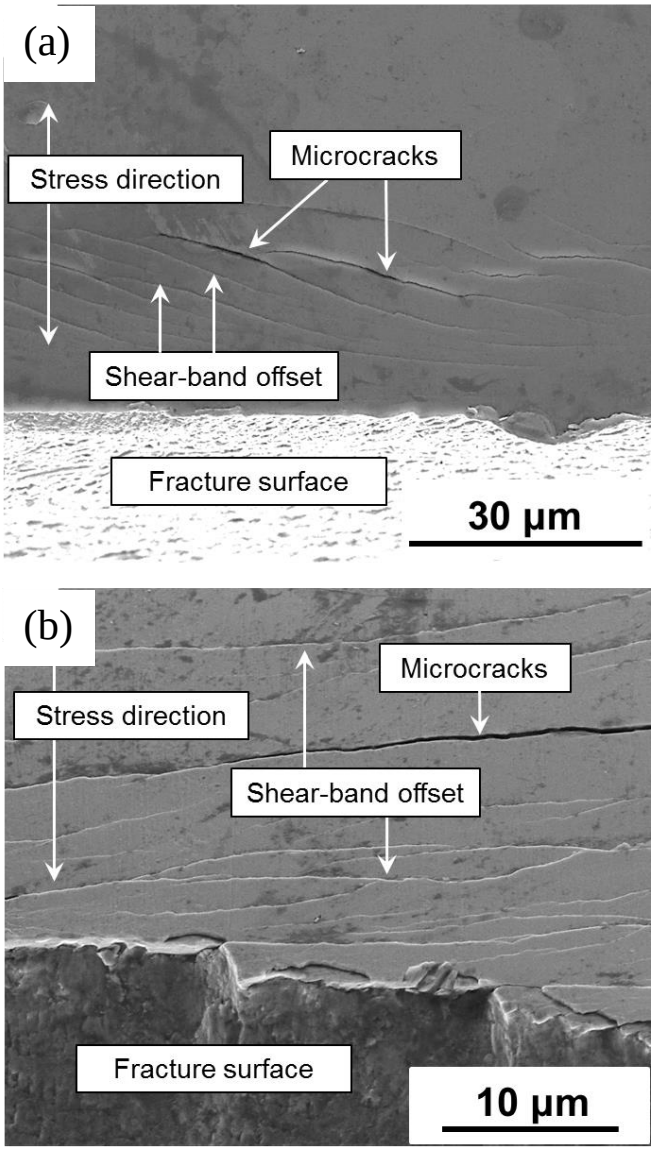

Figure 46. Microcracks associated with shear-off steps formed on the tensile surface near the fracture surface of a coated $Zr_{50}Cu_{30}A_{l0}Ni_{10}$ specimen tested at σ_{max} = 500 MPa. (a) and (b) are the tilt-view at different locations of sample in different magnifications.

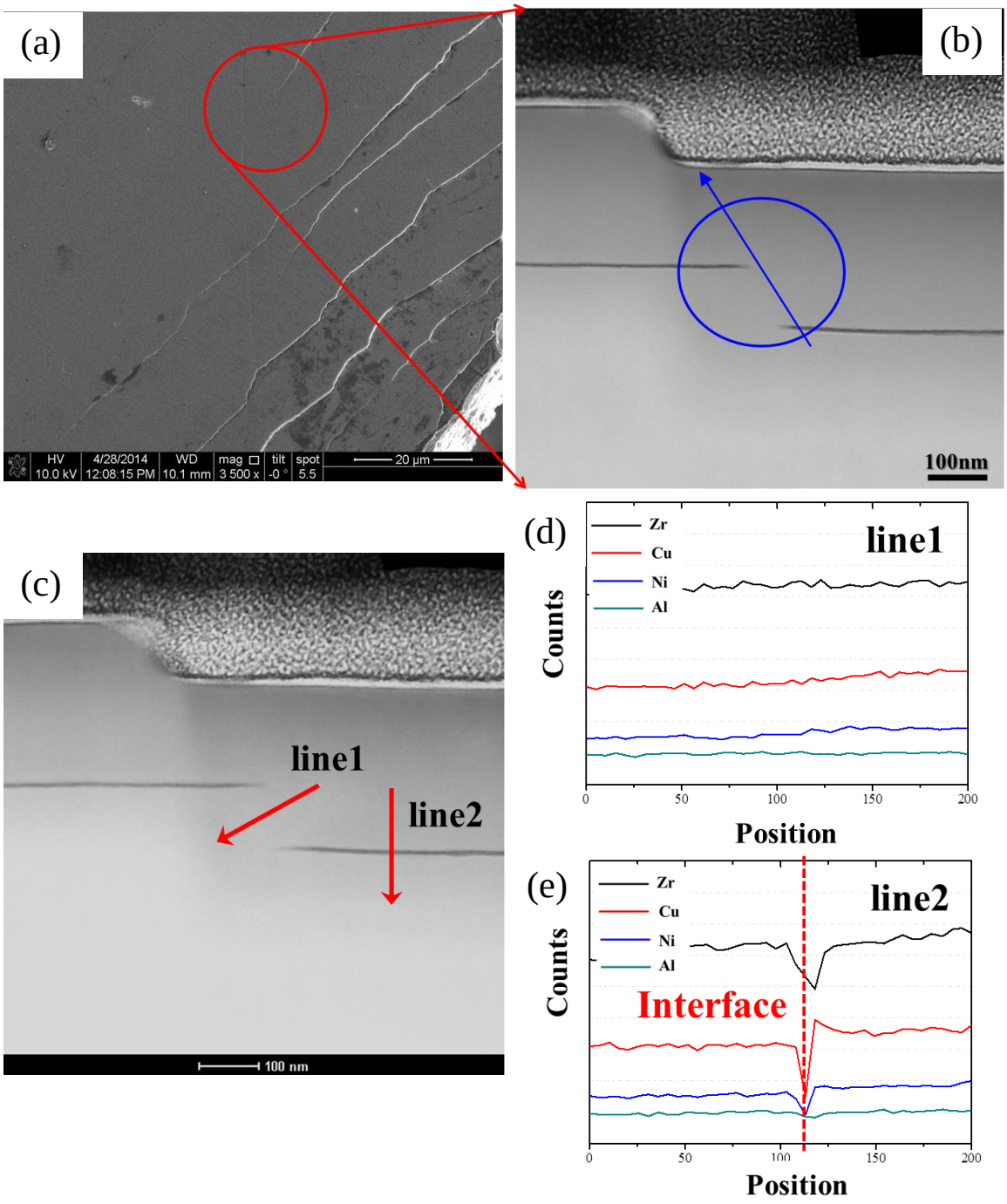

Figure 47. TEM EDS line-scans at the interface of TFMG and BMG substrate after fatigue fractured at σ_{max} = 500 MPa. (a) STEM image; (b) Enlarged TEM image of the shear offset area in (a); (c) EDS line-scan directions marked with the red arrows; (d) and (e) EDS line-scan profile at the interface of film and substrate.

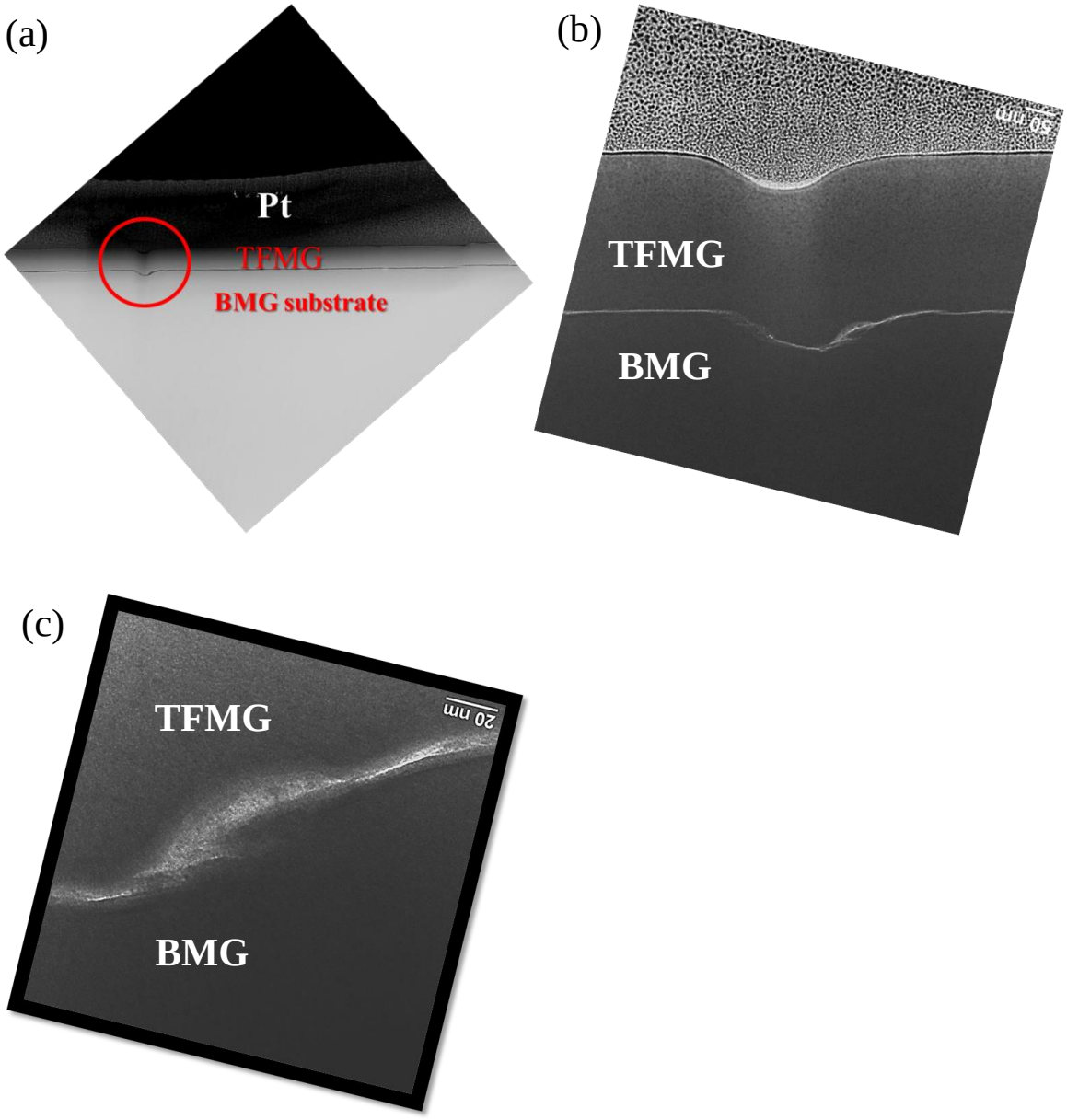

Figure 48. (a) TEM cross-sectional images of TFMG-coated BMG specimen after fatigue fractured at σ_{max} = 500 MPa; (b) Enlarged image of the red circle area in (a); and (c) Enlarged image of the red circle area in (c).

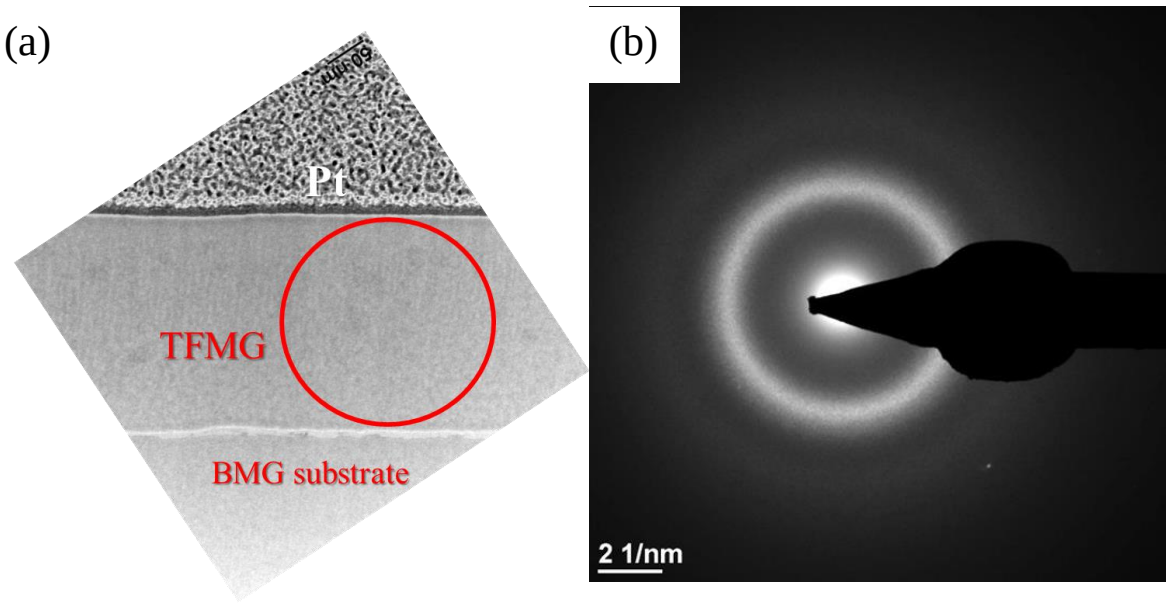

Figure 49. (a) TEM cross-sectional images of the film area in the TFMG-coated BMG specimen after fatigue fractured at σ_{max} = 500 MPa; (b) SAED result of the red circle area in (a), indicating the fully amorphous structure.

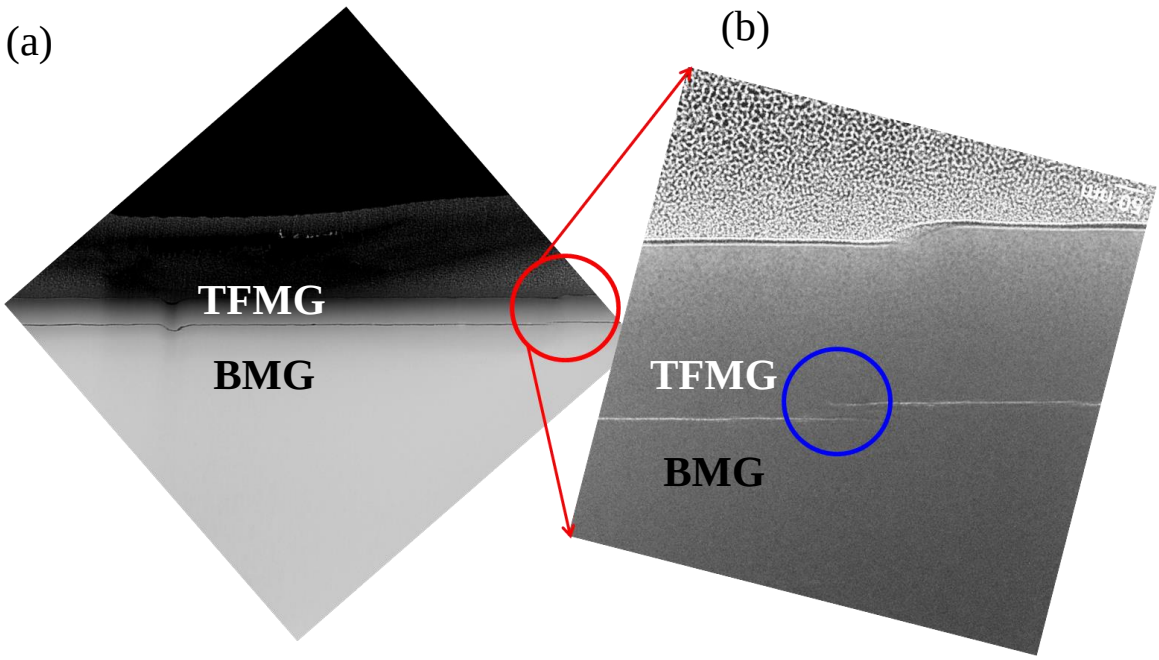

Figure 50. (a) TEM cross-sectional images of TFMG-coated BMG specimen after fatigue fractured at σ_{max} = 500 MPa; and (b) Enlarged image of the shear-off steps area (blue circle) in (a).

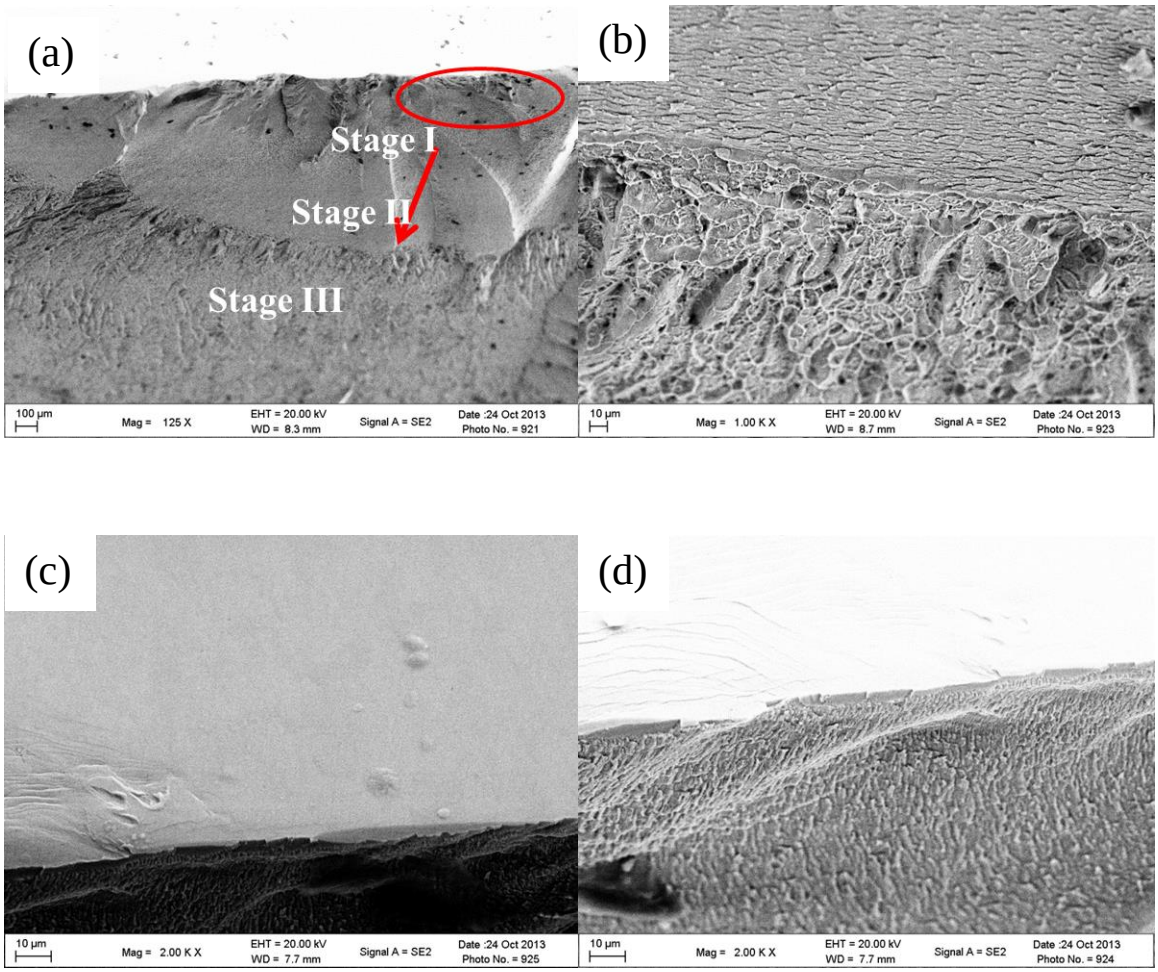

Figure 51. (a) SEM fractography micrograph of the BMG substrate with a 200 nm-thick Zr-based TFMG after fatigue fractured at σ_{max} = 600 MPa, (b) transition regions between Stage II and Stage III, (c) and (d) interface area of the TFMG-BMG specimen after fatigue fracture.

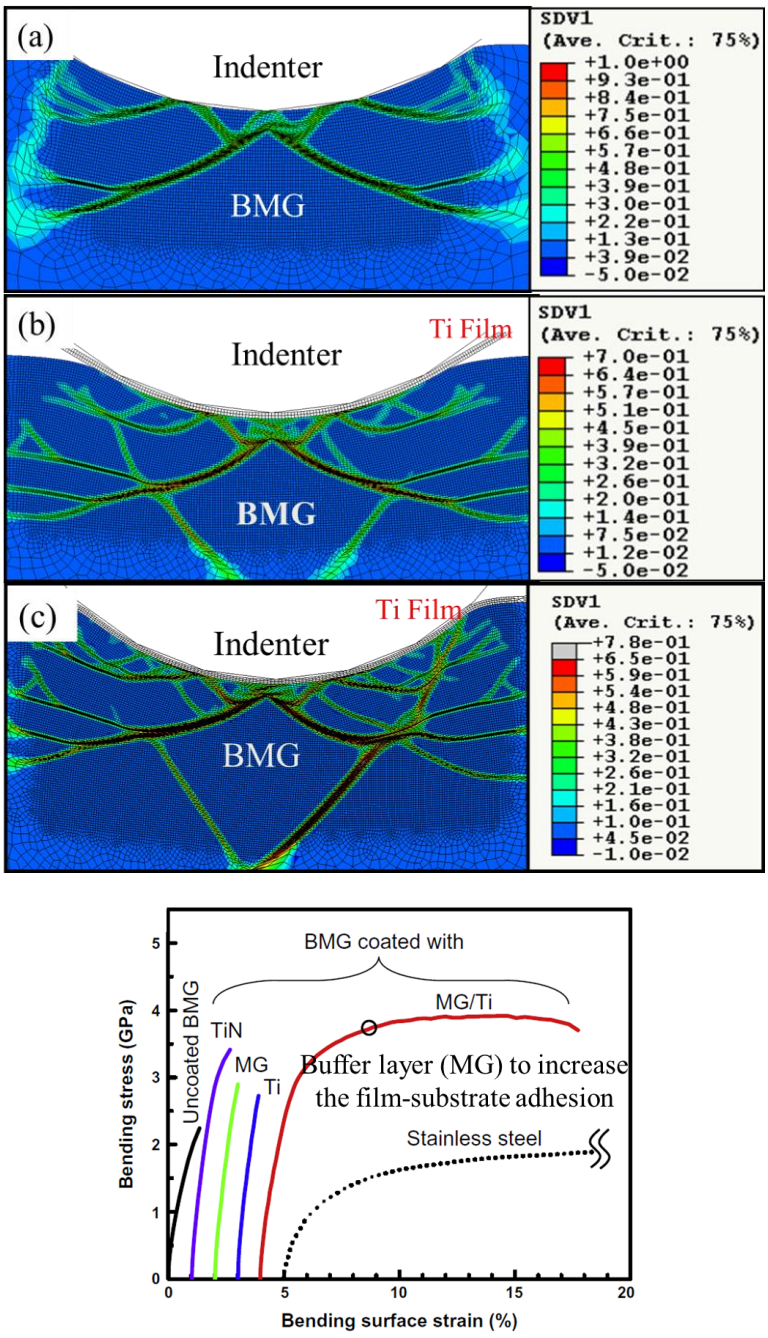

Figure 52. An indentation model (2D) with free-volume contour plots in different adhesion cases: (a) a BMG substrate without coatings; (b) a thin-film coated BMG, in which the substrate and film is completely bonded; (c) a BMG specimen coated with a weakly-bonded thin film; (d) bending stress vs. surface strain curves for uncoated and coated BMG samples, together with 316L stainless steel for comparison.

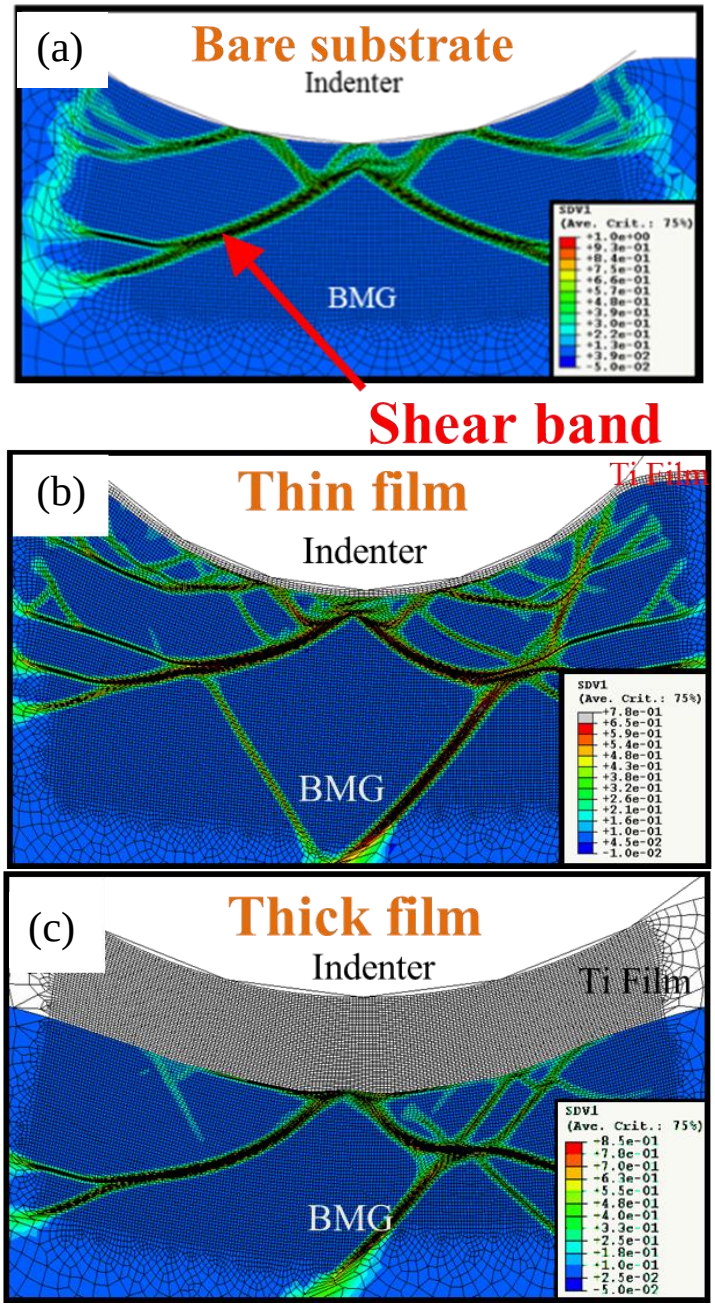

Figure 53. An indentation model (2D) with free-volume contour plots in different film-thickness cases: (a) a BMG substrate without coatings; (b) a BMG substrate with a thin TFMG, having a film/substrate thickness ratio of 1/20; and (c) a BMG substrate with a thick TFMG, having a film/substrate thickness ratio of 1/5.

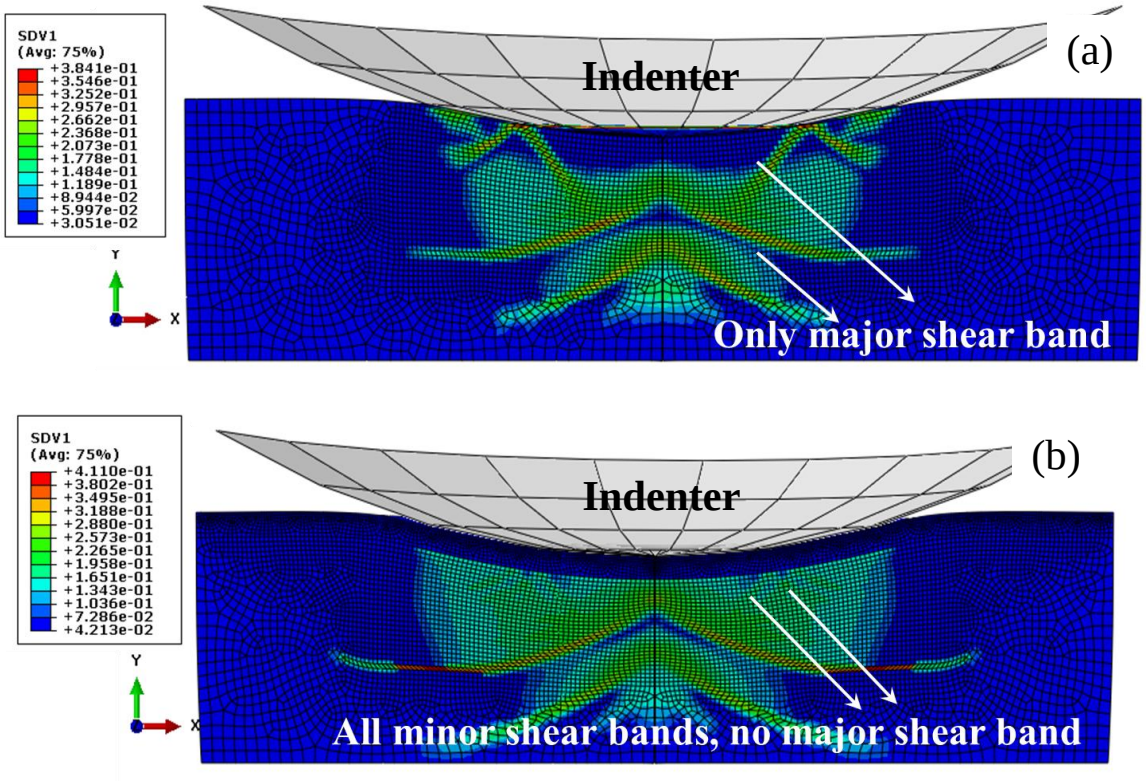

Figure 54. An indentation axisymmetric model (3D) with free-volume contour plots for BMG specimens: (a) without and (b) with TFMG.

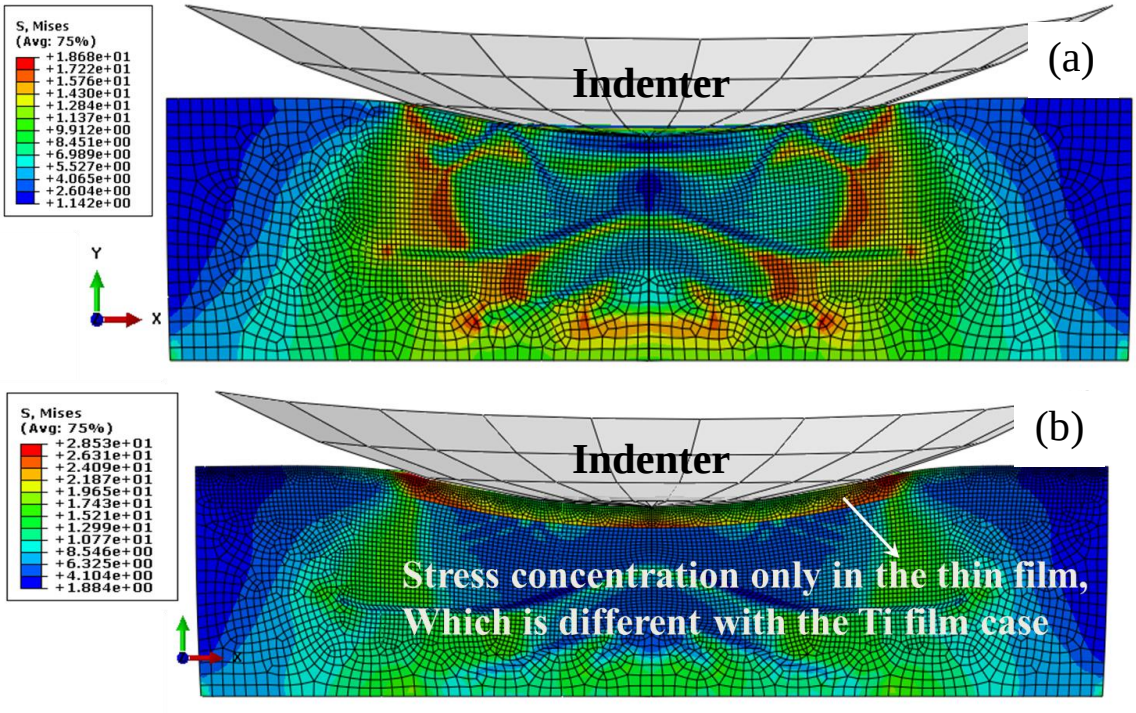

Figure 55. An indentation axisymmetric model (3D) with stress plots for BMG specimens: (a) without and (b) with TFMG.

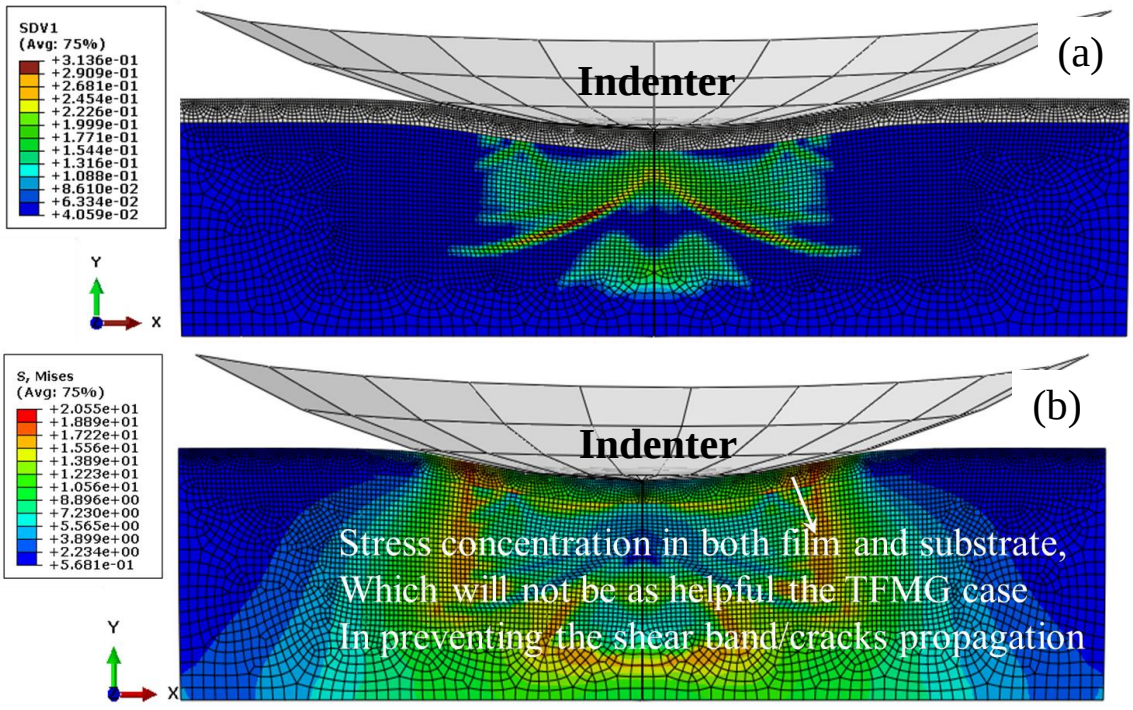

Figure 56. An indentation axisymmetric model (3D) with (a) shear band and (b) stress plots for BMG specimens coated with Ti-alloy thin film.

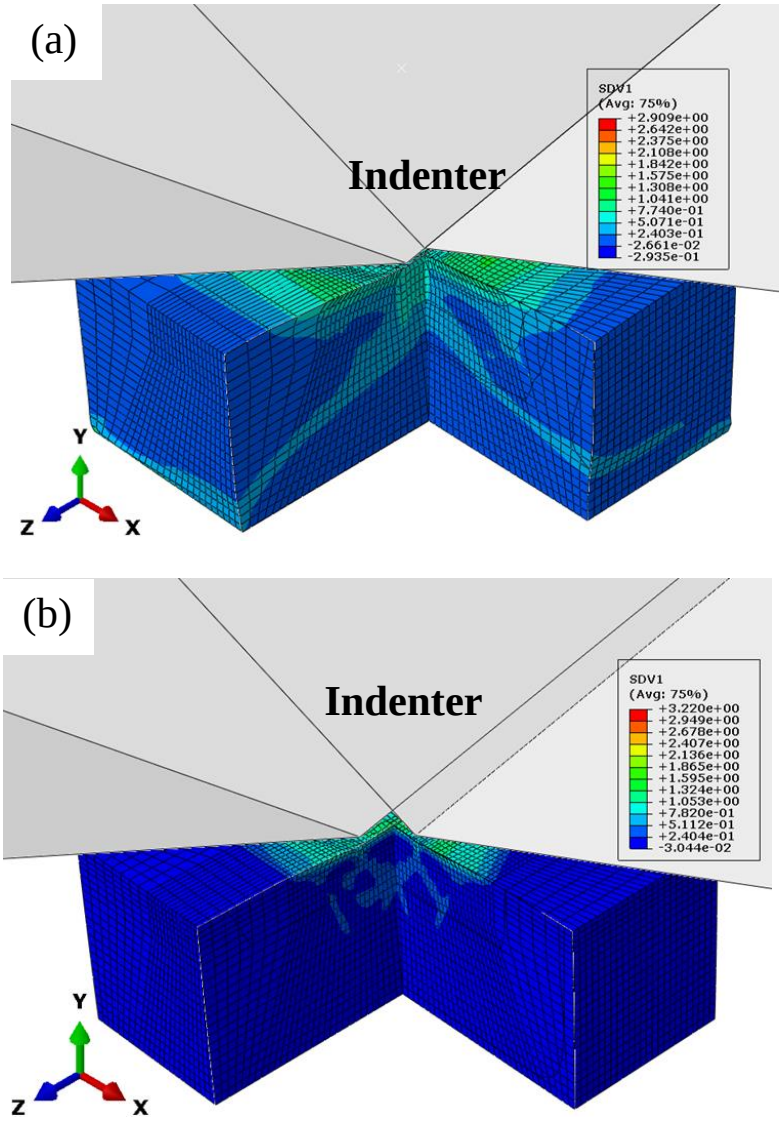

Figure 57. An indentation 3D model with shear-band plots for BMG specimens using Berkovich indenter: (a) without and (b) with TFMG.

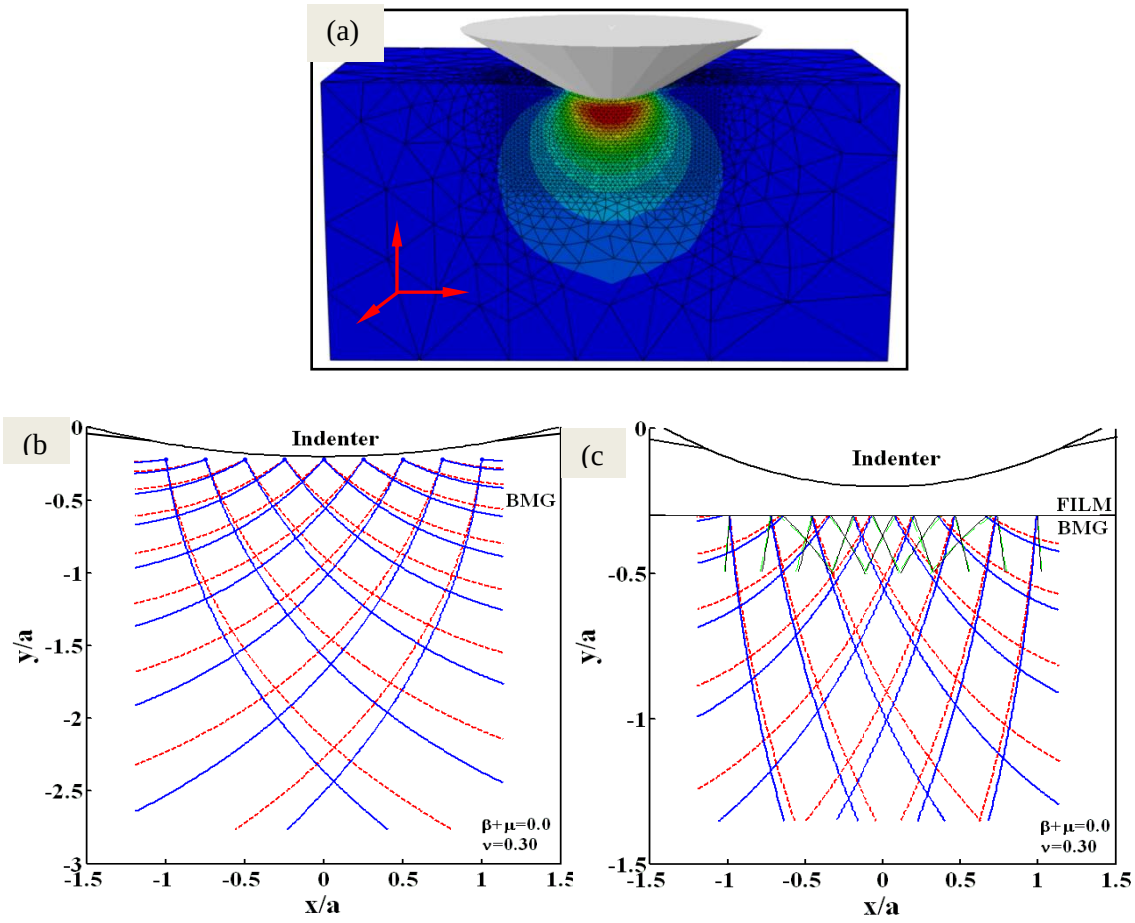

Figure 58. (a) ABAQUS model of a half-symmetric Rockwell indention in a metallic glass, used for predicting shear-band directions in (b) a BMG substrate, and (c) a Ti-coated BMG witha film/substrate thickness ratio of 1/20, having $\mu + \beta = 0$ and υ=0.3. The blue solid curves indicate predicted shear-band directions, and the red dashed curves are principal shear-stress directions. The short solid black and dashed green curves are corresponding shear-band directions and the principal shear-stress directions. [155]

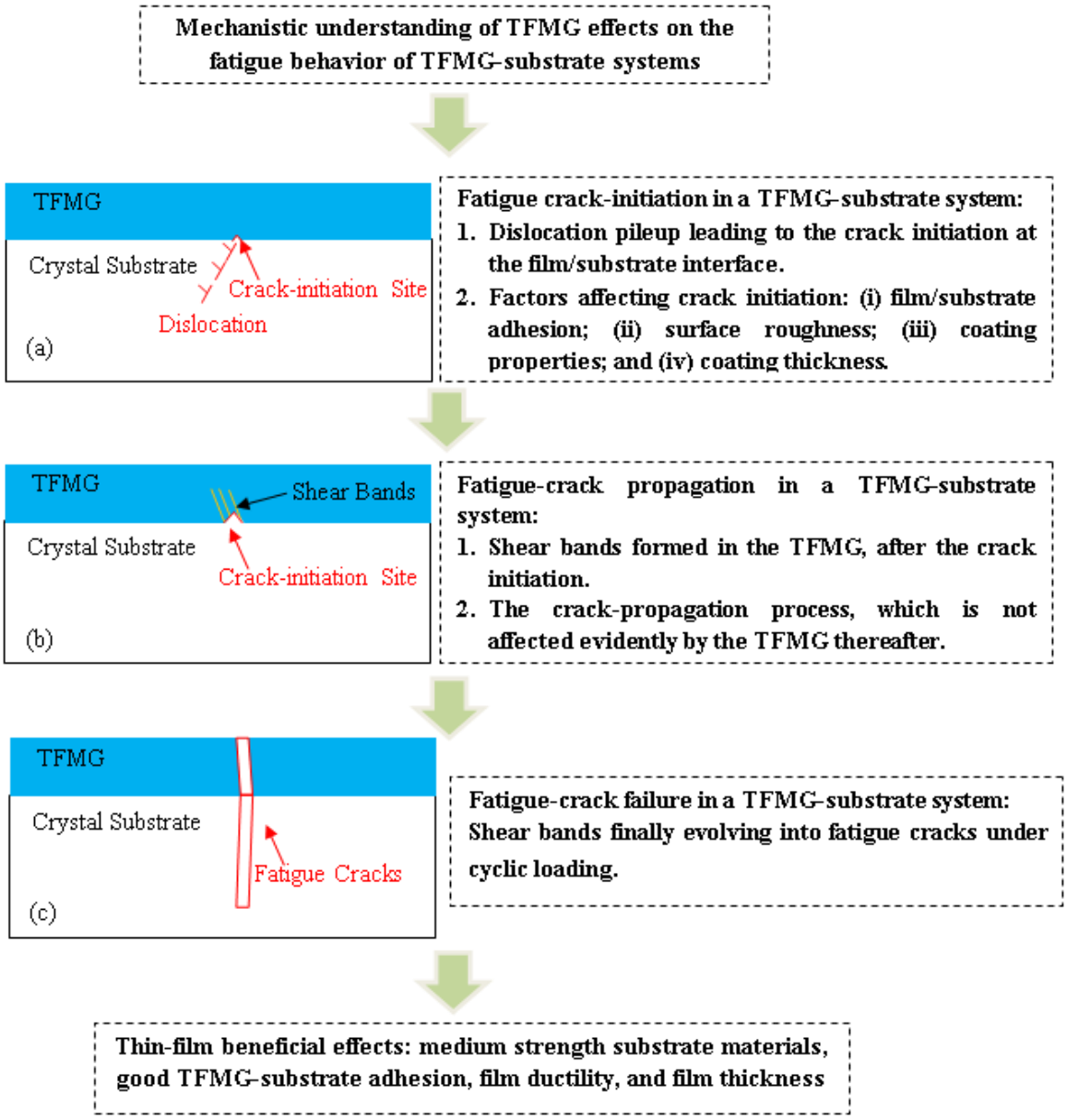

Figure 59. Summary of fatigue crack-initiation and propagation mechanisms in a TFMG/substrate system. [155]

APPENDIX III

Publications

1. G.Y. Wang, H.L. Jia, P.K. Liaw. Fatigue behavior of bulk metallic glasses. Progress in Materials Science (Invited). (in preparation).
2. J.W. Qiao, H.L. Jia, P.K. Liaw. Microstructures and mechanical properties of metallic-glass-matrix composites. Materials Science and Engineering Reports (Invited). (in preparation).
3. H.L. Jia, X. Xie, L. Zhao, J.F. Wang, Y.F. Gao, K.A. Deman, C.L. Ma, P.K. Liaw. Effects of substituting Pd with similar elements on the glass-forming ability and mechanical behavior in Ti-Cu-Zr-Pd bulk metallic glasses. (in preparation).
4. H.L. Jia, L.L. Zheng, W.D. Li, N. Li, J.W. Qiao, G.Y. Wang, Y. Ren, P.K. Liaw, Y.F. Gao. Insights from the lattice strain evolution on deformation mechanisms in metallic-glass-matrix composites. Metallurgical and Materials Transactions A, In Press.
5. H.L. Jia, F.X. Liu, Z.N. An, W.D. Li, G.Y. Wang, J.P. Chu, J.S.C. Jang, Y.F. Gao, and P.K. Liaw. Thin-film metallic glasses for substrate fatigue-property improvements. Thin Solid Films (Invited). 561(2014)2-27.
6. H.L. Jia, L. Huang, C.I. Muntele, T. Zhang, W. He, and P.K. Liaw. A study on the surface structures and properties of Ni-free Zr-based bulk metallic glasses after Ar and Ca ion implantation. Intermetallics. 41(2013)35-43.
7. W. Kai, Y.H. Wua, W.S. Chen, L.W. Tsay, H.L. Jia, and P.K. Liaw. Air-oxidation behavior of a $[(Fe_{50}Co_{50})_{75}B_{20}Si_5]_{96}Nb_4$ bulk metallic glass at 500–650 $^{\circ}$C. Corrosion Science. 66 (2013) 26–32.

8. J.W. Qiao, H.L. Jia, Y. Zhang, and P.K. Liaw. Energy dissipation of shear banding for bulk metallic glasses at ambient and cryogenic temperatures. Materials Chemistry and Physics. 136 (2012) 75-79.

9. W. Kai, Y.H. Wu, W.S. Chen, R.T. Huang, H.L. Jia, P.K. Liaw, and T. Zhang. Air-oxidation behavior of a $[(Co_{50}Cr_{15}Mo_{14}C_{15}B_6)_{97.5}Er_{2.5}]_{93}Fe_7$ bulk-metallic glass at 600-700 $^{\circ}$C (873-973 K). Metallurgical and Materials Transactions A. 43A (2012) 2721-2728.

10. J.W. Qiao, Y. Zhang, H.L. Jia, H.J. Yang, P.K. Liaw, and B.S. Xu. Tensile softening of metallic-glass-matrix composites in the supercooled liquid region. Applied Physics Letters. 100 (2012) 121902.

11. J.W. Qiao, H.L. Jia, C.P. Chuang, E.W. Huang, G.Y. Wang, P.K. Liaw, Y. Ren and Y. Zhang. Low-temperature shear banding for a Cu-based bulk-metallic glass. Scripta Materialia. 63 (2010) 871–874.

VITA

Haoling Jia was born in Shandong Province, China on January 7, 1985. He graduated from the 3rd middle school of Linzi in 2003. He entered the Department of Materials Science and Engineering at Shandong University in 2003, and graduated with a B.S. in 2007. He continued his graduate study in the Department of Materials Science and Engineering at Beihang University and obtained his M.S. in 2010. He enrolled in the doctoral program in the Department of Materials Science and Engineering at the University of Tennessee, Knoxville in 2010. The Doctor of Philosophy degree was received in May 2015.